

The LMARS based shallow-water dynamical core on the cubed-sphere geometry

Xi Chen^{1,2*}

¹Program in Atmospheric and Oceanic Sciences, Princeton University, Princeton, NJ, USA

²Geophysical Fluid Dynamics Laboratory, NOAA, Princeton, NJ, USA

Key Points:

- We present an LMARS-based unstaggered shallow-water model on arbitrary gnomonic cubed-sphere grids
- The solver demonstrates a broad range of diffusion control without any explicit filters
- A newly introduced splash on the sphere test verifies the solver's desirable dispersion properties

*300 Forrester Road, Sayre Hall, Princeton, NJ 08540-6654

Corresponding author: Xi Chen, xic@princeton.edu

Abstract

The rapidly increasing computing powers allow global atmospheric simulations with aggressively high resolutions, which challenges traditional model design principles. This paper presents a Low Mach number Approximate Riemann Solver (LMARS) based unstaggered finite-volume model for solving the shallow-water equations on arbitrary gnomonic cubed-sphere grids. Using a novel reference line-based grid-generation process, it unifies the representation of arbitrary gnomonic cubed-sphere grid projections and permits high-efficiency 1D reconstruction in the halo regions. The numerical discretization also extends a widely used pressure gradient algorithm with the LMARS viscous term, thus improves the model's stability for various numerical applications. The solver demonstrates a broad range of organic diffusion control without any explicit filters, validated by a comprehensive set of test cases. Lastly, a newly introduced splash on the sphere test verifies the solver's desirable dispersion properties and consistent performance among different grid types. This study paves a solid foundation for a new generation of global circulation models with kilometer horizontal scales.

Plain Language Summary

Computing powers and architectures historically influence the numerical algorithm designs of global atmospheric simulations at the fundamental levels. The next generation of the global circulation models can push its resolution to kilometer horizontal scales, which requires vital capabilities in a balanced representation of all motion modes and handling sharp discontinuities such as topography. Here we demonstrate a new framework of a dynamical core that inherits advantages in both traditional geophysical fluid (GFD) modelings and versatile general computational fluid dynamics (CFD) techniques. This new development introduces several innovations, including the unified grid description, numerical optimization, stability enhancement, and a newly designed test to illustrate specific numerical properties cleanly. The desirable results of this work increase our confidence in creating a unique global circulation model to leverage next-generation high-performance computing and to improve our fundamental understanding of the atmospheric processes.

42 **1 Introduction**

43 Building a dynamical core for the atmospheric model is an art of balancing the re-
44 quirements between accuracy and efficiency. Although a model's accuracy can be more
45 definitive to measure in benchmark experiments - at least for smooth solutions, compu-
46 tational efficiency is a relative concept that strongly associates with the computing plat-
47 form characteristics. In a way, the available computational power and machine architec-
48 tures have been dictating the scope of the research topics and the design of the numer-
49 ical simulation. For example, coming out of the wide adoption of the massively paral-
50 lel computing, many modern models prefer quasi-uniform computational grids, such as
51 the icosahedral (Ringler et al., 2000; Tomita et al., 2001; Du et al., 2003; Rípodas et al.,
52 2009) and cubed-sphere grids (Adcroft et al., 2004; Putman & Lin, 2007), over the tra-
53 ditional latitude-longitude grids to evenly distribute the computation tasks over a large
54 number of processors. However, the concepts of both icosahedral and cubed-sphere grids
55 were explored very early in Sadourny et al. (1968); Sadourny (1972); Williamson (1968),
56 but gained very little attention. During this time, single-processor-based latitude-longitude
57 or Gaussian spectral methods demonstrated excellent efficiency in delivering accurate
58 results (Bourke, 1972, 1974) - a perfect example of the evolving standard of the numer-
59 ical algorithm efficiency.

60 The essential motivation of implementing the quasi-uniform grids is to transform
61 the severe two parallel-unfriendly singular points from the latitude-longitude grid (the
62 north and south poles) to less severe eight singularities in the cubed-sphere grid (cor-
63 ners of the six cubed-sphere tiles) or twelve singularities in the icosahedral grid (pentagon
64 cells in a Voronoi perspective). Although the quasi-uniform grids avoid polar filters and
65 other numerical damping schemes due to the polar singularities, they have both pros and
66 cons. In some cases, the numerical artifacts and errors caused by the twelve icosahedral
67 singularities are less severe than the ones caused by cubed-sphere corners. The cubed-
68 sphere grid, however, has several desirable properties. Firstly, many attractive high-order
69 multi-dimensional algorithms achieved optimal computational efficiency by taking ad-
70 vantage of logically Cartesian grids (i.e., rectangles) on each cubed-sphere tile (Rossmanith,
71 2006; Putman & Lin, 2007; C. Chen & Xiao, 2008; Ullrich et al., 2010; Taylor & Fournier,
72 2010). Secondly, the logical 3D cubic geometry on each cube-tile creates one additional
73 dimension to the computational data structure, which offers more flexibility in the par-
74 allel computational optimization designs in both horizontal and vertical directions. Lastly,

75 each tile of the cubed-sphere geometry has a significant similarity with computational
76 grids in regional models. In fact, with separately defined metric terms, the global cubed-
77 sphere dynamical core requires almost no code change to convert into a regional solver
78 in orthogonal grids. This property provides exceptional convenience and flexibility in uni-
79 fying real-world applications and experimenting new algorithms with idealized valida-
80 tion tests.

81 The global circulation models (GCMs) cover a vast range of scales and operate on
82 the most powerful high-performance computers available. Therefore, geophysical fluid
83 models usually discretize the governing equations with various grid staggering choices
84 (Arakawa & Lamb, 1977, namely A-, B-, C-, D-Grid) to gain numerical advantages in
85 resolving the smallest waves. In particular, the C-Grid results in natural pressure gra-
86 dient in the momentum equations and straightforward divergence representation (Adcroft
87 et al., 2019); the D-Grid forms a perfect vorticity mode (Lin, 2004; Harris & Lin, 2013),
88 which dominates large-scale to mesoscale atmospheric motions. With the recent rapid
89 increase of computational power, the GCM community is pushing the model resolution
90 aggressively to about a globally-kilometer horizontal scale (Stevens et al., 2019; Satoh
91 et al., 2019). At this scale, both divergence and vorticity play equally important roles.
92 Therefore, the unstaggered discretization could be a balanced choice in global kilometer-
93 scale model development.

94 Although most GCMs use staggered discretization, a few influential models utilize
95 the A-Grid, including NICAM (Tomita et al., 2001) with a stencil-based scheme, and the
96 E3SM (Taylor et al., 2020) with a compact Spectral-Element-based algorithm. Colocat-
97 ing the velocity components and scalars with a stencil-based scheme has several unique
98 and attractive advantages. It allows direct coupling between the explicitly simulated dy-
99 namical process and parameterized physics processes. No interpolation of the velocity
100 components is required, therefore, eliminating errors associated with such practices. Fur-
101 thermore, it can yield energy conservation in non-hydrostatic models. With colocated
102 prognostic variables, it is possible to formulate a flux-form prognostic total-energy gov-
103 erning equation, thus automatically provide energy conservation to the models. Energy
104 conservation is beyond the scope of the shallow-water implementation and will be ex-
105 tensively discussed in future work. Preliminary work has demonstrated promising results
106 in Li and Chen (2019). Last but not least, unstaggered schemes are widely implemented

107 in traditional computational fluid dynamics applications. Many well-tested techniques
108 can inspire the creation of algorithms in the geophysical fluid simulations.

109 Despite many efforts, historically, the unstaggered discretization was overwhelmed
110 by staggered methods due to, at least, two primary considerations. One challenge is that
111 compared with the staggered schemes, the unstaggered discretization tends to produce
112 severe errors in resolving phase speed for waves with very short wavelengths. Addition-
113 ally, it is more challenging to design numerically robust algorithms with an unstaggered
114 grid. For example, an unstaggered central-differencing of gradient term could produce
115 a so-called “grid decoupling” problem and lead to checkerboard-pattern noise. Indeed,
116 the long-term success of an unstaggered model depends on the proper treatment to ad-
117 dress the above difficulties.

118 To address the first concern, the previous installment of this work thoroughly in-
119 vestigated the dispersive and dissipative relations between different grid staggering choices
120 and orders of accuracy (X. Chen et al., 2018). One of the principal findings is that with
121 high-order algorithms, e.g., using 3-points or 5-points stencil polynomial schemes, waves
122 with problematic phase speeds will be largely pushed to four-grid-spacing and below. On
123 the other hand, in practice, the smallest resolvable wavelengths are contaminated by many
124 sources of errors, such as numerical diffusion, strong gradients in the solutions, and, ac-
125 cordingly, heavily damped or removed by numerical techniques. Therefore, using high-
126 order numerical schemes can prevent the unstaggered model from problematic phase speeds.
127 X. Chen et al. (2018) also introduced simple-to-setup tests to validate the dispersion and
128 dissipation properties of any sophisticated solvers.

129 Unstaggered algorithms for geophysical flows can inherit various robust approaches
130 from other fields. Unlike the geophysical fluid modeling field, the general computational
131 fluid dynamics (CFD) community widely adopts unstaggered algorithms via the imple-
132 mentation of the approximate Riemann Solvers. There is a small but growing literature
133 that takes advantage of the Riemann Solvers in the A-Grid GCMs and achieved stabil-
134 ity, high order accuracy, and are free of explicit diffusion (Giraldo et al., 2002; C. Chen
135 & Xiao, 2008; Ullrich et al., 2010; Yang et al., 2010). However, compared with state-of-
136 science GCMs, the traditional Riemann solvers can be less efficient or more diffusive. More-
137 over, the Riemann solvers with carefully designed mathematical expressions are most ef-
138 fective in simulating generic flow types, including the vacuum, shock, sharp discontinu-

139 ities. Therefore, it is not easy to understand the Riemann solvers' inherent numerical
140 properties and make the comparison to traditional GCM implementations. Lastly, tra-
141 ditional Riemann solvers require careful adjustments to make them accurate on the unique
142 geometry on the Earth's surface with the gravity and the Coriolis forces.

143 The Low Mach number Approximate Riemann Solver (LMARS) introduced in X. Chen
144 et al. (2013) is a highly efficient tool in the finite-volume method based GCMs. The de-
145 sign of LMARS bases on the fact that the geophysical flows do not create any vacuum
146 or sharp discontinuities and the subsonic flows Mach number is always less than 1. The
147 resulting simple mathematical expression of LMARS requires only one approximation,
148 which assumes the sound wave speed (or gravity wave speed in a shallow-water model)
149 is continuous at the finite volume interfaces. The LMARS discretization in a full 3D at-
150 mosphere takes the gravity into account and results in better accuracy than traditional
151 Riemann solvers (Li & Chen, 2019). Previous work has implemented LMARS in many
152 atmospheric applications, including hydrostatic and non-hydrostatic flows with either
153 vertical Lagrangian coordinates or Eulerian coordinates (X. Chen et al., 2013). It is also
154 implemented in the multi-gas planet atmosphere environment with an intrinsic energy-
155 conserving framework (Li & Chen, 2019). As a promising candidate for a new unstag-
156 gered GCM, LMARS is not yet tested with a cubed-sphere geometry.

157 This study aims to develop an LMARS-based unstaggered finite-volume shallow-
158 water solver on the gnomonic cubed-sphere grids. The shallow-water equations offer a
159 standard testbed to validate the horizontal advection algorithms. Whereas previous stud-
160 ies implemented various cubed-sphere grids in different solvers, this work is the first to
161 unify arbitrary gnomonic cubed-sphere grid generation processes. Although the numer-
162 ical discretization of LMARS on the cubed-sphere grid does not contain any explicit fil-
163 ter, this solver can still exhibit a broad range of diffusion properties by controlling the
164 polynomial reconstructing methods and the strength of the forward-backward techniques
165 (Mesinger, 1977). Lastly, various model numerical properties are illustrated and gauged
166 by a comprehensive set of idealized tests, including the traditional famous Williamson
167 et al. (1992) shallow water test suite, and a recently introduced colliding modons test
168 (Lin et al., 2017). Given the traditional discussions about unstaggered grid dispersion
169 uncertainties, this study designs a new "splash on the sphere" test to illustrate and war-
170 rant satisfactory dispersion and dissipation properties on specific wavelengths.

171 The remainder of the paper is organized as follows. Section 2 provides a brief primer
 172 of the gnomonic cubed-sphere grids, in which a unified grid generation process is intro-
 173 duced. Section 3 describes both spatial and temporal numeric discretization. The model
 174 is validated in section 4. In this section, a novel splash on the sphere test is introduced
 175 to gauge the dispersion and dissipation properties. Finally, the main findings and dis-
 176 cussions are concluded in Section 5. Appendix A collects all major symbols to make the
 177 notations consistent and clear. Appendix B provides a mathematical description of the
 178 grid generating process. The governing equations in the cubed-sphere grids are provided
 179 in Appendix C. In this section, some optimizations are discussed to yield more efficient
 180 mathematical expressions.

181 **2 A brief primer on gnomonic cubed-sphere grids and the duo-grid** 182 **system**

183 The FV3 (Finite-Volume Cubed-Sphere Dynamical Core) (Lin, 2004; Putman &
 184 Lin, 2007; Harris & Lin, 2013) has strongly influenced the development of this work. Al-
 185 though being different in staggering choices, the new unstaggered dynamical core is de-
 186 signed to be a seamless evolution within the existing FV3 framework. Therefore, this work
 187 follows a significant amount of naming conventions from the existing FV3 code base, in-
 188 cluding grid type names and dynamical parameter definitions and symbol names.

189 The cubed-sphere grid is obtained from projecting a gridded cube onto the surface
 190 of the sphere, which avoids the polar singularities due to the convergence of the merid-
 191 ians from the traditional latitude-longitude coordinate system. The cubed-sphere grid
 192 shifts the severe polar convergence of meridians to eight weaker singularities at the cor-
 193 ners where cube tiles intersect. Figure 1 illustrates the mapping from the cube to the
 194 sphere in a C8 resolution. The naming convention $C[N]$ denotes that each tile of the cube-
 195 sphere has N by N cell distribution, which results in $N \times N \times 6$ total cells on the sphere.
 196

197 **2.1 Interlock patterns**

198 There are two conventional logical arrangements to interlock the six cubed-sphere
 199 tiles. Figure 2a illustrates the first pattern (Ronchi et al., 1996; Rossmannith, 2006; Yang
 200 et al., 2010) with four tropical tiles and two polar tiles, denoted by the “tropic-belt” log-
 201 ical arrangement. Unfortunately, the interlock between the tiles is not symmetric and

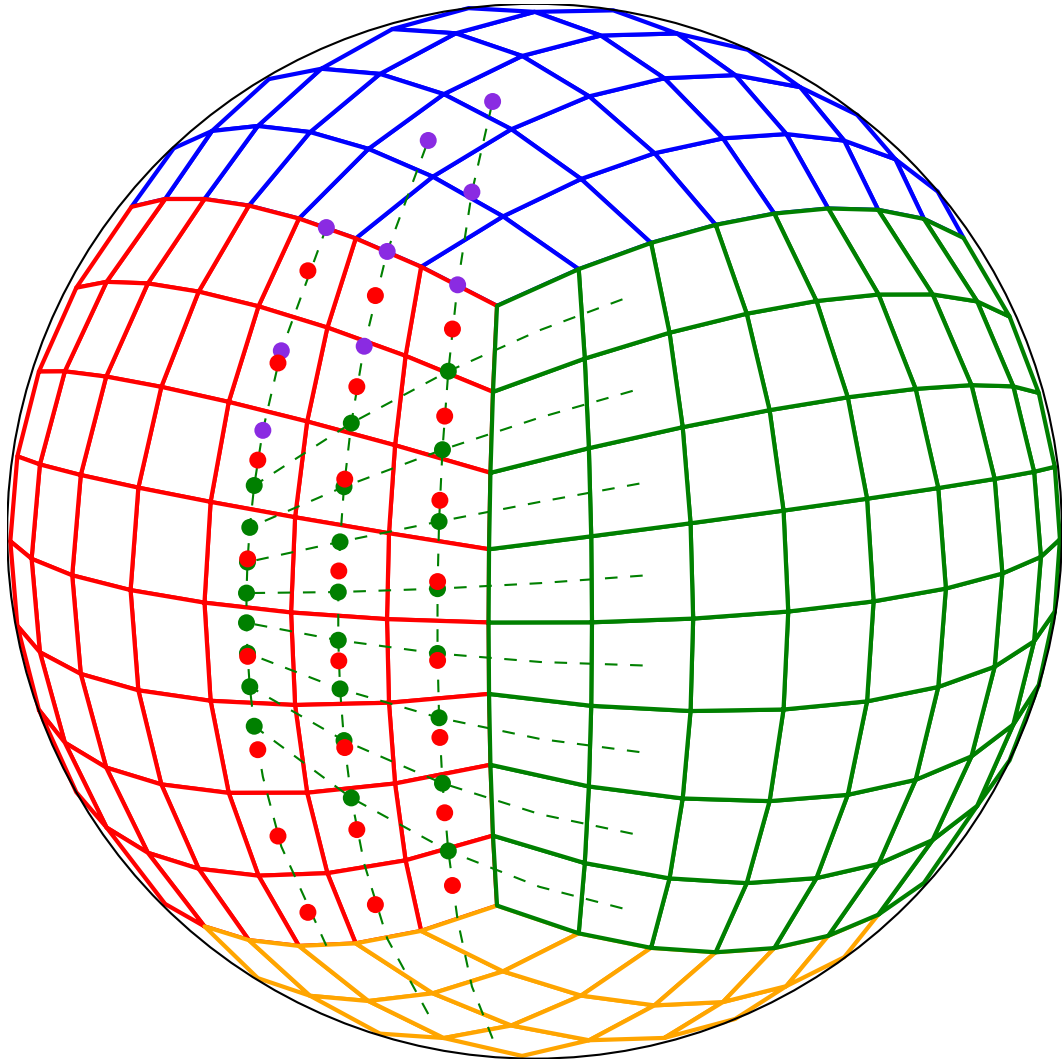


Figure 1. C8 ($8 \times 8 \times 6$) cubed-sphere grid with three layers of ghost cells. When aligned on the same great circle, a simple 1-D polynomial interpolation from the red dots can provide the green dots' values with optimum accuracy and speed.

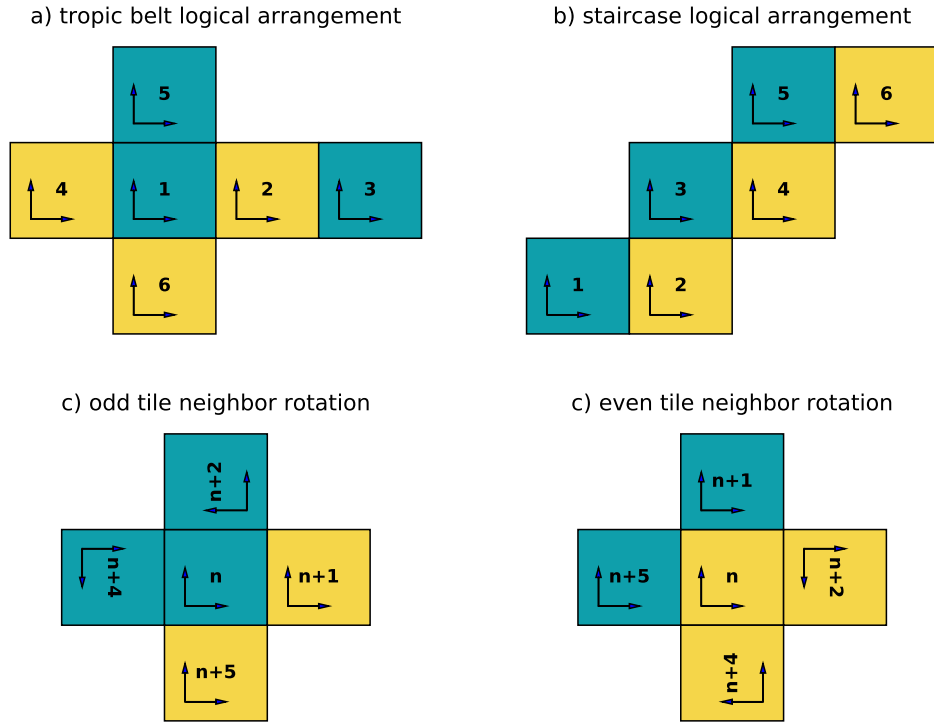


Figure 2. The logic arrangement of the six cubed-sphere tiles. a) the “tropic belt” arrangement has four tropic tiles and two polar tiles, the local coordinate directions are as illustrated at the lower-left corners. b) the “staircase” arrangement and the local coordinates illustration. The “staircase” arrangement simplifies the determination of the neighbor tile indices and orientations into c) odd-index-tile and d) even-index-tile cases. Note if the number $n + l > 6$, the corresponding tile number is $n + l - 6$.

202 require separate distinction for each of the tile. The second pattern (Adcroft et al., 2004)
 203 is illustrated in Figure 2b, and denoted by the “staircase” logical arrangement. The “stair-
 204 case” logical arrangement has better symmetry when exchanging information between
 205 tiles. For example, the calculation of fluxes between two adjacent tiles needs to deter-
 206 mine the tile numbers and the tile-local coordinates rotations. The “staircase” arrange-
 207 ment simplifies the neighbor tile-number and rotation patterns into two odd-index-tile
 208 (tiles 1, 3, 5) and even-index-tile (tiles 2, 4, 6) scenarios, illustrated by Figures 2c, and
 209 d. Both logical arrangements are valid for cubed-sphere applications. This work imple-
 210 ments the “staircase” arrangement to gain some programming simplicities.

2.2 Unified gnomonic projections

The grid lines connecting the grid points are continuous great circles on the sphere. Therefore, the locations of vertices can uniquely determine the full grid system on each cube-sphere tile. On each tile, e.g., the tile centered at $(\lambda, \phi) = (0, 0)$, the vertices can be generated by either the gnomonic (Sadourny, 1972; Ronchi et al., 1996) or the conformal (McGregor, 1996; Rančić et al., 1996) projections. The gnomonic projection projects a Cartesian grid from six straight-lines-meshed cube surfaces to the sphere surface. The conformal projection maximizes the orthogonality of the coordinates. Putman and Lin (2007) examined the most popular approaches: the equidistant projection (Sadourny, 1972), the equiangular projection (Ronchi et al., 1996), the more orthogonal conformal mapping (Rančić et al., 1996), the numerical modification to analytical mappings by an elliptic solver (Khamayseh & Mastin, 1996) or the spring dynamics generator (Tomita et al., 2001). Considering the eight singularities at cube corners remain nonorthogonal in the conformal grid, and the cell size distribution in conformal grids is usually less uniform than the gnomonic choices, this work implements the gnomonic grid.

Figure 3 illustrates a typical gnomonic projection between a grid point on the cube-tile and the sphere-tile. Let the grid points on a cube-tile be indexed by $[i, j]$, with local coordinate $[X, Y]$. In a gnomonic projection, each row of grid points $[i, :]$ shares the same Y value, and each column of grid points $[:, j]$ shares the same X value. The projection of the rows and columns on each cube face forms great circles on the sphere. Furthermore, the coordinates on the sphere converge to a pair of local north-/south-poles, and “west-/east-poles” for each sphere tile (Rossmanith, 2006, Figure 1).

This work offers a novel approach to unite generic gnomonic grid descriptions. Although previous work demonstrated different ways to create various gnomonic grids, the gnomonic grids share distinct properties. Given the orthogonality and symmetry of the gnomonic projected grid points on each cube-tile, the locations of grid points in a single row or column can fully determine the entire gnomonic cubed sphere. Therefore, Figure 3 can determine three widely used gnomonic projections in the literature by three pairs of reference lines with grid points equally distributed. The red reference lines stand for the most traditional equidistance projection (Sadourny, 1972). The equiangular grid (Ronchi et al., 1996) can be obtained by projecting the green lines with grid points equally distributed back to the cube tile and populating them to the entire $[X, Y]$ space. Lastly,

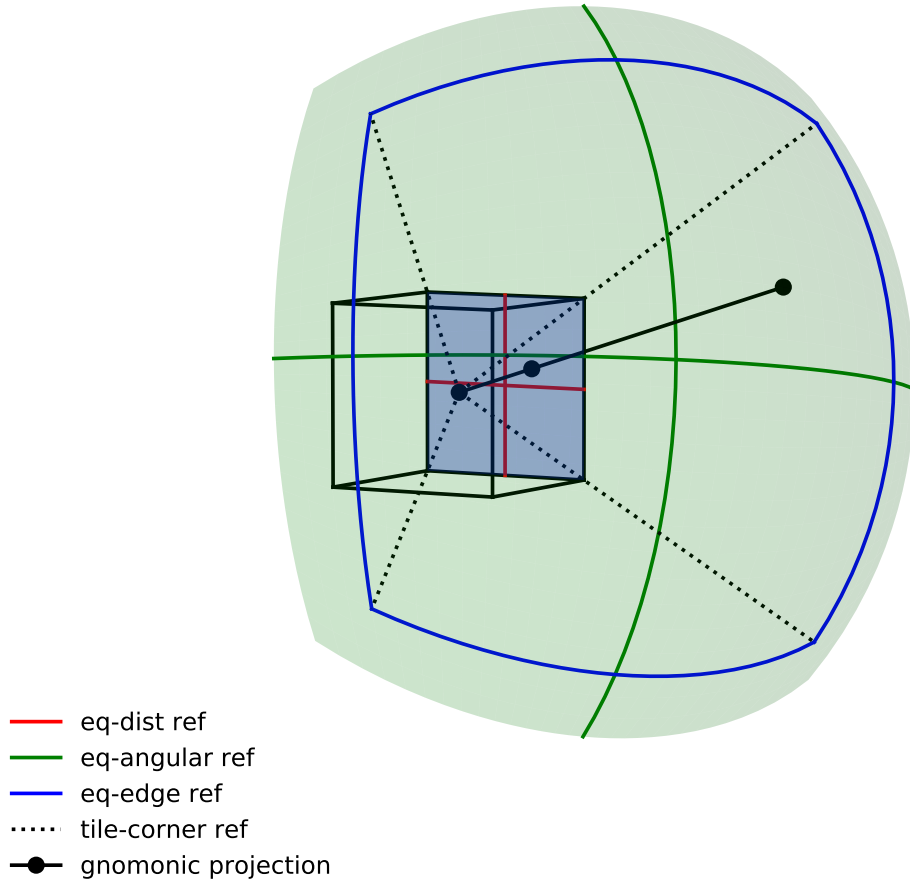


Figure 3. The gnomonic projection. The blue shaded surface is a *cube-tile*, and the green shaded surface is a *sphere-tile*. The solid black line from the sphere center to the sphere surface illustrates a *gnomonic projection* between a grid point on the cube-tile and a grid point on the sphere-tile. The dotted lines define the corners of the bounds to one of the six surfaces of the cubed-sphere grid. The red lines are the *gnomonic projection reference lines* of the equidistance projection, and the green and blue lines are of the equiangular and *equi-edge* projections. The extension of the green surface indicate the ghost cell region for a finite-volume application.

243 although not formally documented, FV3 (Putman & Lin, 2007; Harris & Lin, 2013; Har-
 244 ris et al., 2016) introduced a gnomonic projection with more uniformly distributed cells
 245 on the tile interfaces, and is now adopted in the Next Generation Global Prediction Sys-
 246 tem (NGGPS) project (Zhou et al., 2019). The FV3 grid is denoted by the “equi-edge”
 247 grid and can be obtained similarly by populating the grid-points-equally-distanced blue
 248 lines on the sphere. The following procedures describe the process to populate the ref-
 249 erence line grid points to the full gnomonic projections:

- 250 1. Project the equally distributed grid points from the reference lines onto the gray-
 251 color cube-tile (this procedure is redundant for the red line).
- 252 2. Mesh the gray cube-tile with the projected 1D distribution of the grid points from
 253 the cube surface.
- 254 3. Project the fully meshed grid points from the gray cube tile to the green sphere
 255 tile.

256 The equidistance grid produces less uniformly distributed volumes on the sphere. There-
 257 fore, most modern cubed-sphere models do not implement the equidistance grid. Although
 258 the equiangular projection yield slightly more uniform grid point distribution on the sphere,
 259 the equi-edge grid distributes grid points evenly near the sphere tile connections, which
 260 are the primary sources that cause grid imprinting with a cubed sphere. Additionally,
 261 in a stretched grid (Harris et al., 2016), the equi-edge grid produces the focused tile with
 262 more evenly distributed cells. This work only discusses the equi-edge and the equian-
 263 gular grids, namely `grid_type 0` and `2`, following FV3 naming convention.

264 **2.3 The duo-grid system to handle tile-edge connections**

265 This work implements a maximum 5-point-stencil polynomial reconstruction for
 266 the finite volume scheme. Therefore each tile requires three more layers of ghost cells by
 267 the wave propagation method (X. Chen et al., 2013, 2018; Li & Chen, 2019). Unfortu-
 268 nately, a main numerical challenge with the gnomonic cubed-sphere grid is that the grid
 269 coordinates are not continuous across tile interfaces. Figure 1 illustrates the ghost cells
 270 on the local west-side of the green tile, which creates a west halo region. The native neigh-
 271 bor cell centers in the halo region are the red dots, which forms “kinks” in coordinates
 272 between the green tile and its west halo. Therefore, the name “kinked grid” denotes this
 273 halo type constructed by directly copying values from the neighboring tiles. A natural

274 extension of the green tile coordinates (green dashed lines) into the halo region results
 275 in green dots, denoted by the “extended grid.”

276 There are two reasonable choices for the ghost cell numerical algorithms. FV3 pow-
 277 ered models, for example, directly employ the red dots in the kinked-grid to form one-
 278 sided flux calculations to the tile boundaries. This method has several advantages. The
 279 operations in the halo region (e.g., west halo of the green tile) can be identical to the na-
 280 tive calculations on the neighboring tile (red tile) from different calculating processors
 281 (Putman & Lin, 2007; Harris & Lin, 2013). Additionally, calculations associated with
 282 halo create almost no computational overhead, a valuable property to massively paral-
 283 lel computing. This work implements the other approach, which is to remap the red dots
 284 from the kinked-grid to the green dots on the extended grid (Rossmanith, 2006; Yang
 285 et al., 2010; Ullrich et al., 2010; Katta et al., 2015). Therefore, the halo operations are
 286 a natural extension from the interior calculations, and no extra adjustment is required
 287 for the ghost cells. The second approach can effectively reduce the cubed-sphere grid im-
 288 printing at the tile edges, but creates undesired overhead in the parallel calculations. The
 289 extra calculations are mainly: 1. tile-interface flux synchronization between different tiles;
 290 2. remapping of the prognostic variable values from the kinked grid to the extended grid.

291 The first synchronization overhead is due to inconsistent coordinate directions be-
 292 tween tiles. The fluxes at the same interfaces by different tiles need to be sent to the ad-
 293 jacent tile and get averaged for conservation properties. This operation is only performed
 294 at the end of a full cycle of integration to minimize the message passing.

295 The interpolating algorithm must be at minimum complexity to alleviate the duo-
 296 grid remapping overhead. Most equiangular projection applications take advantage of
 297 that the green dots and red dots are aligned on the same great circle. Thus 1-D inter-
 298 polation is sufficient for the remapping procedure. This property is denoted by duo-grid
 299 1D alignment. Unfortunately, this 1D alignment only applies to equiangular projection.
 300 A direct halo generation with equidistance or equi-edge projections (i.e., by extending
 301 three more layers into the halo during the interior grid creation) does not produce the
 302 duo-grid 1D alignment. A few extra steps by the following procedures can solve this prob-
 303 lem and warrant the duo-grid 1D alignment for arbitrary gnomonic projections:

- 304 1. Populate the non-halo gnomonic projection grid points based on the reference lines
 305 (red for equidistance, blue for equi-edge, and green for equiangular).

- 306 2. Identify the grid points on the resulting sphere tile center lines (i.e., the green lines
 307 in Figure 3).
 308 3. Mirror the outermost three points from the green lines to the ghost region.
 309 4. Populate ghost cell grid points in the halo region base on the mirrored points on
 310 the green lines.

311 To minimize the remapping overhead, in this work, the minimum 1D piecewise linear in-
 312 terpolation is used to remap values from the red to the green points. No discernible degra-
 313 dation is observed compared with high-order 1D polynomial remapping algorithms. De-
 314 tailed mathematic procedures in the gnomonic cubed-sphere generation are described
 315 in Appendix B.

316 **3 The numerical discretization**

317 **3.1 The governing equations discretization**

318 A standard mathematical derivation of the governing equations on the cubed-sphere
 319 is included in Appendix C. Before rearranging and discretizing the governing equations,
 320 denote η an arbitrary variable, the following finite-volume (FV) operators are defined:

$$321 \quad \delta_x [\eta]_{i,j} = \eta_{i+0.5,j} - \eta_{i-0.5,j}, \quad (1)$$

$$322 \quad \delta_y [\eta]_{i,j} = \eta_{i,j+0.5} - \eta_{i,j-0.5}, \quad (2)$$

323 where $\eta_{i\pm 0.5,j}$ are the values of η evaluated at cell interfaces in the x-direction, and $\eta_{i,j\pm 0.5}$
 324 are the values of η evaluated at cell interfaces in the y-direction. Unless specifically spec-
 325 ified, the subscripts (i, j) are omitted for cleaner mathematical expressions, and the vari-
 326 ables without subscripts are evaluated at the cell centers at location (i, j) .
 327

328 The continuity equation can be rearranged in the flux form:

$$329 \quad \frac{\partial h}{\partial t} = -\frac{1}{\Delta A} (\delta_x (hu_{\perp}^x \Delta y) + \delta_y (hw_{\perp}^y \Delta x)), \quad (3)$$

330 Define the flux coefficient:

$$331 \quad f_{i+0.5,j}^x (u_{\perp}^x, \Delta t) = u_{\perp}^x \Delta t \Delta y_{i+0.5,j}, \quad (4)$$

$$332 \quad f_{i,j+0.5}^y (u_{\perp}^y, \Delta t) = u_{\perp}^y \Delta t \Delta x_{i,j+0.5}. \quad (5)$$

333 Therefore, the final discretization of the continuity equation is:
 334

$$335 \quad h^{n+1} = h^n - \frac{1}{\Delta A} (\delta_x (f^x h) + \delta_y (f^y h)), \quad (6)$$

336 and a straightforward discretization to update the cell center velocity components is:

$$337 \quad u^{n+1} = u^n + \left(\sqrt{g\hat{v}} (\zeta + f) - \frac{1}{\Delta x} \delta_x (\Pi + \Phi_s + K) \right) \Delta t, \quad (7)$$

$$338 \quad v^{n+1} = v^n + \left(-\sqrt{g\hat{u}} (\zeta + f) - \frac{1}{\Delta y} \delta_y (\Pi + \Phi_s + K) \right) \Delta t, \quad (8)$$

340 The relative vorticity ζ at cell centers can be numerically evaluated by:

$$341 \quad \zeta = \frac{1}{\Delta A} \left(\delta_x (u_{\parallel}^x \Delta y) - \delta_y (u_{\parallel}^y \Delta x) \right), \quad (9)$$

342 and the kinetic energy K can be numerically evaluated at cell interfaces by:

$$343 \quad K = \frac{1}{2} (u_{\perp} u_{\perp} + u_{\parallel} u_{\parallel}). \quad (10)$$

344 Note that K or u_{\perp} , u_{\parallel} are all defined at the cell interfaces, and the labels in x and y di-
345 rections are omitted.

346 All cell-center or cell-averaged variable values are straightforward to calculate. The
347 next step is to determine the values at the cell interfaces using an efficient approximate
348 Riemann solver and evaluate the terms in the δ_x and δ_y operators.

349 **3.2 Calculation of cell-interface values by LMARS**

350 The remaining variables to be determined at the cell interfaces are: u_{\perp} , h , Π , Φ_s ,
351 and K (i.e., u_{\perp} , u_{\parallel}).

352 Following the naming conventions in X. Chen et al. (2018), $\eta_{i,j}^W$ and $\eta_{i,j}^E$ denote the
353 “west” and “east” volume boundary values of arbitrary variable η calculated by poly-
354 nomial reconstruction within volume (i, j) . Therefore, the mismatching $\eta_{i,j}^E$ and $\eta_{i+1,j}^W$
355 are evaluated at two sides of the interface between cell (i, j) and $(i + 1, j)$. The first step
356 of LMARS is to evaluate cell interface values of Π and u_{\perp} . In the x-direction:

$$357 \quad (u_{\perp}^x)_{i+0.5,j} = \frac{1}{2} \left((u_{\perp}^x)_{i,j}^E + (u_{\perp}^x)_{i+1,j}^W \right) + \frac{1}{2a_{i+0.5,j}} (\Pi_{i,j}^E - \Pi_{i+1,j}^W), \quad (11)$$

$$358 \quad \Pi_{i+0.5,j} = \frac{1}{2} (\Pi_{i,j}^E + \Pi_{i+1,j}^W) + \frac{a_{i+0.5,j}}{2} \left((u_{\perp}^x)_{i,j}^E - (u_{\perp}^x)_{i+1,j}^W \right), \quad (12)$$

360 where a is the gravity wave speed (group velocity) estimated at cell interface:

$$361 \quad a_{i+0.5,j} = \sqrt{\frac{1}{2} (\Pi_{i,j}^E + \Pi_{i+1,j}^W)}. \quad (13)$$

362 Once the velocity normal to the cell interface determined, the values of the vari-
 363 ables to be transported are chosen using upwind values:

$$364 \quad h_{i+0.5,j} = \begin{cases} h_{i,j}^E & \text{if } (u_{\perp}^x)_{i+0.5,j} > 0 \\ h_{i+1,j}^W & \text{else} \end{cases}, \quad (14)$$

$$365 \quad (u_{\parallel}^x)_{i+0.5,j} = \begin{cases} (u_{\parallel}^x)_{i,j}^E & \text{if } (u_{\perp}^x)_{i+0.5,j} > 0 \\ (u_{\parallel}^x)_{i+1,j}^W & \text{else} \end{cases}, \quad (15)$$

367 and the operations on the y-direction is symmetric and analogous.

368 Although algebraically h and Π are interchangeable with the relation $\Pi = Gh$,
 369 they play different roles in the governing equation. Π stands for pressure forcing term,
 370 and h is associated with material transportation. Therefore, their treatments are differ-
 371 ent in the LMARS solver. In a fully compressible model, their corresponding terms are
 372 the density and pressure (X. Chen et al., 2013; Li & Chen, 2019).

373 The last piece for a single sub-cycle update is to reconstruct the prognostic vari-
 374 ables' values at four horizontal cell edges. Following X. Chen et al. (2018) conventions,
 375 assuming an N_c -point stencil polynomial reconstruction for an arbitrary variable η :

$$376 \quad \eta_{i,j}^W = \sum_{l=1-N_g}^{N_g-1} W^{(l)} \eta_{i+l,j}, \quad (16)$$

$$377 \quad \eta_{i,j}^E = \sum_{l=1-N_g}^{N_g-1} E^{(l)} \eta_{i+l,j}, \quad (17)$$

$$378 \quad \eta_{i,j}^S = \sum_{l=1-N_g}^{N_g-1} W^{(l)} \eta_{i,j+l}, \quad (18)$$

$$379 \quad \eta_{i,j}^N = \sum_{l=1-N_g}^{N_g-1} E^{(l)} \eta_{i,j+l}, \quad (19)$$

383 where $W^{(l)} = E^{(-l)}$, $N_c = 2N_g - 1$, and N_g is the layers of ghost cells required at the
 384 tile edges. The lookup coefficient tables for point-value reconstruction and finite-volume
 385 reconstruction from X. Chen et al. (2018) is repeated in Tables 1 and 2 for reference. Al-
 386 though this work does not implement any monotonic filters, most filtering schemes can
 387 be considered equivalent to altering the reconstruction coefficient values locally accord-
 388 ing to the shape of the solutions.

Table 1. The coefficient to calculate “east” side midpoint value on a stencil number of $N_c = 2N_g - 1$ from Point-Value variables

N_g	$E_{pt}^{(-2)}$	$E_{pt}^{(-1)}$	$E_{pt}^{(0)}$	$E_{pt}^{(1)}$	$E_{pt}^{(2)}$
1			1		
2		-1/8	3/4	3/8	
3	3/128	-5/32	45/64	15/32	-5/128

Table 2. the coefficient to calculate “east” side midpoint value on a stencil number of $N_c = 2N_g - 1$ from Volume-Mean variables

N_g	$E_{vm}^{(-2)}$	$E_{vm}^{(-1)}$	$E_{vm}^{(0)}$	$E_{vm}^{(1)}$	$E_{vm}^{(2)}$
1			1		
2		-1/6	5/6	1/3	
3	1/30	-13/60	47/60	9/20	-1/20

389

3.3 Extension of the pressure gradient algorithm in L97 with LMARS

390

viscous terms and the forward-backward algorithm

391

392

393

394

395

396

397

398

399

400

401

402

403

Up to this part, the numerical discretization closely follows the original LMARS approach described by X. Chen et al. (2013, 2018), which is sufficient for this shallow water solver. Alternatively, Lin (1997) (L97) introduces an innovative spatial discretization to the pressure gradient term. Although mathematically equivalent to this work, the L97 pressure gradient algorithm considerably simplifies the discretization in a full 3D compressible model and makes the numerical expression backward compatible with a shallow-water solver. One drawback of L97 is that the expression is a geometric realization of the volume interface pressure force integration. Therefore, it lacks the implicit diffusion calculated by a Riemann solver, and extra filters are required to stabilize the model. Fortunately, LMARS simple expression allows the separation of the geometric derivative terms and viscous terms. It is straightforward to extend the L97 pressure gradient algorithm with the LMARS viscous contribution and result in a fast and stable pressure gradient scheme.

As discussed previously, the volume interface pressure force obtained by LMARS described in Eq. 12 can be represented by an averaging term and a viscous term:

$$\Pi_{i+0.5,j} = \bar{\Pi}_{i+0.5,j} + \Pi_{i+0.5,j}^{\text{vis}}, \quad (20)$$

where

$$\bar{\Pi}_{i+0.5,j} = \frac{1}{2} (\Pi_{i,j}^E + \Pi_{i+1,j}^W), \quad (21)$$

$$\Pi_{i+0.5,j}^{\text{vis}} = \frac{a_{i+0.5,j}}{2} \left((u_{\perp}^x)^E_{i,j} - (u_{\perp}^x)^W_{i+1,j} \right). \quad (22)$$

Therefore, the pressure gradient with the topographic contribution, for example, in the x-direction is discretized:

$$\frac{\partial}{\partial x} (\Pi + \Phi_s) = \frac{1}{\Delta x} \delta_x (\bar{\Pi} + \bar{\Phi}_s) + \frac{1}{\Delta x} \delta_x \Pi^{\text{vis}}. \quad (23)$$

Note that X. Chen et al. (2018) explained that the viscous term Π^{vis} in 1D is equivalent to a $2N_g$ -order diffusion term, which automatically matches the stencil size of the reconstruction schemes. The same function evaluates the surface geopotential at cell interface to warrant numerical consistency:

$$(\bar{\Phi}_s)_{i+0.5,j} = \frac{1}{2} \left((\Phi_s)^E_{i,j} + (\Phi_s)^W_{i+1,j} \right). \quad (24)$$

The following equivalent expressions are defined to simplify the expression:

$$\eta_{(\pm,\pm)}^x \equiv \bar{\eta}_{i\pm 0.5,j,k\pm 0.5}, \quad (25)$$

and the first term in pressure gradient can be rearranged in L97 format:

$$\delta_x (\bar{\Pi} + \bar{\Phi}_s) = \frac{(\Phi_{(-,+)}^x - \Phi_{(+,-)}^x) (p_{(+,+)}^x - p_{(-,-)}^x) + (\Phi_{(-,-)}^x - \Phi_{(+,+)}^x) (p_{(-,+)}^x - p_{(+,-)}^x)}{p_{(-,+)}^x + p_{(+,+)}^x - p_{(-,-)}^x - p_{(+,-)}^x}. \quad (26)$$

The expression in the y-direction is analogous. With this expression, the SWE and 3D compressible pressure gradient numerical discretization can share the identical code.

Another expansion of the pressure gradient calculation is to implement the forward-backward (FB) technique (Mesinger, 1977) to enhance the stability of the model. X. Chen et al. (2018) conducted several numerical analysis on the FB technique. One of the key findings in the 1D linearized environment is that the FB operation is equivalent to a second-order diffusion term on the velocity components, which is vital for the stability of a single-step scheme. In this model with multi-step schemes, the FB scheme is not a necessary

434 component but can be useful in the future fully coupled 3D model as a diffusion mod-
 435 erator. Considering the FB is almost computationally equivalent to an explicit scheme,
 436 a relaxed-FB scheme is implemented by setting a parameter $\beta \in [0, 1]$ to the geomet-
 437 ric pressure gradient term following Harris and Lin (2013):

$$438 \quad \delta_x (\bar{\Pi} + \bar{\Phi}_s) = (1 - \beta) \delta_x (\bar{\Pi} + \bar{\Phi}_s)^{n+1} + \beta \delta_x (\bar{\Pi} + \bar{\Phi}_s)^n. \quad (27)$$

439 Therefore, the parameter β in the FB scheme is an implicit control coefficient of a 2nd-
 440 order diffusion term. The response to various beta values will be validated in the test
 441 section.

442 **3.4 Temporal discretization**

443 The linearized two-step and three-step Runge-Kutta schemes (rk2 and rk3) are im-
 444 plemented for time integration. In each substep, denote prognostic variable array U and
 445 right-hand-side term $\text{RHS}(U, N_g, \beta)$, where the dynamical parameters N_g controls the
 446 stencil size of the reconstruction scheme and β controls the strength of the FB algorithm
 447 in the pressure gradient evaluation. Therefore, the numerical properties of each subcy-
 448 cle update can be tailored to various purposes. Unless explicitly declared, the dynam-
 449 ical parameters in rk2 scheme is:

$$450 \quad U^* = U^n + \frac{1}{2} \Delta t \text{RHS}(U^n, N_g = 1, \beta = 0), \quad (28)$$

$$451 \quad U^{n+1} = U^n + \Delta t \text{RHS}(U^*, N_g = 3, \beta = 0). \quad (29)$$

453 The default rk2 configuration represents a dynamical core with the least operation counts
 454 in each time step and most implicit diffusion.

455 The default rk3 scheme is:

$$456 \quad U^{(1)} = U^n + \frac{1}{3} \Delta t \text{RHS}(U^n, N_g = 3, \beta = 1), \quad (30)$$

$$457 \quad U^{(2)} = U^n + \frac{1}{2} \Delta t \text{RHS}(U^{(1)}, N_g = 3, \beta = 1), \quad (31)$$

$$458 \quad U^{n+1} = U^n + \Delta t \text{RHS}(U^{(2)}, N_g = 3, \beta = 1). \quad (32)$$

461 The default rk3 configuration represents dynamical core with minimized implicit diffu-
 462 sion.

463 Although the rk2 scheme cost fewer operations in each full cycle, the rk3 scheme
 464 allows larger time steps. In practice, a fully optimized rk2 should still maintain better

465 computational efficiency over rk3, majorly due to the first-order substep is significantly
 466 cheaper than the standard high-order substep. The linearized Runge-Kutta schemes can
 467 highly optimize the computational memory storage cost since the values of RHS terms
 468 in each substep are not retained, and the storage of updated prognostic variables can be
 469 reused. Lastly, linearized rk3 only improves the CFL conditions and is 2nd-order accu-
 470 rate in time. Standard high-order accurate Runge-Kutta schemes can be found in X. Chen
 471 et al. (2013); Ullrich et al. (2010); C. Chen and Xiao (2008).

472 **4 Tests and results**

473 **4.1 Testing Plan**

474 Table 3 introduces the naming convention to label the model configurations for a
 475 shallow water test simulation. For example, a run label C48.g2.rk3.b1.00 stands for a
 476 simulation of a $48 \times 48 \times 6$ cubed-sphere grid with equiangular grid point distribution,
 477 and the discretization configuration is the rk3 scheme described in the previous subsec-
 478 tion. The value of the forward-backward parameter is 1, which is fully explicit. As de-
 479 scribed above, the default rk2 configuration not only uses fully implicit forward-backward
 480 pressure gradient evaluation but also minimizes the first substep complexity by using a
 481 1st-order accurate reconstruction scheme. The rk3 configuration implements a fully ex-
 482 plicit pressure gradient algorithm and uses 5-point-stencil reconstruction for all three sub-
 483 steps. Therefore, the rk2 and rk3 configurations represent the two extremes of the nu-
 484 merical diffusion and performance properties spectrums, with rk2 at the more compu-
 485 tationally efficient, more diffusive end, and vice versa. The diffusivities of other config-
 486 urations lie between the two ends.

487 Most conventional tests require the simulation data on a traditional latitude-longitude
 488 grid for analysis. Therefore, all cubed-sphere simulation results are remapped by a 1st-
 489 order conservative algorithm onto a 144×72 spherical grid, which is about 2.5-degree grid
 490 spacing to minimize regridding introduced artifacts.

491 The validation of this model contains three stages. The first stage employs the widely
 492 adopted Williamson et al. (1992) shallow-water test suite (W92) to match the conver-
 493 gence of the results to the literature. The smooth solutions in W92 also allow the val-
 494 idations of the order of accuracy and model's overall response to diffusion. The sensi-
 495 tivities of the model-specific parameters, such as grid choices, discretization configura-

Table 3. Naming convention to label the model configurations of a shallow water test simulation. For example, a run label C48.g2.rk3.b1.00 stands for a simulation with a 48x48x6 cubed-sphere grid with equal-angular tile grid point distribution, and the time advancing is a 3-step Runge-Kutta scheme, the value of the forward-backward parameter is 1, which is fully explicit.

Notation	Description
C[N]	Cubed-sphere grid with N cells along each side of the cubed sphere tile. $N \times N \times 6$ total grid cells. $N \in [48, 96, 192, 384, 768]$.
g0	Equi-edge grid
g2	Equiangular grid
rk2	2-substep time scheme with 1-point- and 5-point-stencil polynomial reconstruction in two substeps.
rk3	3-substep time scheme with 5-point-stencil polynomial reconstruction in all substeps
b[β]	The forward-backward pressure gradient algorithm control parameter $\beta \in [0, 1]$. (only appear when β value is non-default)

496 tions, beta values, are tested. In GCM development, the rotational mode plays a dom-
 497 inant role in large to mesoscale motions. Therefore in stage 2, the recently proposed modon
 498 test (Lin et al., 2017) is implemented to check the model’s quality in representing the
 499 vorticity. Last but not least, a new “splash test” inspired by X. Chen et al. (2018) is pro-
 500 posed in stage 3 to validate the model’s dispersion and dissipation properties. Minimiz-
 501 ing the phase speed errors at short wavelengths and maintaining scale-selective diffusion
 502 properties are vital for unstaggered algorithms.

503 The time step in each run configuration is set at the maximum allowed values that
 504 the simulations are stable in all resolutions. The courant number for LMARS based solver
 505 is estimated by:

$$506 \quad c_{\text{CFL}} = \frac{(a_{\text{max}} + a_{\text{min}}) \Delta t}{(\Delta A / \Delta x)_{\text{min}}}, \quad (33)$$

507 where a_{max} and a_{min} stand for the highest and lowest gravity wave speed evaluated at
 508 the initial condition, and $(\Delta A / \Delta x)_{\text{min}}$ is the shortest distance across a grid cell. Grant-
 509 ing that the maximum flow speed in LMARS should be less than the lowest gravity wave
 510 speed, the estimated courant number is an upper bound in the simulations. This def-

Table 4. Time step parameter `n_split` and the corresponding courant number in each test case. The courant numbers are associated with equi-edge grid configuration.

Test label	Test description	<code>n_split</code> (rk2)	<code>cfl</code> (g0.rk2)	<code>n_split</code> (rk3)	<code>cfl</code> (g0.rk3)
case1	Advection of a cosine bell	8		8	
case2	Steady-state geostrophic balanced flow	10	0.7	7	1
case5	Zonal flow over an isolated conical mountain	13	0.85	9	1.22
case6	Rossby-Haurwitz wave	19	0.81	13	1.18
modon	Colliding modons	11	1.02	7	1.61
splash	Splash on the sphere	2		2	

511 inition can be extended to the compressible 3D model by replacing the gravity wave speed
512 with acoustic wave speed. In all simulations, the dynamic time step Δt is calculated via:
513 $\Delta t = dt_atmos / (k_split \times n_split)$, where `dt_atmos`=3600 s is a base time step, the cy-
514 cling parameter `n_split` is unchanged in all resolutions, and `k_split` scales with resolutions
515 with values [1, 2, 4, 8, 16] corresponding to [C48, C96, C192, C384, C768]. Among all
516 parameters, the choice of the time-marching scheme is the most dominant factor in de-
517 termining the maximum allowed time steps. The equiangular grid allows slightly larger
518 time steps than the equi-edge grid. Table 4 lists the time step parameter `n_split` and the
519 corresponding courant numbers for all test cases.

520 Error norm measures follow the W92 in the height field h :

$$521 \quad l_1(h) = \frac{I(|h - h_T|)}{I(|h_T|)}, \quad (34)$$

$$522 \quad l_2(h) = \sqrt{\frac{I((h - h_T)^2)}{I(h_T^2)}}, \quad (35)$$

$$523 \quad l_\infty(h) = \frac{\max |h - h_T|}{\max |h_T|}, \quad (36)$$

524 with global mean operator:

$$525 \quad I(\eta) = \frac{\sum \eta \Delta A}{\sum \Delta A}, \quad (37)$$

528 where ΔA is the discretized area of the cell that variable η occupies, h_T is the true so-
 529 lution of fluid depth, which is estimated by most accurate C768.g2.rk3.b1.00 results if
 530 no analytical solution is available.

531 4.2 W92 shallow-water tests

532 In W92, test cases 1, 2, 5, 6 (See test names in Table 4) are widely used in global
 533 shallow-water solver development. These four tests are conducted with various config-
 534 urations and resolutions, as described in the testing plan. In particular, case 1 and 2 usu-
 535 ally tests different rotating angles. Since the solutions do not show significant dependency
 536 on the rotation directions, only 45-degree rotation results are presented for brevity. The
 537 45-degree advection of the cosine bell and the solid body rotation tests are labels as case1a45
 538 and case2a45.

539 Figure 4 is the l_1 , l_2 , and l_{inf} error norms plotted against the simulation time at
 540 C48 resolution. A general finding is that the errors of most non-stationary runs depend
 541 mostly on rk2 and rk3 differences rather than the grid type choices, indicating diffusion
 542 properties are the dominant factor in error growth. Case 1 uses constant flows, which
 543 do not evaluate the pressure gradient. Therefore, the results represent the errors solely
 544 due to advection schemes. Additionally, no sudden error spike is observed when the co-
 545 sine bell travels across cube-sphere tile boundaries in case 1. Thus, the singularities in
 546 a cubed-sphere geometry are sufficiently handled, and no grid imprinting is observed. In
 547 the solid-body rotation tests with stationary solutions, which are different from other
 548 tests, all the runs produce similar magnitudes of errors. In particular, the equi-edge grid
 549 (g0) produces slightly larger errors than the equiangular grid (g2). Lastly, in case 6, the
 550 error growth curves do not saturate to a steady number, indicating that the solutions
 551 remain in-phase (X. Chen et al., 2018) even after a significant period of simulation time.
 552

553 To determine the general order of accuracy in different configurations, Figure 5 plots
 554 the l_2 error against different resolutions at specific dates. The results indicate that rk3
 555 runs consistently maintain second-order overall accuracy, which is expected since no high-
 556 order multi-dimension scheme is employed in this work. The previous section explains
 557 that the forward-backward scheme (FB) is numerically equivalent to adding a 2nd-order
 558 stabilizing term to the advection equation, which will degrade the overall 2nd-order ac-

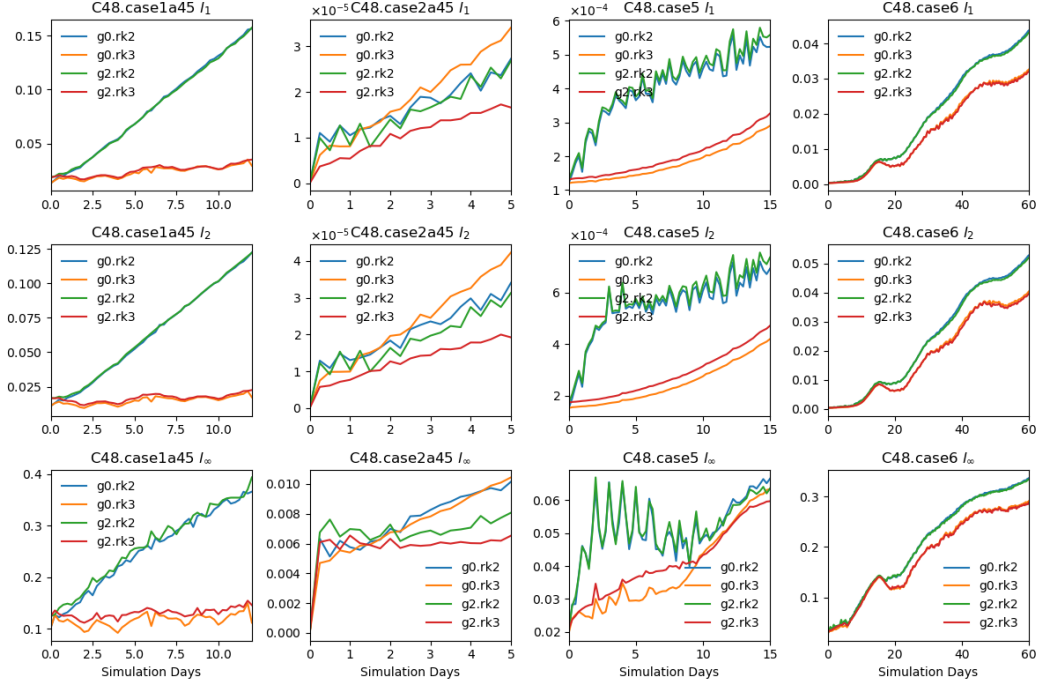


Figure 4. l_1 , l_2 and l_{inf} error norms growth with the simulation time of W92 test cases 1, 2, 5 and 6 at the C48 resolution.

559 accuracy. Therefore, in cases 5 and 6, rk2 runs, which employ a fully forward-backward
 560 pressure gradient algorithm, demonstrate lower than 2nd-order overall accuracy. Case
 561 1 does not involve the pressure gradient. Thus, it is not affected by FB settings. It ap-
 562 pears that the balanced stationary case 2 is also free of FB accuracy degradation.

563 A more in-depth analysis of FB impact is demonstrated in Figures 6 and 7. Inter-
 564 estingly, the overall order of accuracy gradually increases with higher beta values in Fig-
 565 ure 6. In figure 7, although all results have good convergence towards C768 high-resolution
 566 solutions, FB parameter β has a significant influence on the solver’s diffusion properties.
 567 The fully explicit C48.rk3.b1.00 run produces even higher maximum values (the small
 568 circle at the eastern equator) than the C768.rk3.b0.00 run with fully implicit pressure
 569 gradient evaluation.

570 The Rossby-Haurwitz test (case6) with a wavenumber four is adopted in various
 571 works. This test can validate the solvers’ robustness in preventing the instability due to
 572 truncation error in the initial conditions. Figure 8 shows the height field at day 14, 40,
 573 80 at resolutions C48 and C768 with rk2 and rk3 configurations. Only the equal-angular

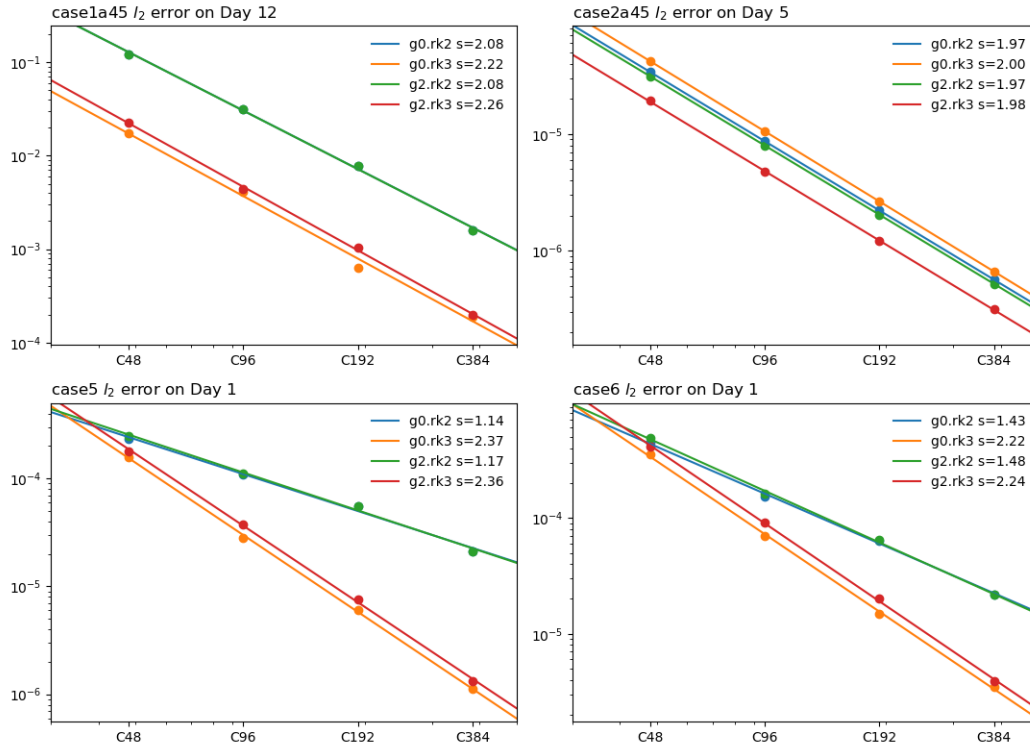


Figure 5. l_2 error against different resolutions at specific dates with different resolutions. The value of s in the legends are slopes of each line that indicates the overall order of accuracy.

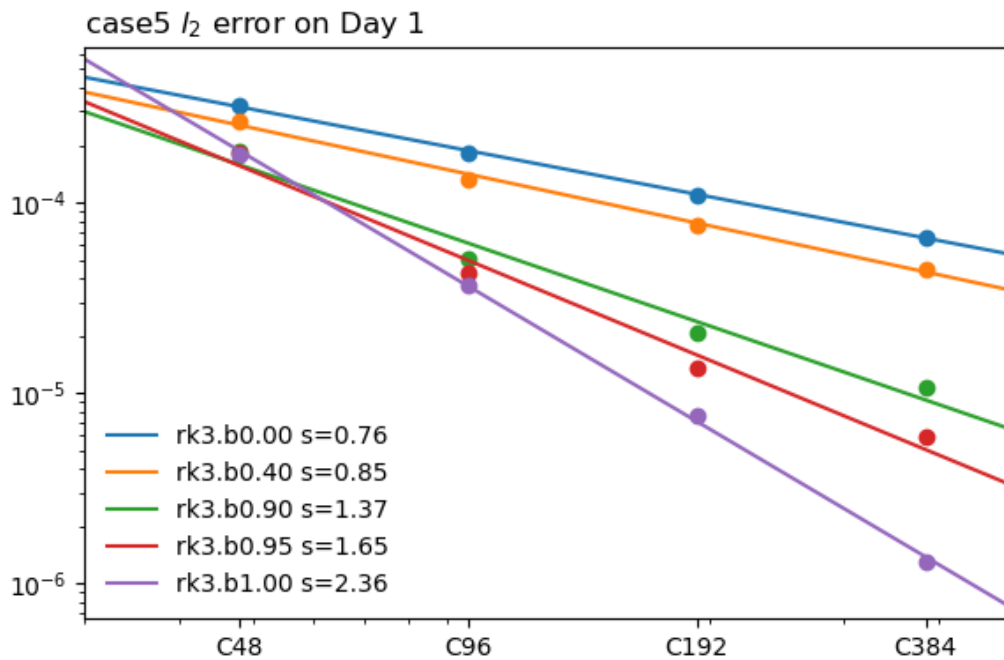


Figure 6. Same as Figure 5, but different beta values in case 5 are compared.

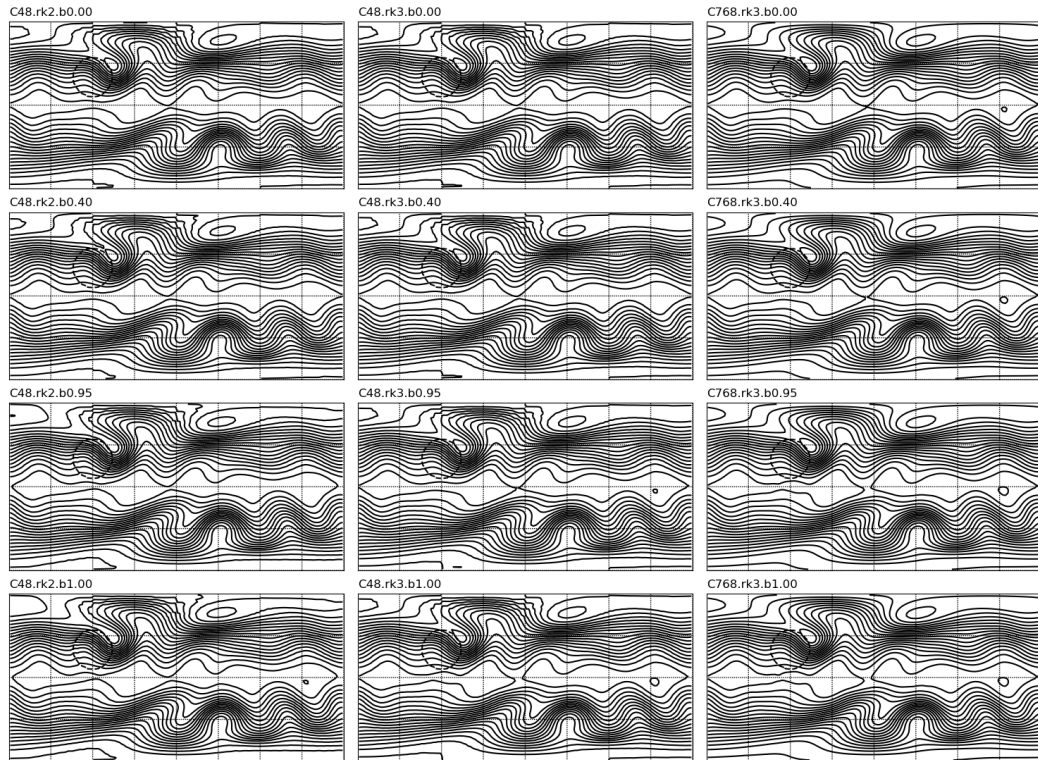


Figure 7. The final day flow height field of case 5 with C48 and C768 resolutions. Different configurations of rk2, rk3 and different strength of FB parameter β values are also compared. The dashed circle is the location of the conical mountain. The contour interval is 50 m.

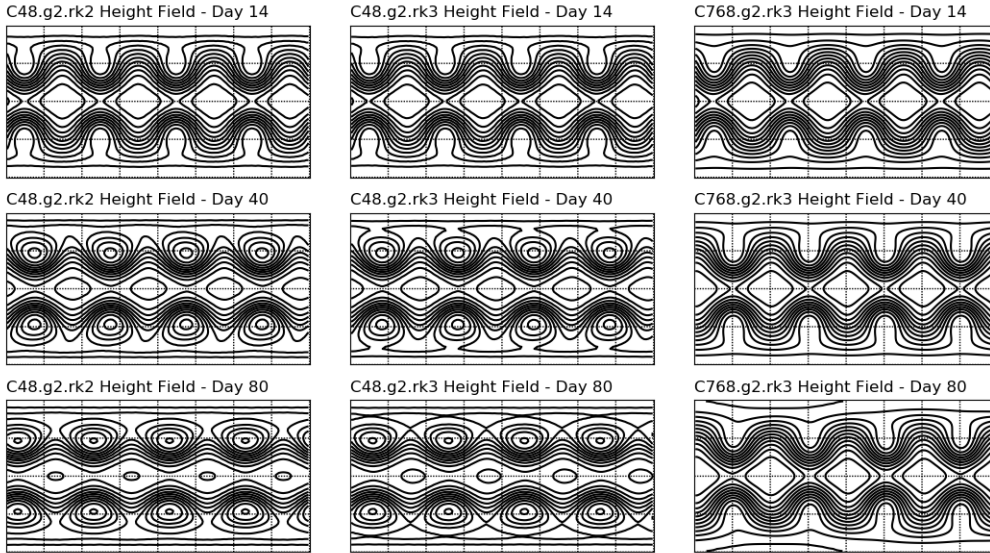


Figure 8. Height field at day 14, 40, 80 at resolutions C48 and C768 with rk2 and rk3 configurations. Only the equal-angular grid (g2) is displayed because no strong dependency from the grid type choices is found. The contour interval is 200 m.

574 grid is displayed because no strong dependency from the grid type choices is found. The
 575 solver achieves optimum symmetry for an extended simulation time of over 80 days. Al-
 576 though both being symmetric, the high-resolution C768 reference solutions maintain much
 577 better initial modal structures and intensity than the low-resolution solutions.

578 4.3 Colliding modons

579 The recently proposed colliding modons test (Lin et al., 2017; Zhang et al., 2019;
 580 Wang et al., 2019) evaluates the solver’s ability to simulate vorticity dynamics, which
 581 plays a dominant role in large to mesoscale motions. The colliding modon pairs can fully
 582 reach steady shapes after one day and travel back to approximately their original loca-
 583 tions at around day 100. A successful cycle can produce four symmetrical tracks in four
 584 quadrants, namely Q_{sw} , Q_{se} , Q_{nw} , Q_{ne} . The quality of the results can be evaluated by
 585 comparing the travel distances and amplitudes of the vortex.

586 Figure 9 demonstrates the colliding modons simulations with g2.rk3 configuration
 587 at various resolutions. The results show that the symmetry is well maintained in all runs.
 588 The simulations with C192 and better resolutions show good convergence. Figure 10 com-

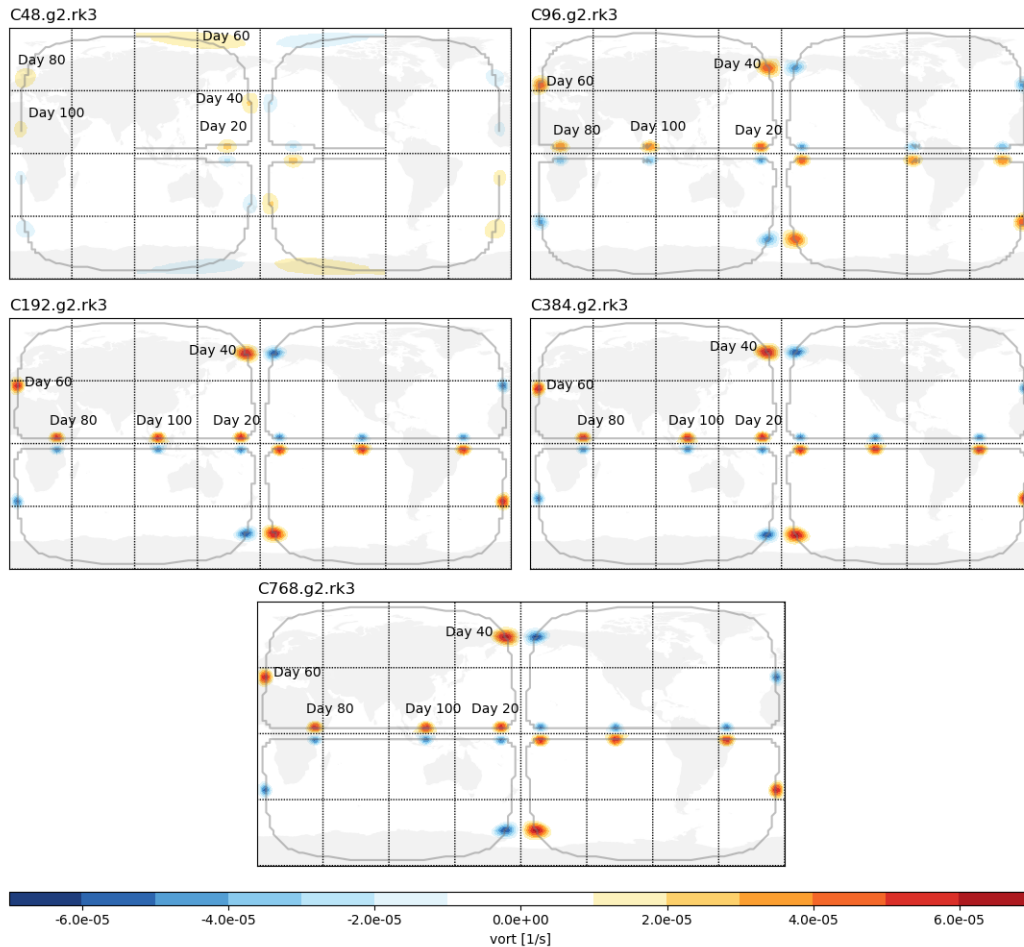


Figure 9. Colliding modons simulations with g2.rk3 configuration at various resolutions.

589 pares the travel distance and amplitude of the modons in the northwest quadrant at day
 590 100. Note that the travel distance is measured starting at the end of day 1 to ignore ini-
 591 tial adjustments. Although the grid choices, discretization configurations have impacts
 592 on both values, the resolution is the deterministic factor to resolve the modons move-
 593 ment correctly, and C192 and better resolutions result in converged values. The bar plots
 594 in Figure 10 provide a quantitative baseline for future development.

595 The colliding modons test provides an interesting perspective in atmospheric mod-
 596 eling applications. The spatial scale of each modon is at around 1000 km. The exper-
 597 iments show that although a 200 km resolution (C48) model can capture the motion of
 598 the modon, the speed is not correctly simulated, and the strength of the vortex is rapidly
 599 dissipated by model internal diffusion. Considering that many rotational processes that
 600 are of interest in global circulation models are of horizontal scales less than 1000 km, in-

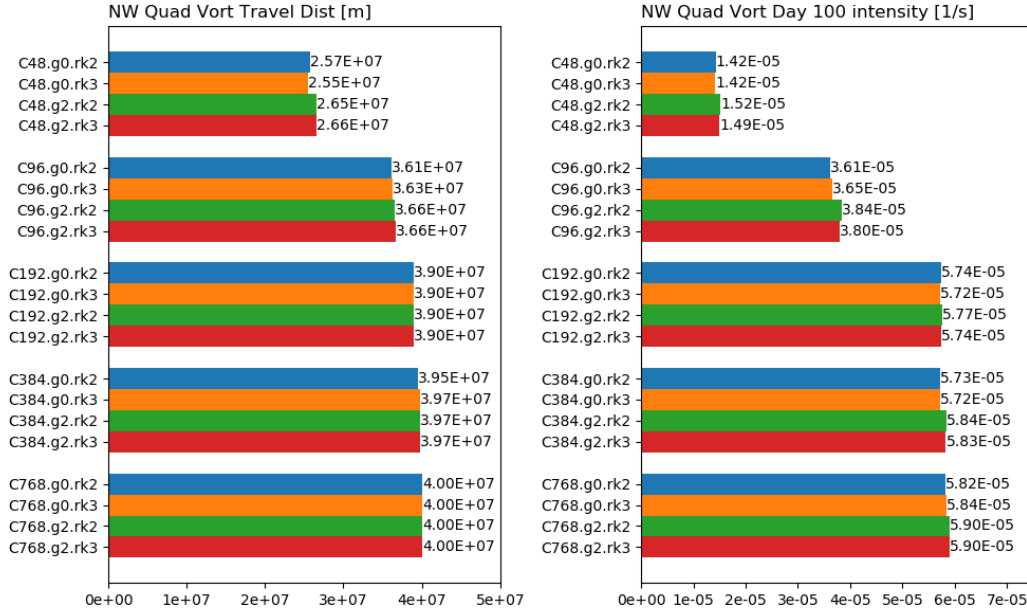


Figure 10. The travel distance and amplitude of the modons in the northwest quadrant at day 100. Note that the travel distance is measured starting at the end of day 1 to ignore initial adjustments.

601 creasing the model resolution may be the most effective way to improve the accuracy in
 602 simulating many rotational events such as cyclones and storms. Recent studies also sug-
 603 gest significant improvements in simulating atmospheric vortices by enhancing the model
 604 resolution. For example, Murakami et al. (2015) found that by improving resolution from
 605 50 to 25 km, the model can better capture categories 4 and 5 hurricanes. Gao et al. (2019)
 606 showed better hurricane structures by locally increasing the model resolution from 25km
 607 to 8km.

608 **4.4 Splash on the sphere**

609 Previous subsections cover a comprehensive range of numerical model properties
 610 such as the correctness, orders of accuracy, faithful vortex representation. This section
 611 validates the dispersion and dissipation properties at various wavelengths by introduc-
 612 ing a “splash on the sphere” test. Historically, unstaggered solvers are considered infe-
 613 rior in representing the short wave propagation due to poor dispersive properties. How-
 614 ever, such conclusions usually are based on the low-order linearized analysis, which does
 615 not reflect high-order complex real-world applications. By discretizing the high-order lin-

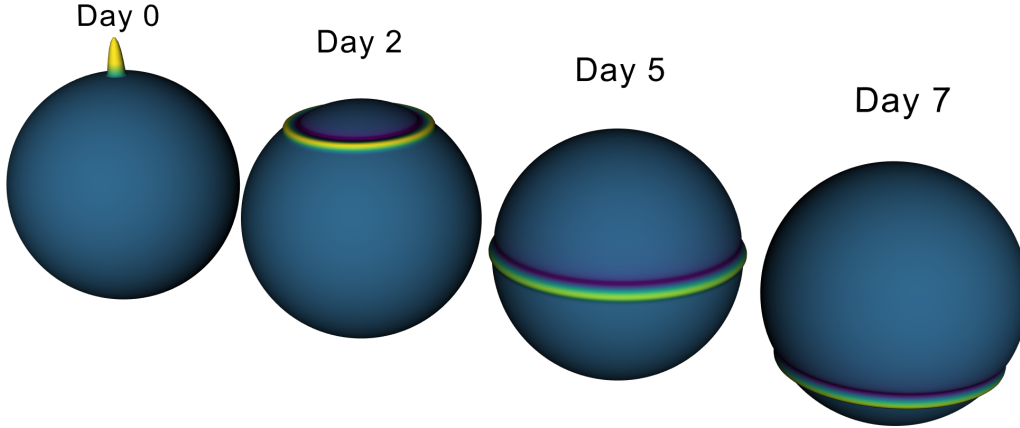


Figure 11. Exaggerated height field of the splash on the sphere test at Days 0, 2, 5, and 7.

616 earized analysis in Courant numbers and numerical phase, X. Chen et al. (2018) found
 617 the grid staggering choices have negligible phase speed influence in high-order algorithms.
 618 Furthermore, X. Chen et al. (2018) also introduced a simple 1D test to visualize the dis-
 619 persion behavior at short waves and the diffusion control of grid-scale noise. Inspired by
 620 this work, this section presents an extended 2D version of a “splash on the sphere” test
 621 to evaluate solver capabilities in faithfully represent short wave propagations.

622 The test has a simple physical process to splash a sinusoidal droplet at the North
 623 Pole and freely propagate on the non-rotational sphere. The choice of the sinusoidal sig-
 624 nal is to limit the waves in a single modal mode and test the sharp gradient between the
 625 perturbation and the background when a monotonic algorithm is implemented in the fu-
 626 ture. The Coriolis coefficient f and the topography are both zero, and the initial veloc-
 627 ity field is stationary. The height field with the initial splashing perturbation is defined:

$$628 \quad \Phi = \begin{cases} \Phi_0 + \Phi' \cos\left(\frac{\pi}{2} \frac{r}{R}\right) & \text{if } r < R, \\ \Phi_0 & \text{else,} \end{cases} \quad (38)$$

629 where r is the distance from the north pole, and $\Phi_0 = 50 \text{ m} \times G \approx (\pi R_e / 10 \text{ Day})^2$,
 630 $\Phi' = 1 \text{ m} \times G$, and $R = 500 \text{ km}$. The design of a 50 m background flow height allows
 631 the propagating waves to reach the South Pole at approximately ten days, which is an
 632 arbitrary choice. Figure 11 illustrates the exaggerated height field at Days 0, 2, 5, and
 633 7.

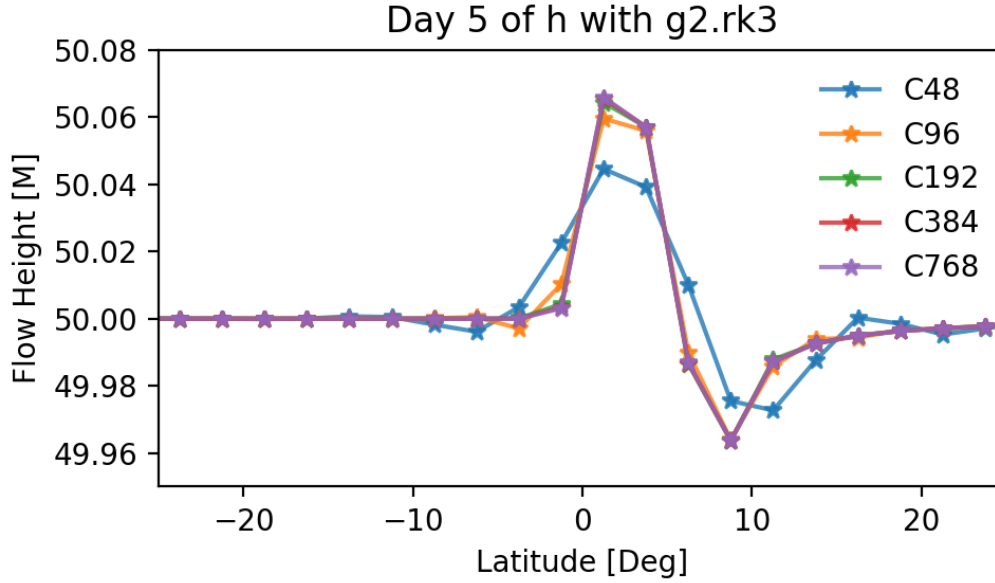


Figure 12. Day-5 snapshots in the meridional direction of g2.rk3 runs at various resolutions.

634 The analysis of this work focuses on day-5 snapshots when the splash waves prop-
 635 agate to the equatorial region. The results in all resolutions are regridded to 144×72
 636 latitude-longitude resolution. Figure 12 shows the day-5 snapshots in the meridional di-
 637 rection of g2.rk3 runs at various resolutions. All simulations propagate the splash at the
 638 same location, indicating no phase error is observed. The C48 run shows an obvious spread-
 639 ing of the wave due to the excessive diffusion at this wavelength. Since this work does
 640 not implement any monotonic algorithm, overshoots and undershoots are also observed
 641 in the results.

642 Figure 13 quantitatively compares day-5 snapshots of distances to the north pole
 643 (NP), peak flow height, and maximum zonal wind absolute values with different discretiza-
 644 tion settings, grid choices, and resolutions. The identical distances to NP indicate the
 645 solver’s excellent dispersive properties, which is highly desired with the unstaggered al-
 646 gorithm. In contrast to the modon tests, the peak flow height comparison shows an in-
 647 triguing observation that the model’s intrinsic diffusion properties have an even more
 648 significant influence on the results than the resolution differences. In the last column,
 649 a perfect numerical solver should not produce any zonal wind in this test. The non-zero
 650 values are due to the imperfect representation of the curvilinear cubed-sphere geome-
 651 try. Therefore, it is an excellent test to check the grid discretization performance. It is

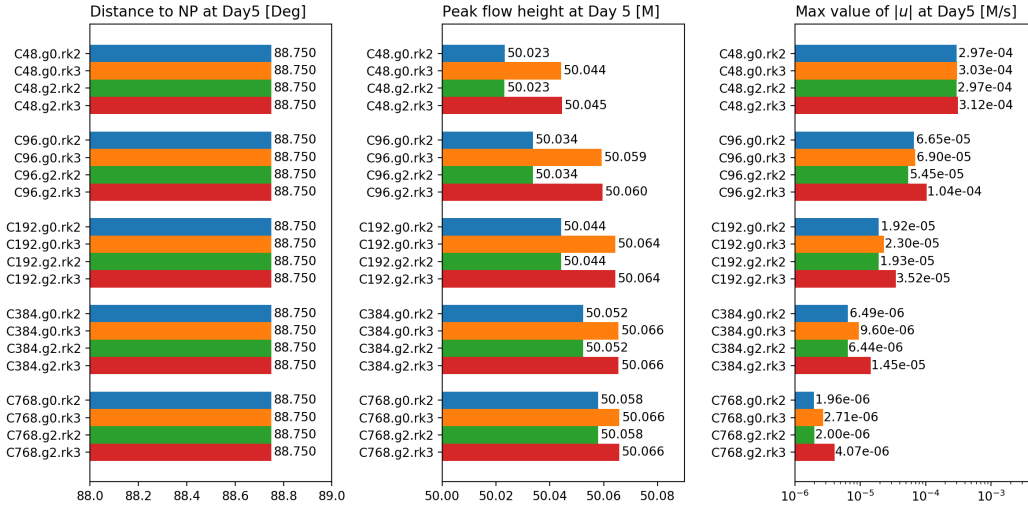


Figure 13. Day-5 snapshots of distances to the north pole (NP), peak flow height, and maximum zonal wind absolute values with different discretization settings, different grid choices, and resolutions.

reassuring to find that the different grid choices do not produce excessive discrepancies in geometric errors. The resolutions and discretization play more critical roles than grid choices.

This work only tests one splash configuration for brevity. In X. Chen et al. (2018), a square wave is also an informative setup to investigate sharp gradient handlings. In future work, a “square splash” can be an appealing option once more sophisticated local monotonic algorithms are included. The tracking of maximum zonal wind absolute values can be a useful gauge of high-order multi-dimension algorithms.

4.5 Discussion

The model demonstrates competitive performance in all numerical tests. Even without any explicit filter, the solver exhibits a broad range of organic implicit diffusion properties, mainly controlled by reconstruction stencil size and strength of forward-backward pressure gradient settings. Considering a full-fledged GCM is an interplay between numerical methods and highly uncertain physics parameterization, flexibility in diffusion control is helpful.

667 The results provide some perspectives in faithfully simulating various processes.
668 The rotational motions in the colliding modon tests and the propagation of character-
669 istics in the splash tests are both about a 1000-km spatial scale. Although the C48 sim-
670 ulations can capture both events, the qualities are significantly less reliable than those
671 of higher resolution counterparts. C96 is the recommended minimum resolution to ac-
672 curately represent these processes, which is about ten times grid-spacing. This guide-
673 line also indicates the unstaggered solver has balanced capabilities in resolving the ro-
674 tational mode, and the divergence mode.

675 Lastly, with the duo-grid system and the tile-edge remapping, the solver is free of
676 any grid imprinting issues. The grid-type choices show negligible differences in the so-
677 lutions compared to discretization differences and resolutions, which indicates the de-
678 sired consistency in grid choices for various purposes.

679 **5 Conclusions and future work**

680 In this work, we have successfully demonstrated the LMARS-based shallow-water
681 solver on two gnomonic cubed-sphere grids with controllable variations of computational
682 efficiency and diffusion properties. We use the W92 test suite to warrant the model to
683 produce results that converge to the literature. The model illustrates a broad range of
684 diffusion and controls the delicate balance between the order of accuracy and the robust-
685 ness by various dynamical core parameters. In particular cases, numerical tests demon-
686 strate that many resolvable processes are not necessarily reliable. We also designed a test
687 to isolate numerical properties by visualizing the dissipation and dispersion. Lastly, Griffies
688 (2004, Chap 17) discussed that explicit frictional operators might alter pressure gradi-
689 ent and angular momentum due to imbalanced design. With no explicit damping, the
690 control of implicit diffusion in this model is organic and does not cause artifacts in pres-
691 sure gradient calculations.

692 There are several new ideas in this work. We introduced the duo-grid system that
693 unifies arbitrary gnomonic cubed-sphere grid representations. It also provides the 1D align-
694 ment for arbitrary gnomonic grids at halo regions. This work also extends the L97 pressure-
695 gradient integration technique with LMARS diffusion contribution, resulting in a fast
696 and stable discretization. In the numerical test section, the extension of more quanti-
697 tive metrics to the modon tests allows straightforward comparison between different mod-

698 els and configurations. The splash on the sphere test offers an economical way to get 1D
 699 dispersion and dissipation properties of the model without extracting the schemes into
 700 a 1D testbed.

701 Balancing the computational performance and numerical accuracy is one of the top
 702 motivations in this development. Therefore, this work implements several optimizations.
 703 Some improvement does not sacrifice numerical accuracy. For example, the choice of unit-
 704 length basis vectors significantly simplifies the mathematical expressions of the curvi-
 705 linear system, thus avoiding the computational storage of redundant vector transforma-
 706 tion matrices. On the other hand, although halo region 1D remap can be made more so-
 707 phisticated with higher-order schemes, we choose the simple piecewise linear reconstruc-
 708 tion to maintain a minimum unbalanced workload in parallel computing. Lastly, a shallow-
 709 water testbed cannot determine the most optimal solver diffusion properties in a fully
 710 coupled GCM. Therefore, this work provides a guideline for a controllable range of or-
 711 ganic numerical properties once integrated into a full model.

712 The next step is the extension of this work to a 3D compressible atmosphere with
 713 the cubed-sphere grid. Previous work has implemented LMARS in a vertical 2D com-
 714 pressible atmosphere with both Eulerian and Lagrangian vertical coordinates (X. Chen
 715 et al., 2013). Li and Chen (2019) demonstrated an energy-conserving model with sim-
 716 ple microphysics under the LMARS Eulerian framework. Therefore, the LMARS 3D ex-
 717 tension on the cubed-sphere grid has several core components validated in various en-
 718 vironments. Another future topic is to include more sophisticated advection components,
 719 such as monotonic constraints (van Leer, 1979), high-order multi-dimension transport
 720 schemes (Lin & Rood, 1996) in the horizontal direction. With the vertical Lagrangian
 721 coordinates, this development shares substantial similarities with the FV3 framework,
 722 which can guide future research.

723 **Appendix A List of constants, symbols and their values and units**

724 To make the notations consistent and clear, Table A1 summarizes all important
 725 constants, symbols, their values and units in this work for reference.

Symbol	Description	Values	Units
G	Gravitational constant	9.80665	ms^{-2}
Ω	Rotational speed of the Earth	7.292e-5	s^{-1}

R	Radius of the Earth	6.3712e6	m
\hat{e}_λ	Unit vector in zonal direction	1	NA
\hat{e}_ϕ	Unit vector in meridional direction	1	NA
\hat{e}_1	Unit vector in x-direction (local to cubed-sphere tile)	1	NA
\hat{e}_2	Unit vector in y-direction (local to cubed-sphere tile)	1	NA
\hat{k}	Unit vector in sphere radius direction	1	NA
λ	Longitude		rad
ϕ	Latitude		rad
i, j	Indices to label grid points in x- and y-directions		NA
α	angle between two curvilinear coordinates		rad
g_{ij}	Covariant 2D metric tensor of the curvilinear grid system, note the ij in this context is the dimension iteration in Einstein Notation		NA
g^{ij}	Contra-variant 2D metric tensor of the curvilinear grid system		NA
h	Thickness of the fluid		m
Π	Thickness of the fluid in term of geopotential		m^2s^{-2}
Φ	Geopotential		m^2s^{-2}
Φ_s	Surface geopotential		m^2s^{-2}
\vec{u}	2D velocity vector		ms^{-1}
f	Coriolis parameter		s^{-1}
ζ	Vertical component of the relative vorticity		s^{-1}
u	Covariant wind component in x-direction		ms^{-1}
v	Covariant wind component in y-direction		ms^{-1}
\tilde{u}	Contra-variant wind component in x-direction		ms^{-1}
\tilde{v}	Contra-variant wind component in x-direction		ms^{-1}
g	Metric coefficient of the curvilinear geometry		NA
u_λ	Wind component in zonal direction		ms^{-1}
u_ϕ	Wind component in meridional direction		ms^{-1}
J^{c2l}	Matrix to convert (u, v) to (u_λ, u_ϕ)		NA
J^{l2c}	Matrix to convert (u_λ, u_ϕ) to (u, v)		NA
u_\perp^x	Wind projection perpendicular to cell interface in x-direction		ms^{-1}

u_{\parallel}^x	Wind projection parallel to cell interface in x-direction	ms^{-1}
u_{\perp}^y	Wind projection perpendicular to cell interface in y-direction	ms^{-1}
u_{\parallel}^y	Wind projection parallel to cell interface in y-direction	ms^{-1}
a	Gravity wave speed (group speed of the fluid)	ms^{-1}

Table A1: List of parameters and symbols used throughout this document

726 Appendix B Gnomonic projection initialization algorithms

727 This section provides a detailed mathematical reference-line based gnomonic cubed-
728 sphere generation process for reference.

729 B1 Basic geometric algorithms

730 Each gnomonic projection can be described by a 3D Cartesian vector $\vec{p}(x, y, z)$, which
731 is uniquely determined by a point on the sphere or a 3D vector on the spherical coordi-
732 nate with unit length $\vec{p}(\lambda, \phi)$. The valid information is the direction of the vector, and
733 the length of the vector is trivial. The conversion can be written:

$$734 \quad x = \cos \phi \cos \lambda, \quad (B1)$$

$$735 \quad y = \cos \phi \sin \lambda, \quad (B2)$$

$$736 \quad z = \sin \phi, \quad (B3)$$

739 and

$$740 \quad \lambda = \arctan \frac{y}{x}, \quad (B4)$$

$$741 \quad \phi = \arcsin \frac{z}{\sqrt{x^2 + y^2 + z^2}}, \quad (B5)$$

743 where the Fortran intrinsic functions `atan2()` is used to place λ in the range of $-\pi <$
744 $\lambda \leq \pi$.

745 To calculate the great circle distance between two points:

$$746 \quad \text{dist}(\vec{p}_1(\lambda_1, \phi_1), \vec{p}_2(\lambda_2, \phi_2)) = R \arccos \left(\frac{\vec{p}_1 \cdot \vec{p}_2}{|\vec{p}_1| |\vec{p}_2|} \right), \quad (B6)$$

747 or

$$748 \quad \text{dist}(\vec{p}_1(\lambda_1, \phi_1), \vec{p}_2(\lambda_2, \phi_2)) = R \arccos(\cos \phi_1 \cos \phi_2 \cos(\lambda_1 - \lambda_2) + \sin \phi_1 \sin \phi_2). \quad (\text{B7})$$

749 To calculate the area of a grid cell:

$$750 \quad \text{area}(\vec{p}_1, \vec{p}_2, \vec{p}_3, \vec{p}_4) = R^2(\alpha_{412} + \alpha_{123} + \alpha_{234} + \alpha_{341} - 2\pi), \quad (\text{B8})$$

751 where α_{ijk} is the angle between three points $(\vec{p}_i, \vec{p}_j, \vec{p}_k)$ with “right-hand rule” from \vec{p}_j ,
752 and can be calculated by:

$$753 \quad \alpha_{ijk} = \arccos\left(\frac{(\vec{p}_i \times \vec{p}_j) \cdot (\vec{p}_j \times \vec{p}_k)}{|\vec{p}_i \times \vec{p}_j| \cdot |\vec{p}_j \times \vec{p}_k|}\right). \quad (\text{B9})$$

754 The mid-point of two vectors \vec{p}_1 and \vec{p}_2 is:

$$755 \quad \text{mid}(\vec{p}_1, \vec{p}_2) = \frac{\vec{p}_1 + \vec{p}_2}{2}. \quad (\text{B10})$$

756 **B2 Initializing gnomonic projection with reference lines on tile one**

757 As illustrated in Fig. 3, the eight corners of the tiles in 3D Cartesian coordinates
758 are $(x, y, z) = (\pm 1, \pm 1, \pm 1)$. The resolution of the cubed-sphere grid is denoted by $C[N]$,
759 which indicates $N \times N \times 6$ total grid cells. Let the first tile be centered at $(\lambda, \phi) =$
760 $(0, 0)$ or the cube-tile with vertices $(x, y, z) = (1, \pm 1, \pm 1)$ and denote (X, Y) the local
761 coordinates on this cube-tile, the 3D Cartesian coordinates can be written by:

$$762 \quad (x, y, z) = (1, X, Y), \quad (\text{B11})$$

763 and the projection vector can be also written $\vec{p}(X, Y)$. Additionally, let (i, j) be the in-
764 dices of the grid points on tile one, and the indices start counting from 1. Therefore, the
765 coordinate sets (x, y, z) , (λ, ϕ) , (X, Y) and (i, j) are interchangeable and representing the
766 same gnomonic projection vector. The vertices on the tile can be uniquely determined
767 by a column of Y values on the cube tile surface.

768 **B21 Equidistance projection**

769 To get the Y values of the red reference column:

$$770 \quad Y(i_{\text{ref}}, j) = -1 + (j - 1) \delta h, \quad (\text{B12})$$

771 where $\delta h = 2/N$, $i_{\text{ref}} = N/2 + 1$. Then the red reference row is:

$$772 \quad X(i, j_{\text{ref}}) = Y(i_{\text{ref}}, i), \quad (\text{B13})$$

773 where $i_{\text{ref}} = N/2 + 1$, and the grid mesh on the cube tile can be populated from the
 774 two reference lines accordingly:

$$775 \quad X(i, j) = X(i, j_{\text{ref}}) = Y(i_{\text{ref}}, i), \quad (\text{B14})$$

$$776 \quad Y(i, j) = Y(i_{\text{ref}}, j). \quad (\text{B15})$$

777 Therefore, $\vec{p}(X, Y)$ can be easily converted to $\vec{p}(x, y, z)$ and $\vec{p}(\lambda, \phi)$, and the grid points
 778 on the cubed-sphere tile is generated. One may observe that the values of i_{ref} and j_{ref}
 779 are trivial
 780

781 ***B22 Equiangular projection***

782 Comparing to equidistance projection, the equiangular grid generation requires an
 783 extra first step to project grid points from the green reference column to the cube tile
 784 and get the Y values. The angular step of the grid points on the green row is:

$$785 \quad \delta\zeta = \frac{2\alpha_{\text{ref}}}{N}, \quad (\text{B16})$$

786 where $\alpha_{\text{ref}} = \pi/4$. Then the Y values are:

$$787 \quad Y(i_{\text{ref}}, j) = R_{\text{ref}} \tan((j - 1)\delta\zeta - \alpha_{\text{ref}}), \quad (\text{B17})$$

788 where $R_{\text{ref}} = 1$. Then the entire set of grid points on the tile can be populated follow-
 789 ing the same procedure as the equidistance projection.

790 ***B23 Equi-edge projection***

791 The procedures to generate the equi-edge projection are identical to the equian-
 792 gular projection except different parameters: $\alpha_{\text{ref}} = \arcsin(\sqrt{3})$, $R_{\text{ref}} = \sqrt{2}$.

793 **B3 Populating grid points to six tiles**

794 Once the grid points on tile one are generated, the points on the rest of the tiles
 795 can be populated using the “staircase” tile-interlock pattern. The basic rotations to any
 796 3D vector can be decomposed by the combination of the rotations about each axes of
 797 the Cartesian coordinate system. The rotation about each axes by an angle β following
 798 right-hand rule:

$$799 \quad R_x(\beta) = \begin{pmatrix} 1 & 0 & 0 \\ 0 & \cos \beta & -\sin \beta \\ 0 & \sin \beta & \cos \beta \end{pmatrix}, \quad (\text{B18})$$

$$R_y(\beta) = \begin{pmatrix} \cos \beta & 0 & \sin \beta \\ 0 & 1 & 0 \\ -\sin \beta & 0 & \cos \beta \end{pmatrix}, \quad (B19)$$

$$R_z(\beta) = \begin{pmatrix} \cos \beta & -\sin \beta & 0 \\ \sin \beta & \cos \beta & 0 \\ 0 & 0 & 1 \end{pmatrix}. \quad (B20)$$

In particular,

$$R_x(90^\circ) = \begin{pmatrix} 1 & 0 & 0 \\ 0 & 0 & -1 \\ 0 & 1 & 0 \end{pmatrix}, \quad (B21)$$

$$R_y(90^\circ) = \begin{pmatrix} 0 & 0 & 1 \\ 0 & 1 & 0 \\ -1 & 0 & 0 \end{pmatrix}, \quad (B22)$$

$$R_z(90^\circ) = \begin{pmatrix} 0 & -1 & 0 \\ 1 & 0 & 0 \\ 0 & 0 & 1 \end{pmatrix}. \quad (B23)$$

Therefore, the rotations for each tile:

$$\vec{p}(i, j; \text{tile} = 2) = R_z(90^\circ) \vec{p}(i, j; \text{tile} = 1), \quad (B24)$$

$$\vec{p}(i, j; \text{tile} = 3) = R_x(90^\circ) R_z(90^\circ) \vec{p}(i, j; \text{tile} = 1), \quad (B25)$$

$$\vec{p}(i, j; \text{tile} = 4) = R_x(90^\circ) R_z(180^\circ) \vec{p}(i, j; \text{tile} = 1), \quad (B26)$$

$$\vec{p}(i, j; \text{tile} = 5) = R_y(90^\circ) R_z(270^\circ) \vec{p}(i, j; \text{tile} = 1), \quad (B27)$$

$$\vec{p}(i, j; \text{tile} = 6) = R_y(90^\circ) \vec{p}(i, j; \text{tile} = 1), \quad (B28)$$

or:

$$\vec{p}(i, j; \text{tile} = 1) = [1, X, Y], \quad (B29)$$

$$\vec{p}(i, j; \text{tile} = 2) = [-X, 1, Y], \quad (B30)$$

$$\vec{p}(i, j; \text{tile} = 3) = [-X, -Y, 1], \quad (B31)$$

$$\vec{p}(i, j; \text{tile} = 4) = [-1, -Y, -X], \quad (B32)$$

$$\vec{p}(i, j; \text{tile} = 5) = [Y, -1, -X], \quad (B33)$$

$$\vec{p}(i, j; \text{tile} = 6) = [Y, X, -1]. \quad (B34)$$

Appendix C The governing equations

This shallow water model employs the vector-invariant form governing equations:

$$\frac{\partial h}{\partial t} = -\nabla \cdot (h\vec{u}), \quad (\text{C1})$$

$$\frac{\partial \vec{u}}{\partial t} = -(\zeta + f)\vec{k} \times \vec{u} - \nabla \left((\Pi + \Phi_s) + \frac{1}{2}\vec{u} \cdot \vec{u} \right), \quad (\text{C2})$$

where

$$\Pi = Gh, \quad (\text{C3})$$

$$\zeta = \hat{k} \cdot (\nabla \times \vec{u}), \quad (\text{C4})$$

$$f = 2\Omega \sin \phi. \quad (\text{C5})$$

The definition of the variables, constants, and their values are summarized in Table A1.

C1 Generic form in a curvilinear grid system

This solver uses covariant wind components as the prognostic variable. The covariant wind components are the projections of the wind vector on the curvilinear coordinates:

$$u = \vec{u} \cdot \hat{e}_1, \quad (\text{C6})$$

$$v = \vec{u} \cdot \hat{e}_2, \quad (\text{C7})$$

and the corresponding contra-variant wind components satisfy:

$$\vec{u} = \tilde{u}\hat{e}_1 + \tilde{v}\hat{e}_2. \quad (\text{C8})$$

A covariant 2D metric tensor g_{ij} of the curvilinear grid system on a tile of the cubed-sphere is defined by Einstein Notation:

$$g_{ij} = \hat{e}_i \cdot \hat{e}_j, \quad (\text{C9})$$

with the metric coefficient:

$$g = \det(g_{ij}). \quad (\text{C10})$$

Note \hat{e}_i and \hat{e}_j in the Einstein Notation are iterations along dimensions \hat{e}_1 and \hat{e}_2 . The contra-variant 2D metric tensor g^{ij} is the inverse of g_{ij} , and the conversions between covariant and contra-variant vector component are:

$$\begin{bmatrix} u \\ v \end{bmatrix} = g_{ij} \begin{bmatrix} \tilde{u} \\ \tilde{v} \end{bmatrix}, \quad (\text{C11})$$

861

862

$$\begin{bmatrix} \tilde{u} \\ \tilde{v} \end{bmatrix} = g^{ij} \begin{bmatrix} u \\ v \end{bmatrix}. \quad (\text{C12})$$

863

C2 The choice of the basis vectors and the optimizations

864

865

866

867

868

The choice of the definition of \hat{e}_1 and \hat{e}_2 are flexible. Modelers made various definitions of these terms in the literature. To yield concise mathematical expressions in numerical discretization, the covariant unit vectors are set to unit length in space, or $|\hat{e}_1| = |\hat{e}_2| = 1$. Thus, the values at the each grid point (i, j) on a cubed-sphere tile can be calculated in a discretized form:

869

$$(\hat{e}_1)_{i,j} = \frac{(\hat{k}_{i,j} \times \hat{k}_{i+1,j}) \times \hat{k}_{i,j}}{\left| (\hat{k}_{i,j} \times \hat{k}_{i+1,j}) \times \hat{k}_{i,j} \right|}, \quad (\text{C13})$$

870

871

$$(\hat{e}_2)_{i,j} = \frac{(\hat{k}_{i,j} \times \hat{k}_{i,j+1}) \times \hat{k}_{i,j}}{\left| (\hat{k}_{i,j} \times \hat{k}_{i,j+1}) \times \hat{k}_{i,j} \right|}, \quad (\text{C14})$$

872

with:

873

$$\hat{k}(\lambda, \phi) = \begin{bmatrix} \cos \phi \cos \lambda \\ \cos \phi \sin \lambda \\ \sin \phi \end{bmatrix}. \quad (\text{C15})$$

874

875

This algorithm to determine \hat{e}_1 and \hat{e}_2 offers better flexibility when constructing various implementations of the cubed-sphere grids.

876

877

Define α the angle between two local curvilinear coordinates, or the unit vectors \hat{e}_1 and \hat{e}_2 on a cubed-sphere tile, it yields:

878

$$\sin \alpha = \hat{k} \cdot (\hat{e}_1 \times \hat{e}_2), \quad (\text{C16})$$

879

880

$$\cos \alpha = \hat{e}_1 \cdot \hat{e}_2. \quad (\text{C17})$$

881

882

Note that discrete grid subscripts i, j are omitted for cleaner expression, since all variables are co-located.

883

This set of basis produces concise mathematical forms of the metric tensors:

884

$$g_{ij} = \begin{bmatrix} 1 & \cos \alpha \\ \cos \alpha & 1 \end{bmatrix}, \quad (\text{C18})$$

885

886

$$g^{ij} = \frac{1}{\sin^2 \alpha} \begin{bmatrix} 1 & -\cos \alpha \\ -\cos \alpha & 1 \end{bmatrix}, \quad (\text{C19})$$

887

888

$$\sqrt{g} = \sin \alpha. \quad (\text{C20})$$

889 **C3 Conversions of vector components to the regular latitude-longitude**
 890 **coordinates**

891 The latitude-longitude basis vectors are:

$$892 \hat{e}_\lambda(\lambda, \phi) = \frac{1}{\cos \phi} \frac{\partial \hat{k}}{\partial \lambda} = \begin{bmatrix} -\sin \lambda \\ \cos \lambda \\ 0 \end{bmatrix}, \quad (\text{C21})$$

$$893 \hat{e}_\phi(\lambda, \phi) = \frac{\partial \hat{k}}{\partial \phi} = \begin{bmatrix} -\sin \phi \cos \lambda \\ -\sin \phi \sin \lambda \\ \cos \phi \end{bmatrix}, \quad (\text{C22})$$

895 and define the regular zonal and meridional wind components u_λ and u_θ . The conver-
 896 sion matrices are:

$$897 J^{c2l} = \begin{bmatrix} \hat{e}_1 \cdot \hat{e}_\lambda & \hat{e}_2 \cdot \hat{e}_\lambda \\ \hat{e}_1 \cdot \hat{e}_\phi & \hat{e}_2 \cdot \hat{e}_\phi \end{bmatrix} g^{ij}, \quad (\text{C23})$$

$$898 J^{l2c} = \frac{g_{ij}}{\det(J^{c2l})} \begin{bmatrix} J_{11}^{c2l} & -J_{12}^{c2l} \\ -J_{21}^{c2l} & J_{22}^{c2l} \end{bmatrix}, \quad (\text{C24})$$

900 with the conversion relations:

$$901 \begin{bmatrix} u_\lambda \\ v_\phi \end{bmatrix} = J^{c2l} \begin{bmatrix} u \\ v \end{bmatrix}, \quad (\text{C25})$$

$$902 \begin{bmatrix} u \\ v \end{bmatrix} = J^{l2c} \begin{bmatrix} u_\lambda \\ v_\phi \end{bmatrix}. \quad (\text{C26})$$

904 **C4 Conversions of vector components to the local orthogonal coordi-**
 905 **nates at cell interfaces**

906 The preparation of the Riemann solver requires the wind vectors to be projected
 907 to the local orthogonal coordinates at the cell interfaces. Therefore, at cell interfaces in
 908 x-direction:

$$909 u_\perp^x = \tilde{u} \sin \alpha, \quad (\text{C27})$$

$$910 u_\parallel^x = \tilde{u} \cos \alpha + \tilde{v} = v, \quad (\text{C28})$$

912 or:

$$913 \begin{bmatrix} u_\perp^x \\ u_\parallel^x \end{bmatrix} = \begin{bmatrix} \sin \alpha & 0 \\ \cos \alpha & 1 \end{bmatrix} \begin{bmatrix} \tilde{u} \\ \tilde{v} \end{bmatrix}, \quad (\text{C29})$$

914 with inversion:

$$915 \begin{bmatrix} \tilde{u} \\ \tilde{v} \end{bmatrix} = \begin{bmatrix} \frac{1}{\sin \alpha} & 0 \\ -\frac{\cos \alpha}{\sin \alpha} & 1 \end{bmatrix} \begin{bmatrix} u_{\perp}^x \\ u_{\parallel}^x \end{bmatrix} \quad (\text{C30})$$

916 At cell interfaces in y-direction:

$$917 u_{\perp}^y = \tilde{v} \sin \alpha, \quad (\text{C31})$$

918

$$919 u_{\parallel}^x = \tilde{v} \cos \alpha + \tilde{u} = u, \quad (\text{C32})$$

920 or:

$$921 \begin{bmatrix} u_{\perp}^y \\ u_{\parallel}^y \end{bmatrix} = \begin{bmatrix} 0 & \sin \alpha \\ 1 & \cos \alpha \end{bmatrix} \begin{bmatrix} \tilde{u} \\ \tilde{v} \end{bmatrix}, \quad (\text{C33})$$

922 with inversion:

$$923 \begin{bmatrix} \tilde{u} \\ \tilde{v} \end{bmatrix} = \begin{bmatrix} -\frac{\cos \alpha}{\sin \alpha} & 1 \\ \frac{1}{\sin \alpha} & 0 \end{bmatrix} \begin{bmatrix} u_{\perp}^y \\ u_{\parallel}^y \end{bmatrix} \quad (\text{C34})$$

924 A small optimization can be observed from the above subsections. With basis vec-
 925 tors \hat{e}_1 and \hat{e}_2 being restricted to unit length, many vector conversions can be carried
 926 out with simple operations using pre-calculated values of $\sin \alpha$ and $\cos \alpha$. Therefore, the
 927 model saves considerable memory storage and computational cost by dropping many met-
 928 ric matrices and reducing operation counts. Moreover, the metric terms generation are
 929 more flexible in arbitrary gnomonic projections and simpler than most of the literature.

930 C5 Projecting the governing equations to the curvilinear coordinates

931 Projecting the continuity equation and the vector-invariance form momentum equa-
 932 tion to the curvilinear coordinates yields:

$$933 \frac{\partial h}{\partial t} = -\frac{1}{\sqrt{g}} \left(\frac{\partial}{\partial x} (\sqrt{g} h \tilde{u}) + \frac{\partial}{\partial y} (\sqrt{g} h \tilde{v}) \right), \quad (\text{C35})$$

$$934 \frac{\partial u}{\partial t} = \sqrt{g} \hat{v} (\zeta + f) - \frac{\partial}{\partial x} (\Pi + \Phi_s + K), \quad (\text{C36})$$

$$935 \frac{\partial v}{\partial t} = -\sqrt{g} \hat{u} (\zeta + f) - \frac{\partial}{\partial y} (\Pi + \Phi_s + K), \quad (\text{C37})$$

937 with the relative vorticity and the kinetic energy defined by:

$$938 \zeta = \frac{1}{\sqrt{g}} \left(\frac{\partial v}{\partial x} - \frac{\partial u}{\partial y} \right), \quad (\text{C38})$$

$$939 K = \frac{1}{2} (u \tilde{u} + v \tilde{v}). \quad (\text{C39})$$

940

941 These two terms can be further rearranged and optimized with better finite-volume
942 representations in the numerical discretization process.

943 **Acknowledgments**

944 The author wants to thank Lucas Harris and Stephen Griffies for the constructive GFDL
945 internal reviews. All materials used in this work are stored through GFDL’s Archiving
946 System at the location “/archive/Xi.Chen/PAPERS/2020.JAMES.SW/data” and can
947 be obtained by contacting GFDL or the author. This report was prepared by Xi Chen
948 under award NA18OAR4320123 from the National Oceanic and Atmospheric Admin-
949 istration, U.S. Department of Commerce. The statements, findings, conclusions, and rec-
950 ommendations are those of the author(s) and do not necessarily reflect the views of the
951 National Oceanic and Atmospheric Administration, or the U.S. Department of Commerce.

952 **References**

- 953 Adcroft, A., Anderson, W., Balaji, V., Blanton, C., Bushuk, M., Dufour, C. O.,
954 ... Zhang, R. (2019, 10). The GFDL Global Ocean and Sea Ice Model
955 OM4.0: Model Description and Simulation Features. *Journal of Ad-
956 vances in Modeling Earth Systems*, 11(10), 3167–3211. Retrieved from
957 <https://onlinelibrary.wiley.com/doi/abs/10.1029/2019MS001726> doi:
958 10.1029/2019MS001726
- 959 Adcroft, A., Campin, J.-M., Hill, C., & Marshall, J. (2004, 12). Implementation
960 of an Atmosphere-Ocean General Circulation Model on the Expanded Spher-
961 ical Cube. *Monthly Weather Review*, 132(12), 2845–2863. Retrieved from
962 <http://dx.doi.org/10.1175/MWR2823.1> doi: 10.1175/MWR2823.1
- 963 Arakawa, A., & Lamb, V. R. (1977, 1). Computational design of the basic dynamical
964 processes of the UCLA general circulation model. *Methods in computational
965 physics*, 17, 173–265.
- 966 Bourke, W. (1972, 9). An Efficient, One-Level, Primitive-Equation Spectral
967 Model. *Monthly Weather Review*, 100(9), 683–689. Retrieved from [http://
968 journals.ametsoc.org/doi/abs/10.1175/1520-0493%281972%29100%
969 3C0683%3AAAEOPSM%3E2.3.CO%3B2](http://journals.ametsoc.org/doi/abs/10.1175/1520-0493%281972%29100%3C0683%3AAAEOPSM%3E2.3.CO%3B2) doi: 10.1175/1520-0493(1972)100<0683:
970 AEOPSM>2.3.CO;2
- 971 Bourke, W. (1974, 10). A Multi-Level Spectral Model. I. Formulation and

- 972 Hemispheric Integrations. *Monthly Weather Review*, 102(10), 687–
973 701. Retrieved from [http://journals.ametsoc.org/doi/abs/10.1175/](http://journals.ametsoc.org/doi/abs/10.1175/1520-0493%281974%29102%3C0687%3AAMLSMI%3E2.0.CO%3B2)
974 1520-0493%281974%29102%3C0687%3AAMLSMI%3E2.0.CO%3B2 doi: 10.1175/
975 1520-0493(1974)102(0687:AMLSMI)2.0.CO;2
- 976 Chen, C., & Xiao, F. (2008, 5). Shallow water model on cubed-sphere by multi-
977 moment finite volume method. *Journal of Computational Physics*, 227(10),
978 5019–5044. Retrieved from [https://linkinghub.elsevier.com/retrieve/](https://linkinghub.elsevier.com/retrieve/pii/S0021999108000570)
979 [pii/S0021999108000570](https://linkinghub.elsevier.com/retrieve/pii/S0021999108000570) doi: 10.1016/j.jcp.2008.01.033
- 980 Chen, X., Andronova, N., Van Leer, B., Penner, J. E., Boyd, J. P., Jablonowski, C.,
981 & Lin, S.-J. (2013, 7). A Control-Volume Model of the Compressible Euler
982 Equations with a Vertical Lagrangian Coordinate. *Monthly Weather Review*,
983 141(7), 2526–2544. Retrieved from [http://journals.ametsoc.org/doi/abs/](http://journals.ametsoc.org/doi/abs/10.1175/MWR-D-12-00129.1)
984 10.1175/MWR-D-12-00129.1 doi: 10.1175/MWR-D-12-00129.1
- 985 Chen, X., Lin, S.-J., & Harris, L. M. (2018, 9). Towards an Unstaggered Finite-
986 Volume Dynamical Core With a Fast Riemann Solver: 1-D Linearized Analysis
987 of Dissipation, Dispersion, and Noise Control. *Journal of Advances in Modeling*
988 *Earth Systems*, 10(9), 2333–2356. Retrieved from [http://doi.wiley.com/](http://doi.wiley.com/10.1029/2018MS001361)
989 10.1029/2018MS001361 doi: 10.1029/2018MS001361
- 990 Du, Q., Gunzburger, M. D., & Ju, L. (2003, 8). Voronoi-based finite volume meth-
991 ods, optimal Voronoi meshes, and PDEs on the sphere. *Computer Methods in*
992 *Applied Mechanics and Engineering*, 192(35-36), 3933–3957. Retrieved from
993 <https://linkinghub.elsevier.com/retrieve/pii/S0045782503003943>
994 doi: 10.1016/S0045-7825(03)00394-3
- 995 Gao, K., Harris, L., Chen, J.-H., Lin, S.-J., & Hazelton, A. (2019, 1). Improving
996 AGCM Hurricane Structure With Two-Way Nesting. *Journal of Advances in*
997 *Modeling Earth Systems*, 11(1), 278–292. Retrieved from [http://doi.wiley](http://doi.wiley.com/10.1029/2018MS001359)
998 [.com/10.1029/2018MS001359](http://doi.wiley.com/10.1029/2018MS001359) doi: 10.1029/2018MS001359
- 999 Giraldo, F., Hesthaven, J., & Warburton, T. (2002, 9). Nodal High-Order Discontin-
1000 uous Galerkin Methods for the Spherical Shallow Water Equations. *Journal of*
1001 *Computational Physics*, 181(2), 499–525. Retrieved from [https://linkinghub](https://linkinghub.elsevier.com/retrieve/pii/S0021999102971391)
1002 [.elsevier.com/retrieve/pii/S0021999102971391](https://linkinghub.elsevier.com/retrieve/pii/S0021999102971391) doi: 10.1006/jcph.2002
1003 .7139
- 1004 Griffies, S. (2004). *Fundamentals of Ocean Climate Models*. Princeton, N.J:

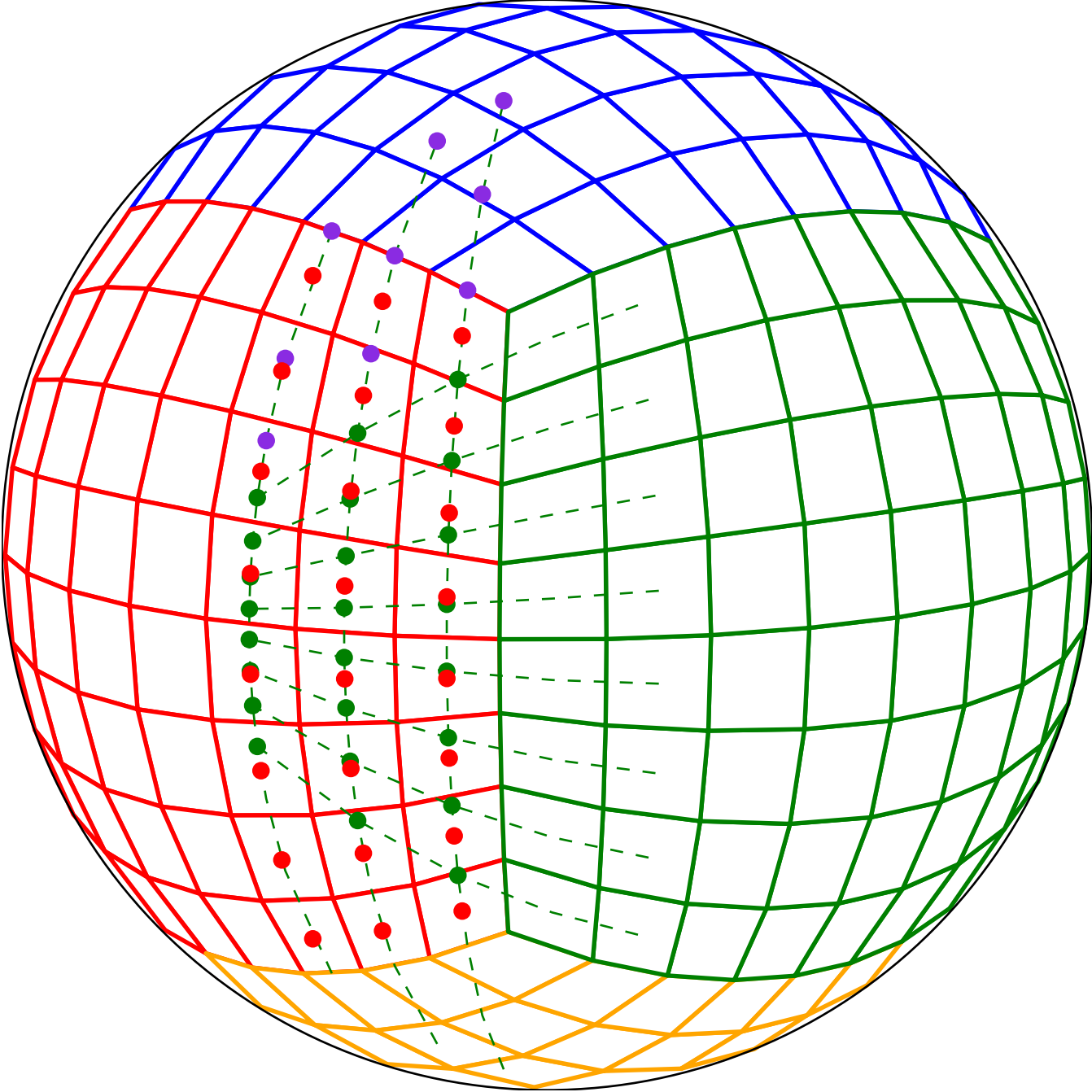
- 1005 Princeton University Press. Retrieved from [https://www.amazon.com/
1006 Fundamentals-Climate-Models-Stephen-Griffies-dp-0691118922/dp/
1007 0691118922/ref=mt_hardcover?encoding=UTF8&me=&qid=1591938681](https://www.amazon.com/Fundamentals-Climate-Models-Stephen-Griffies-dp-0691118922/dp/0691118922/ref=mt_hardcover?encoding=UTF8&me=&qid=1591938681)
- 1008 Harris, L. M., & Lin, S.-J. (2013, 1). A Two-Way Nested Global-Regional Dynamical Core on the Cubed-Sphere Grid. *Monthly Weather Review*, *141*(1), 283–
1009 306. Retrieved from [http://journals.ametsoc.org/doi/abs/10.1175/MWR-D
1010 -11-00201.1](http://journals.ametsoc.org/doi/abs/10.1175/MWR-D-11-00201.1) doi: 10.1175/MWR-D-11-00201.1
- 1012 Harris, L. M., Lin, S.-J., & Tu, C. (2016, 3). High-Resolution Climate Simulations Using GFDL HiRAM with a Stretched Global Grid. *Journal of Climate*, *29*(11), 4293–4314. Retrieved from [http://dx.doi.org/10.1175/
1013 JCLI-D-15-0389.1](http://dx.doi.org/10.1175/JCLI-D-15-0389.1) doi: 10.1175/JCLI-D-15-0389.1
- 1016 Katta, K. K., Nair, R. D., & Kumar, V. (2015, 7). High-Order Finite-Volume Transport on the Cubed Sphere: Comparison between 1D and 2D Reconstruction Schemes. *Monthly Weather Review*, *143*(7), 2937–2954. Retrieved from <http://dx.doi.org/10.1175/MWR-D-13-00176.1>
1017 [https://
1018 journals.ametsoc.org/mwr/article/143/7/2937/72256/HighOrder
1019 -FiniteVolume-Transport-on-the-Cubed](https://journals.ametsoc.org/mwr/article/143/7/2937/72256/HighOrder-FiniteVolume-Transport-on-the-Cubed) doi: 10.1175/MWR-D-13-00176.1
- 1022 Khamayseh, A., & Mastin, C. (1996). Computational Conformal Mapping for Surface Grid Generation. *Journal of Computational Physics*, *123*(2), 394–401. Retrieved from [http://www.sciencedirect.com/science/article/pii/
1023 S0021999196900327](http://www.sciencedirect.com/science/article/pii/S0021999196900327) doi: <http://dx.doi.org/10.1006/jcph.1996.0032>
- 1026 Li, C., & Chen, X. (2019, 2). Simulating Nonhydrostatic Atmospheres on Planets (SNAP): Formulation, Validation, and Application to the Jovian Atmosphere. *The Astrophysical Journal Supplement Series*, *240*(2), 37. Retrieved from <https://iopscience.iop.org/article/10.3847/1538-4365/aafdaa> doi:
1027 [10.3847/1538-4365/aafdaa](https://iopscience.iop.org/article/10.3847/1538-4365/aafdaa)
- 1031 Lin, S.-J. (1997, 7). A finite-volume integration method for computing pressure gradient force in general vertical coordinates. *Quarterly Journal of the Royal Meteorological Society*, *123*(542), 1749–1762. Retrieved from [http://doi.wiley
1032 .com/10.1002/qj.49712354214](http://doi.wiley.com/10.1002/qj.49712354214) doi: 10.1002/qj.49712354214
- 1035 Lin, S.-J. (2004, 10). A “Vertically Lagrangian” Finite-Volume Dynamical Core for Global Models. *Monthly Weather Review*, *132*(10), 2293–2307. Retrieved
1036 from [http://journals.ametsoc.org/doi/abs/10.1175/1520-0493\(2004\)
1037](http://journals.ametsoc.org/doi/abs/10.1175/1520-0493(2004)132<2293:VLLC;1-0;FT=1)

- 1038 132<2293:AVLFDC>2.0.CO;2 doi: 10.1175/1520-0493(2004)132<2293:
1039 AVLFDC>2.0.CO;2
- 1040 Lin, S.-J., Harris, L., Chen, X., Yao, W., & Chai, J. (2017, 11). Colliding Mod-
1041 ons: A Nonlinear Test for the Evaluation of Global Dynamical Cores. *Jour-
1042 nal of Advances in Modeling Earth Systems*, 9(7), 2483–2492. Retrieved
1043 from <http://dx.doi.org/10.1002/2017MS000965>[http://doi.wiley.com/
1044 10.1002/2017MS000965](http://doi.wiley.com/10.1002/2017MS000965) doi: 10.1002/2017MS000965
- 1045 Lin, S.-J., & Rood, R. B. (1996, 9). Multidimensional Flux-Form Semi-Lagrangian
1046 Transport Schemes. *Monthly Weather Review*, 124(9), 2046–2070. Re-
1047 trieved from [https://doi.org/10.1175/1520-0493\(1996\)
1048 MFFSLT%3E2.0.CO%3B2](https://doi.org/10.1175/1520-0493(1996)124%3C2046:MFFSLT%3E2.0.CO%3B2)[http://0.0.0.2http://journals.ametsoc.org/doi/
1049 abs/10.1175/1520-0493\(1996\)124%3C2046%3AMFFSLT%3E2.0.CO%3B2](http://0.0.0.2http://journals.ametsoc.org/doi/abs/10.1175/1520-0493(1996)124%3C2046%3AMFFSLT%3E2.0.CO%3B2) doi:
1050 10.1175/1520-0493(1996)124<2046:MFFSLT>2.0.CO;2
- 1051 McGregor, J. L. (1996, 6). Semi-Lagrangian Advection on Conformal-Cubic Grids.
1052 *Monthly Weather Review*, 124(6), 1311–1322. Retrieved from [http://
1053 journals.ametsoc.org/doi/abs/10.1175/1520-0493%281996%29124%
1054 3C1311%3ASLAOCC%3E2.0.CO%3B2](http://journals.ametsoc.org/doi/abs/10.1175/1520-0493%281996%29124%3C1311%3ASLAOCC%3E2.0.CO%3B2) doi: 10.1175/1520-0493(1996)124<1311:
1055 SLAOC>2.0.CO;2
- 1056 Mesinger, F. (1977). Forward-backward scheme, and its use in a limited area model.
1057 *Contrib. Atmos. Phys.*, 50, 200–210.
- 1058 Murakami, H., Vecchi, G. A., Underwood, S., Delworth, T. L., Wittenberg, A. T.,
1059 Anderson, W. G., ... Zeng, F. (2015, 12). Simulation and Prediction of
1060 Category 4 and 5 Hurricanes in the High-Resolution GFDL HiFLOR Cou-
1061 pled Climate Model. *Journal of Climate*, 28(23), 9058–9079. Retrieved from
1062 <http://journals.ametsoc.org/doi/10.1175/JCLI-D-15-0216.1> doi:
1063 10.1175/JCLI-D-15-0216.1
- 1064 Putman, W. M., & Lin, S.-J. (2007, 11). Finite-volume transport on various cubed-
1065 sphere grids. *Journal of Computational Physics*, 227(1), 55–78. Retrieved from
1066 <http://www.sciencedirect.com/science/article/pii/S0021999107003105>
1067 doi: 10.1016/j.jcp.2007.07.022
- 1068 Rančić, M., Purser, R. J., & Mesinger, F. (1996, 4). A global shallow-water
1069 model using an expanded spherical cube: Gnomonic versus conformal coor-
1070 dinates. *Quarterly Journal of the Royal Meteorological Society*, 122(532),

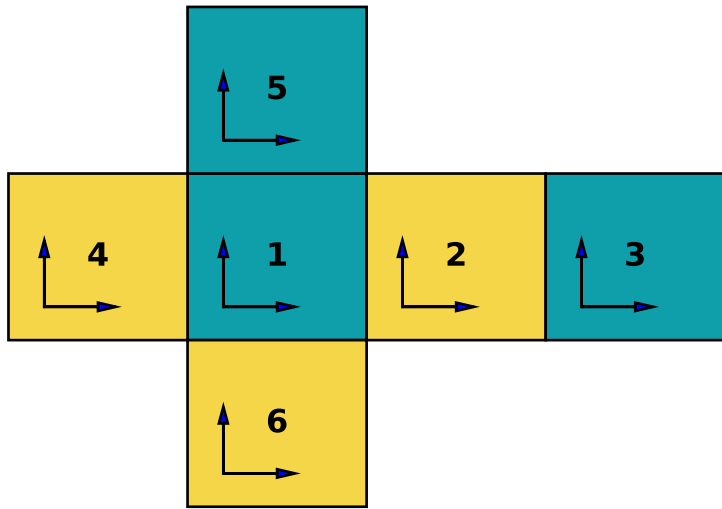
- 1071 959–982. Retrieved from <http://dx.doi.org/10.1002/qj.49712253209> doi:
 1072 10.1002/qj.49712253209
- 1073 Ringler, T. D., Heikes, R. P., & Randall, D. A. (2000, 7). Modeling the At-
 1074 mospheric General Circulation Using a Spherical Geodesic Grid: A New
 1075 Class of Dynamical Cores. *Monthly Weather Review*, 128(7), 2471–2490.
 1076 Retrieved from [http://journals.ametsoc.org/doi/full/10.1175/
 1077 1520-0493%282000%29128%3C2471%3AMTAGCU%3E2.0.CO%3B2](http://journals.ametsoc.org/doi/full/10.1175/1520-0493%282000%29128%3C2471%3AMTAGCU%3E2.0.CO%3B2) doi: 10.1175/
 1078 1520-0493(2000)128(2471:MTAGCU)2.0.CO;2
- 1079 Rípodas, P., Gassmann, A., Förstner, J., Majewski, D., Giorgetta, M., Korn, P.,
 1080 ... Heinze, T. (2009, 12). Icosahedral Shallow Water Model (ICOSWM):
 1081 results of shallow water test cases and sensitivity to model parameters. *Geo-
 1082 scientific Model Development*, 2(2), 231–251. Retrieved from [https://
 1083 www.geosci-model-dev.net/2/231/2009/](https://www.geosci-model-dev.net/2/231/2009/) doi: 10.5194/gmd-2-231-2009
- 1084 Ronchi, C., Iacono, R., & Paolucci, P. (1996, 3). The “Cubed Sphere”: A New
 1085 Method for the Solution of Partial Differential Equations in Spherical Geom-
 1086 etry. *Journal of Computational Physics*, 124(1), 93–114. Retrieved from
 1087 <https://linkinghub.elsevier.com/retrieve/pii/S0021999196900479>
 1088 doi: 10.1006/jcph.1996.0047
- 1089 Rossmanith, J. A. (2006, 4). A wave propagation method for hyperbolic sys-
 1090 tems on the sphere. *Journal of Computational Physics*, 213(2), 629–658.
 1091 Retrieved from [http://www.sciencedirect.com/science/article/pii/
 1092 S0021999105003967](http://www.sciencedirect.com/science/article/pii/S0021999105003967) doi: <http://dx.doi.org/10.1016/j.jcp.2005.08.027>
- 1093 Sadourny, R. (1972, 2). Conservative Finite-Difference Approximations of the Prim-
 1094 itive Equations on Quasi-Uniform Spherical Grids. *Monthly Weather Review*,
 1095 100(2), 136–144. Retrieved from [http://journals.ametsoc.org/doi/abs/10.
 1096 .1175/1520-0493%281972%29100%3C0136%3ACFAOTP%3E2.3.CO%3B2](http://journals.ametsoc.org/doi/abs/10.1175/1520-0493%281972%29100%3C0136%3ACFAOTP%3E2.3.CO%3B2) doi: 10
 1097 .1175/1520-0493(1972)100(0136:CFAOTP)2.3.CO;2
- 1098 Sadourny, R., Arakawa, A., & Mintz, Y. (1968, 6). Integration of the nondiver-
 1099 gent barotropic vorticity equation with an icosahedral-hexagonal grid for
 1100 the sphere. *Monthly Weather Review*, 96(6), 351–356. Retrieved from
 1101 [http://journals.ametsoc.org/doi/abs/10.1175/1520-0493\(1968\)
 1102 096%3C0351:IOTNBV%3E2.0.CO;2](http://journals.ametsoc.org/doi/abs/10.1175/1520-0493(1968)096%3C0351:IOTNBV%3E2.0.CO;2) doi: 10.1175/1520-0493(1968)096(0351:
 1103 IOTNBV)2.0.CO;2

- 1104 Satoh, M., Stevens, B., Judt, F., Khairoutdinov, M., Lin, S.-J., Putman, W. M.,
 1105 & Düben, P. (2019, 5). Global Cloud-Resolving Models. *Current Climate*
 1106 *Change Reports*. Retrieved from [http://link.springer.com/10.1007/](http://link.springer.com/10.1007/s40641-019-00131-0)
 1107 [s40641-019-00131-0](http://link.springer.com/10.1007/s40641-019-00131-0) doi: 10.1007/s40641-019-00131-0
- 1108 Stevens, B., Satoh, M., Auger, L., Biercamp, J., Bretherton, C. S., Chen, X., ...
 1109 Zhou, L. (2019, 9). DYAMOND: the DYnamics of the Atmospheric general
 1110 circulation Modeled On Non-hydrostatic Domains. *Progress in Earth and*
 1111 *Planetary Science*, 6(1), 61. Retrieved from [https://progearthplanetsci](https://progearthplanetsci.springeropen.com/articles/10.1186/s40645-019-0304-z)
 1112 [.springeropen.com/articles/10.1186/s40645-019-0304-z](https://progearthplanetsci.springeropen.com/articles/10.1186/s40645-019-0304-z) doi:
 1113 10.1186/s40645-019-0304-z
- 1114 Taylor, M. A., & Fournier, A. (2010, 8). A compatible and conservative spectral
 1115 element method on unstructured grids. *Journal of Computational Physics*,
 1116 229(17), 5879–5895. Retrieved from [https://linkinghub.elsevier.com/](https://linkinghub.elsevier.com/retrieve/pii/S0021999110001841)
 1117 [retrieve/pii/S0021999110001841](https://linkinghub.elsevier.com/retrieve/pii/S0021999110001841) doi: 10.1016/j.jcp.2010.04.008
- 1118 Taylor, M. A., Guba, O., Steyer, A., Ullrich, P. A., Hall, D. M., & Eldrid, C. (2020,
 1119 1). An Energy Consistent Discretization of the Nonhydrostatic Equations in
 1120 Primitive Variables. *Journal of Advances in Modeling Earth Systems*, 12(1).
 1121 Retrieved from [https://onlinelibrary.wiley.com/doi/abs/10.1029/](https://onlinelibrary.wiley.com/doi/abs/10.1029/2019MS001783)
 1122 [2019MS001783](https://onlinelibrary.wiley.com/doi/abs/10.1029/2019MS001783) doi: 10.1029/2019MS001783
- 1123 Tomita, H., Tsugawa, M., Satoh, M., & Goto, K. (2001, 12). Shallow Water
 1124 Model on a Modified Icosahedral Geodesic Grid by Using Spring Dynam-
 1125 ics. *Journal of Computational Physics*, 174(2), 579–613. Retrieved from
 1126 <https://linkinghub.elsevier.com/retrieve/pii/S0021999101968974>
 1127 doi: 10.1006/jcph.2001.6897
- 1128 Ullrich, P. A., Jablonowski, C., & van Leer, B. (2010, 8). High-order finite-
 1129 volume methods for the shallow-water equations on the sphere. *Journal*
 1130 *of Computational Physics*, 229(17), 6104–6134. Retrieved from [http://](http://www.sciencedirect.com/science/article/pii/S0021999110002317)
 1131 www.sciencedirect.com/science/article/pii/S0021999110002317 doi:
 1132 10.1016/j.jcp.2010.04.044
- 1133 van Leer, B. (1979, 7). Towards the ultimate conservative difference scheme.
 1134 V. A second-order sequel to Godunov’s method. *Journal of Computational*
 1135 *Physics*, 32(1), 101–136. Retrieved from [http://linkinghub.elsevier.com/](http://linkinghub.elsevier.com/retrieve/pii/0021999179901451)
 1136 [retrieve/pii/0021999179901451](http://linkinghub.elsevier.com/retrieve/pii/0021999179901451) doi: 10.1016/0021-9991(79)90145-1

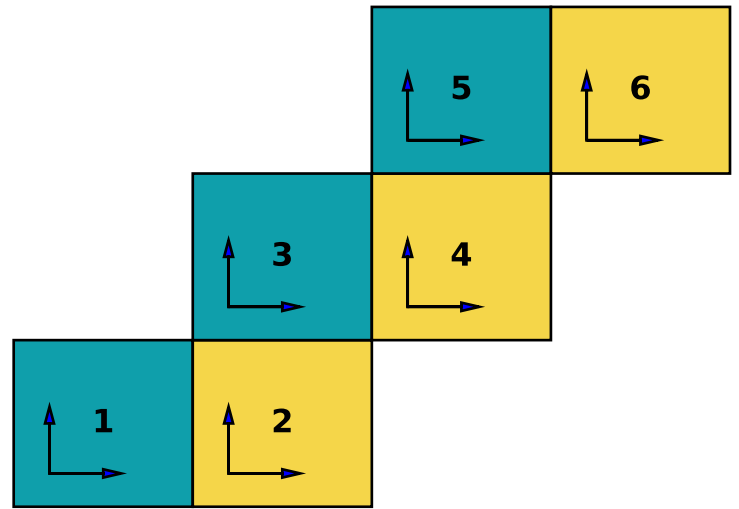
- 1137 Wang, L., Zhang, Y., Li, J., Liu, Z., & Zhou, Y. (2019, 12). Understanding the
 1138 Performance of an Unstructured-Mesh Global Shallow Water Model on Kinetic
 1139 Energy Spectra and Nonlinear Vorticity Dynamics. *Journal of Meteorological*
 1140 *Research*, *33*(6), 1075–1097. Retrieved from [http://link.springer.com/](http://link.springer.com/10.1007/s13351-019-9004-2)
 1141 [10.1007/s13351-019-9004-2](http://link.springer.com/10.1007/s13351-019-9004-2) doi: 10.1007/s13351-019-9004-2
- 1142 Williamson, D. L. (1968, 11). Integration of the barotropic vorticity equation on
 1143 a spherical geodesic grid. *Tellus*, *20*(4), 642–653. Retrieved from [http://](http://tellusa.net/index.php/tellusa/article/view/10044)
 1144 tellusa.net/index.php/tellusa/article/view/10044 doi: 10.1111/j.2153
 1145 -3490.1968.tb00406.x
- 1146 Williamson, D. L., Drake, J. B., Hack, J. J., Jakob, R., & Swarztrauber, P. N.
 1147 (1992, 9). A standard test set for numerical approximations to the shallow wa-
 1148 ter equations in spherical geometry. *Journal of Computational Physics*, *102*(1),
 1149 211–224. Retrieved from [https://linkinghub.elsevier.com/retrieve/pii/](https://linkinghub.elsevier.com/retrieve/pii/S0021999105800166)
 1150 [S0021999105800166](https://linkinghub.elsevier.com/retrieve/pii/S0021999105800166) doi: 10.1016/S0021-9991(05)80016-6
- 1151 Yang, C., Cao, J., & Cai, X.-C. (2010, 1). A Fully Implicit Domain Decomposition
 1152 Algorithm for Shallow Water Equations on the Cubed-Sphere. *SIAM Journal*
 1153 *on Scientific Computing*, *32*(1), 418–438. Retrieved from [http://epubs.siam](http://epubs.siam.org/doi/abs/10.1137/080727348)
 1154 [.org/doi/abs/10.1137/080727348](http://epubs.siam.org/doi/abs/10.1137/080727348) doi: 10.1137/080727348
- 1155 Zhang, Y., Li, J., Yu, R., Zhang, S., Liu, Z., Huang, J., & Zhou, Y. (2019, 6).
 1156 A Layer-Averaged Nonhydrostatic Dynamical Framework on an Unstruc-
 1157 tured Mesh for Global and Regional Atmospheric Modeling: Model De-
 1158 scription, Baseline Evaluation, and Sensitivity Exploration. *Journal of*
 1159 *Advances in Modeling Earth Systems*, *11*(6), 1685–1714. Retrieved from
 1160 <https://onlinelibrary.wiley.com/doi/abs/10.1029/2018MS001539> doi:
 1161 [10.1029/2018MS001539](https://onlinelibrary.wiley.com/doi/abs/10.1029/2018MS001539)
- 1162 Zhou, L., Lin, S.-J., Chen, J.-H., Harris, L. M., Chen, X., & Rees, S. L. (2019,
 1163 7). Toward Convective-Scale Prediction within the Next Generation Global
 1164 Prediction System. *Bulletin of the American Meteorological Society*, *100*(7),
 1165 1225–1243. Retrieved from [http://journals.ametsoc.org/doi/10.1175/](http://journals.ametsoc.org/doi/10.1175/BAMS-D-17-0246.1)
 1166 [BAMS-D-17-0246.1](http://journals.ametsoc.org/doi/10.1175/BAMS-D-17-0246.1) doi: 10.1175/BAMS-D-17-0246.1



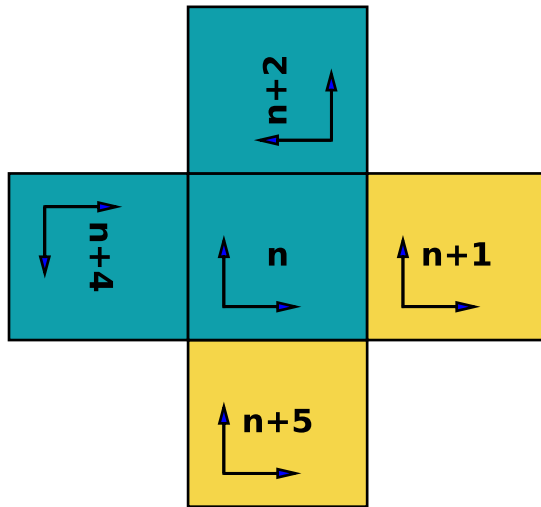
a) tropic belt logical arrangement



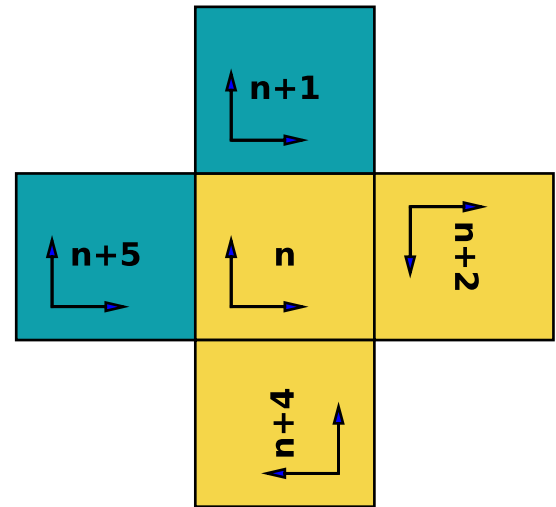
b) staircase logical arrangement

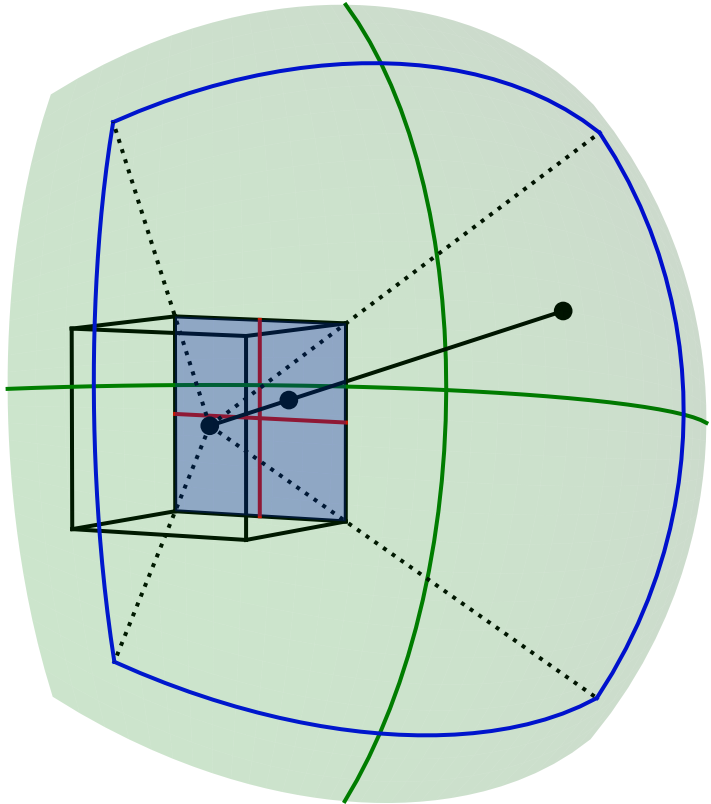


c) odd tile neighbor rotation

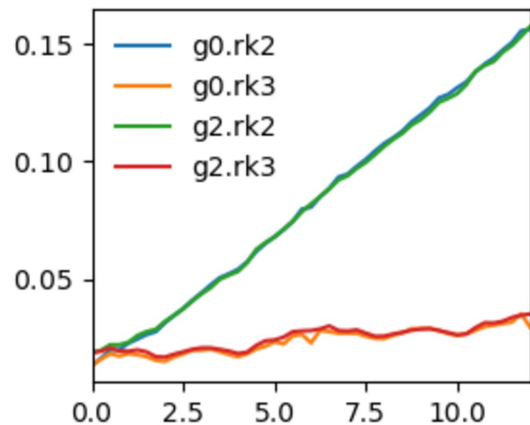
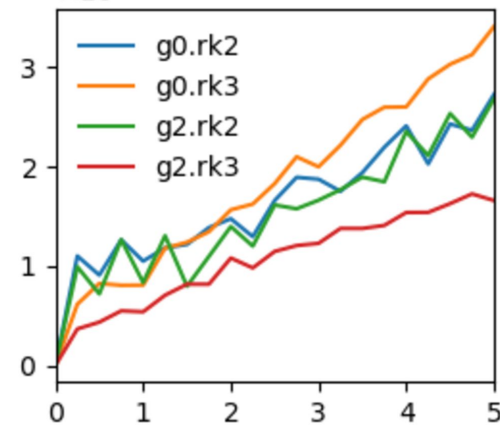
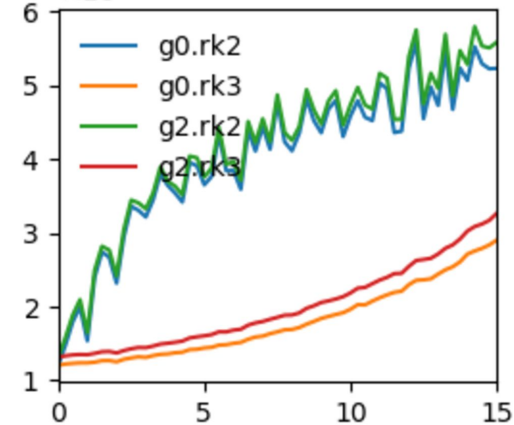
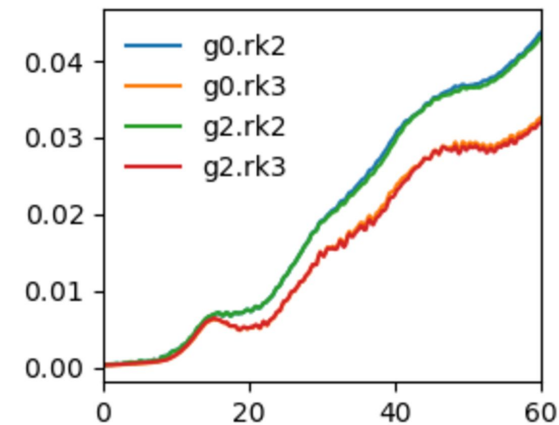
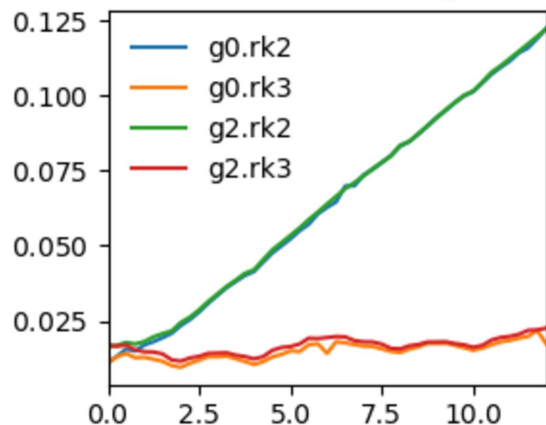
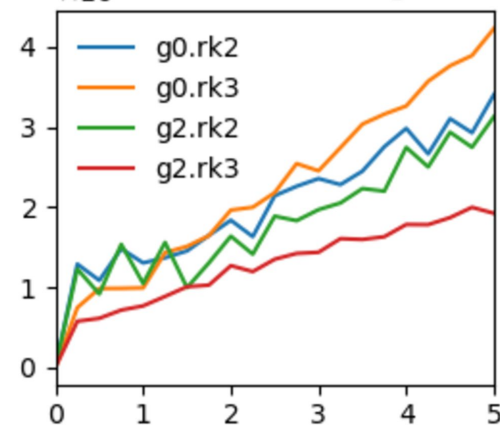
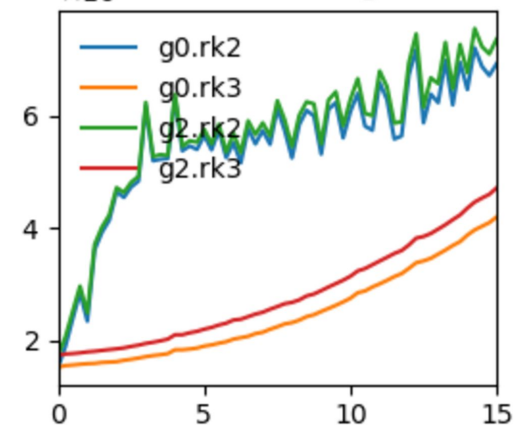
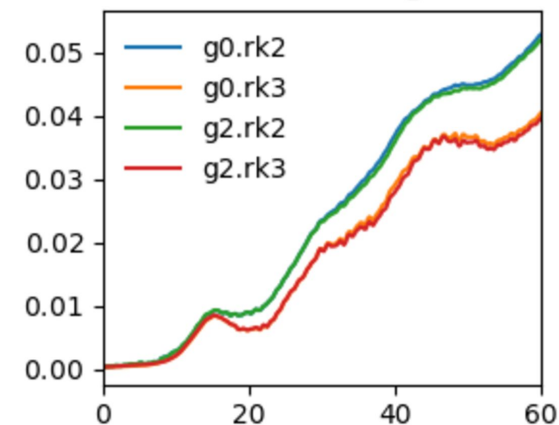
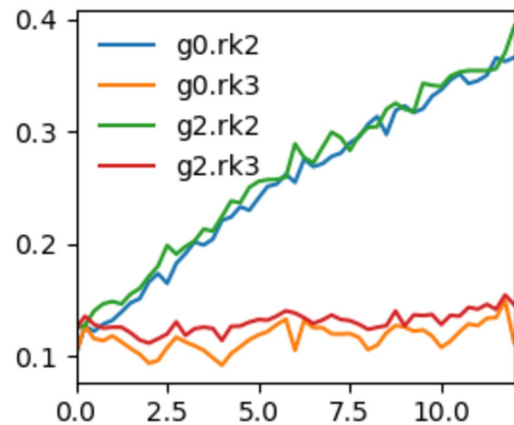
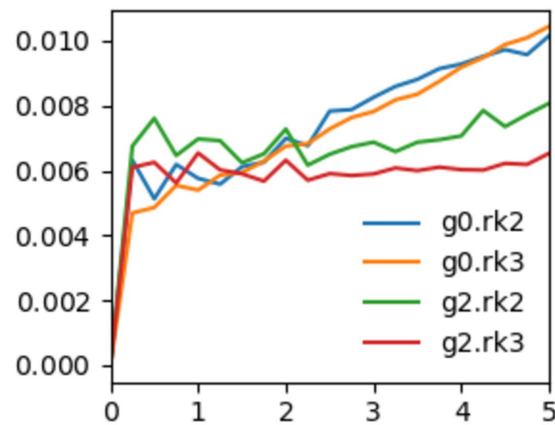
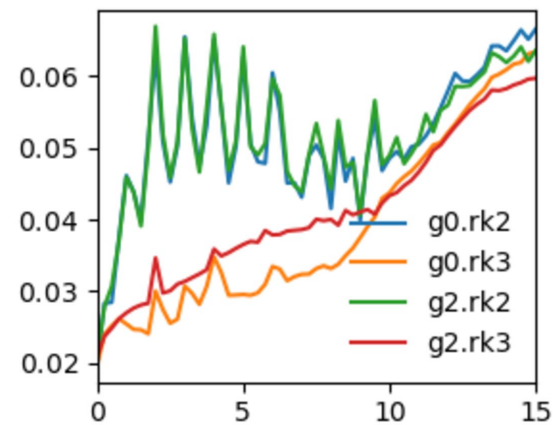
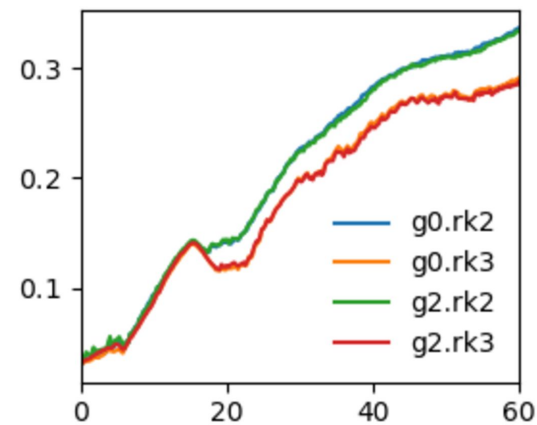


c) even tile neighbor rotation





- eq-dist ref
- eq-angular ref
- eq-edge ref
- tile-corner ref
- gnomonic projection

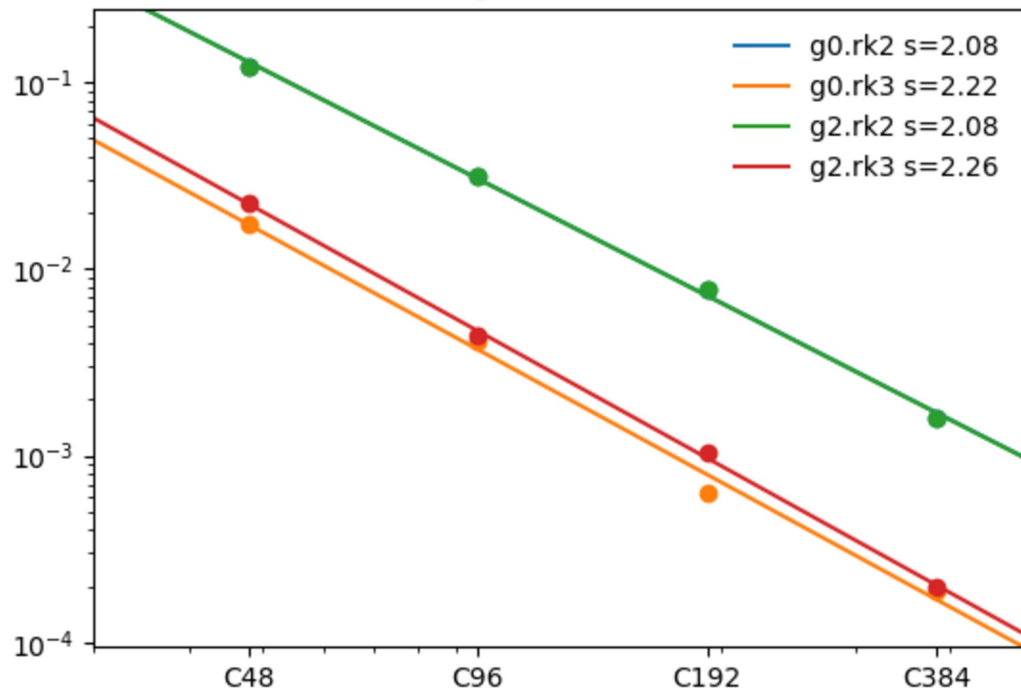
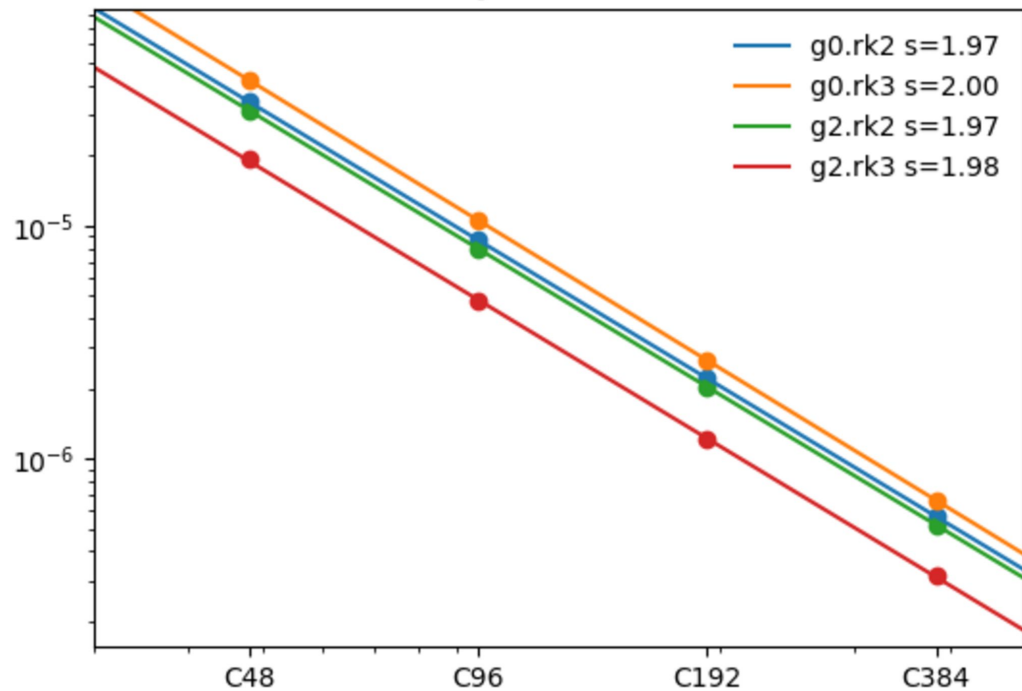
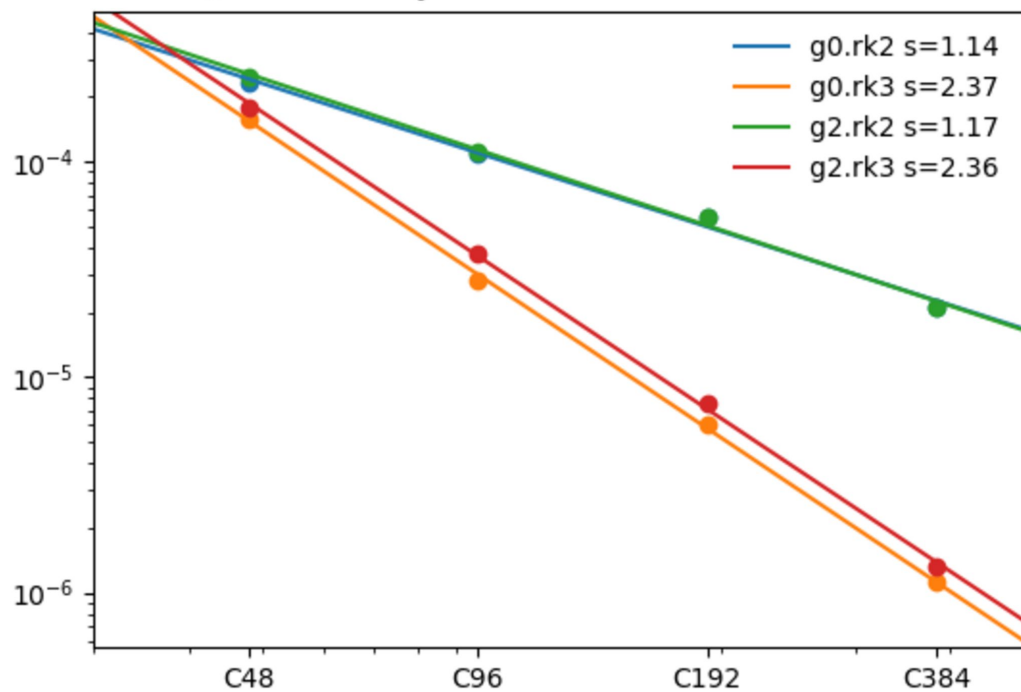
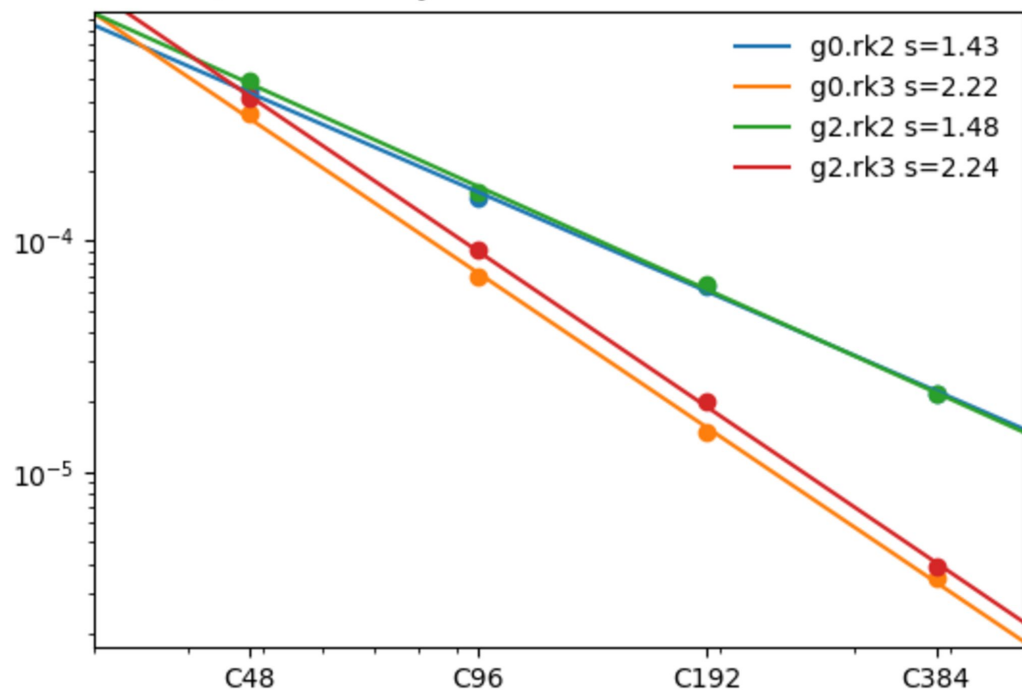
C48.case1a45 l_1  $\times 10^{-5}$ C48.case2a45 l_1  $\times 10^{-4}$ C48.case5 l_1 C48.case6 l_1 C48.case1a45 l_2  $\times 10^{-5}$ C48.case2a45 l_2  $\times 10^{-4}$ C48.case5 l_2 C48.case6 l_2 C48.case1a45 l_∞ C48.case2a45 l_∞ C48.case5 l_∞ C48.case6 l_∞ 

Simulation Days

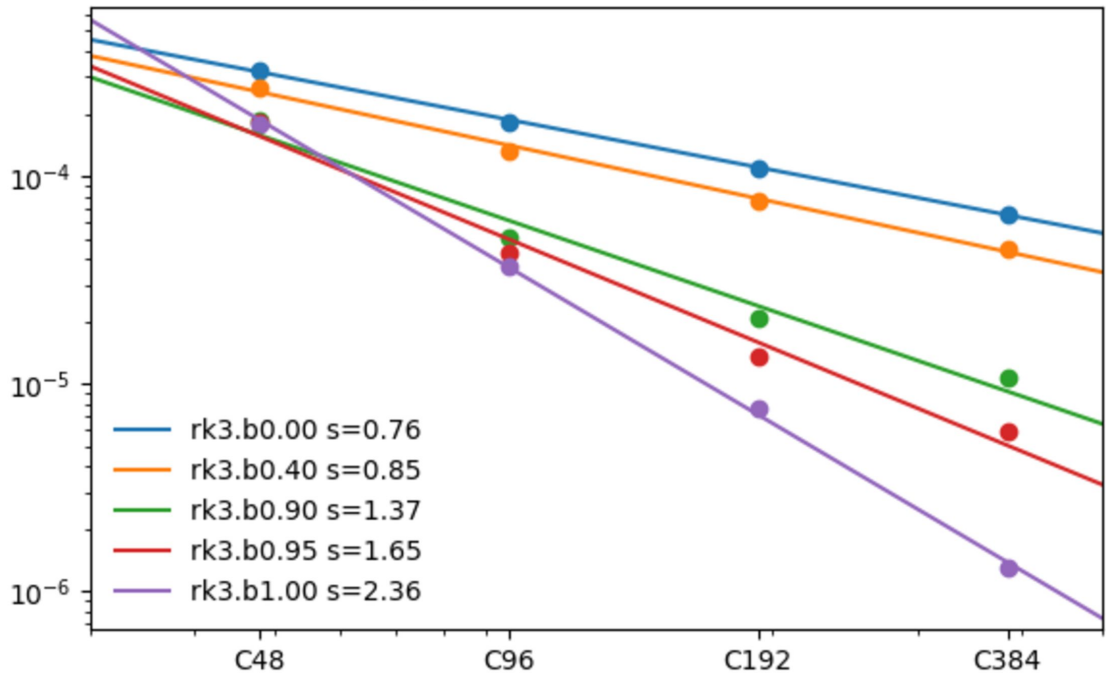
Simulation Days

Simulation Days

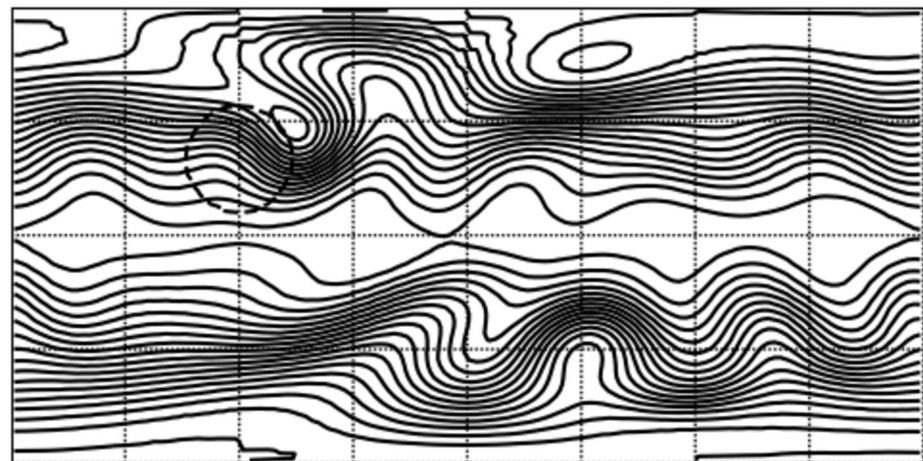
Simulation Days

case1a45 l_2 error on Day 12case2a45 l_2 error on Day 5case5 l_2 error on Day 1case6 l_2 error on Day 1

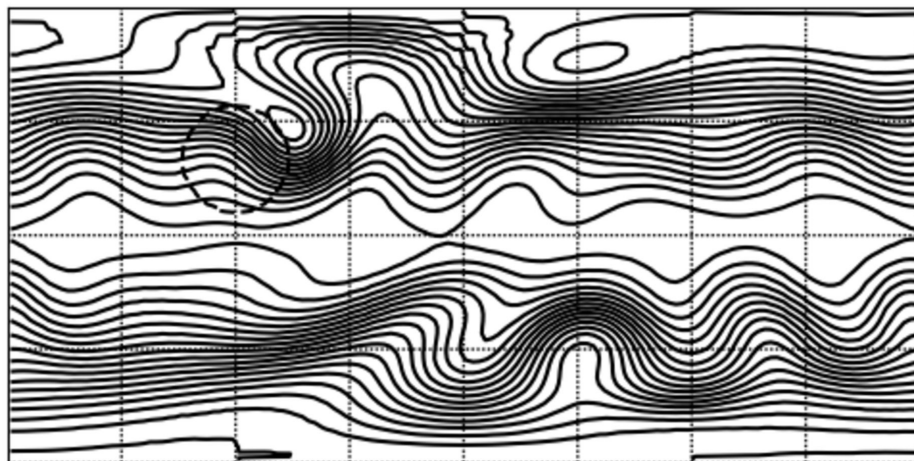
case5 l_2 error on Day 1



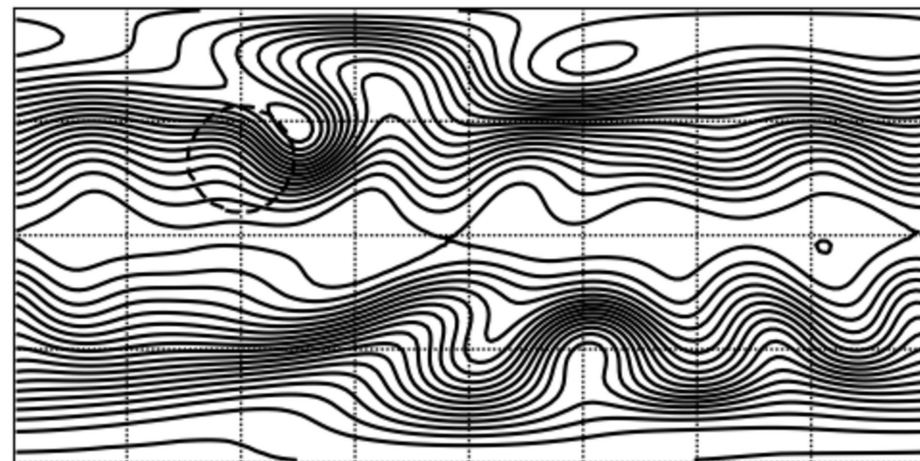
C48.rk2.b0.00



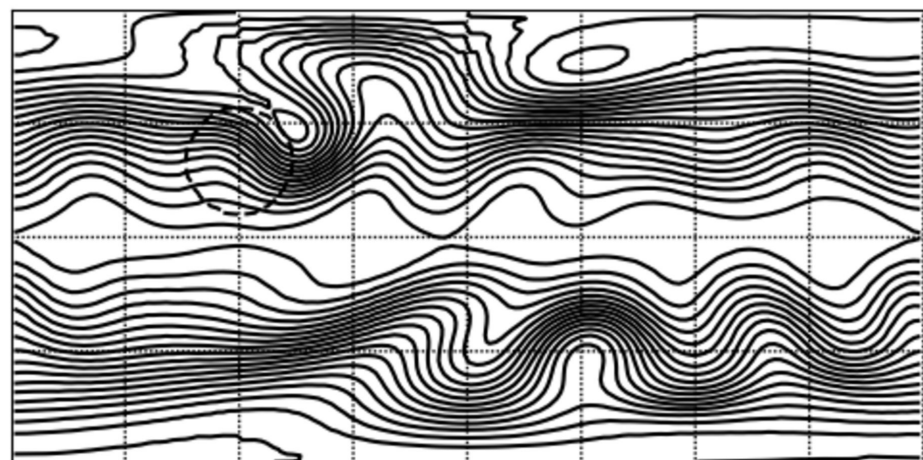
C48.rk3.b0.00



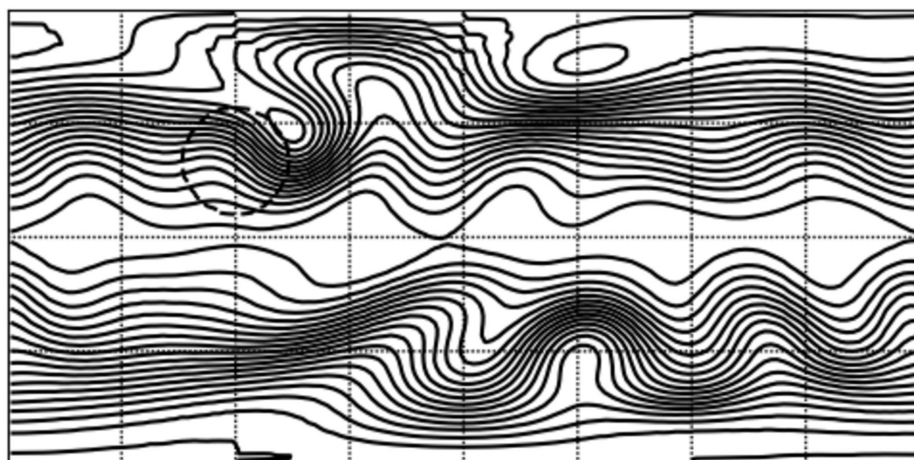
C768.rk3.b0.00



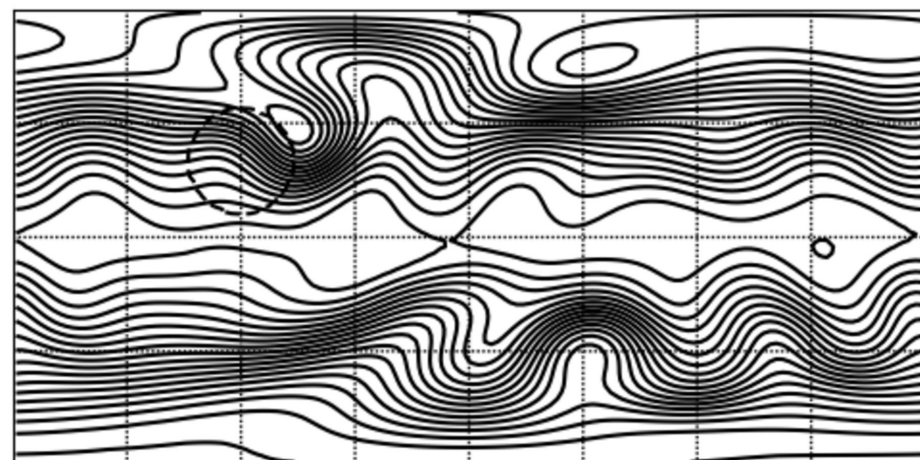
C48.rk2.b0.40



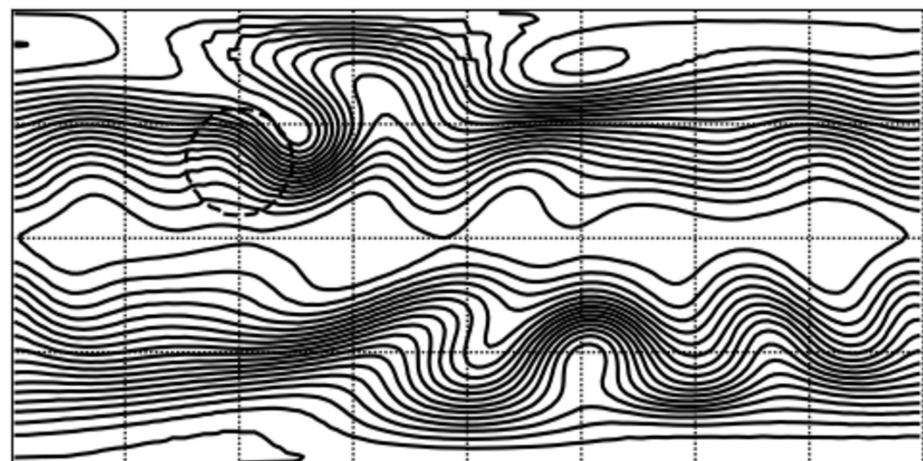
C48.rk3.b0.40



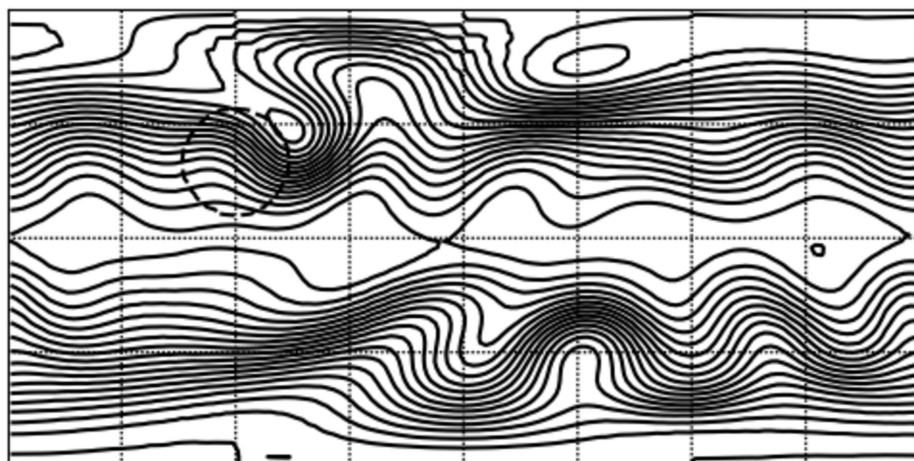
C768.rk3.b0.40



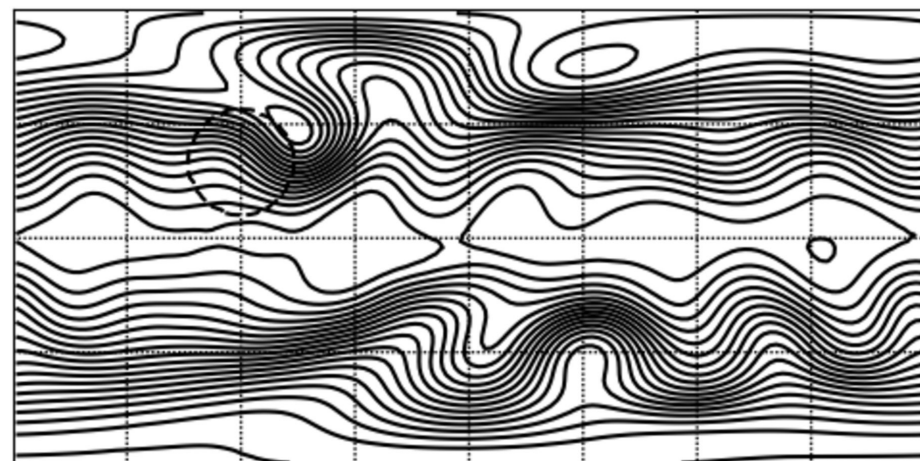
C48.rk2.b0.95



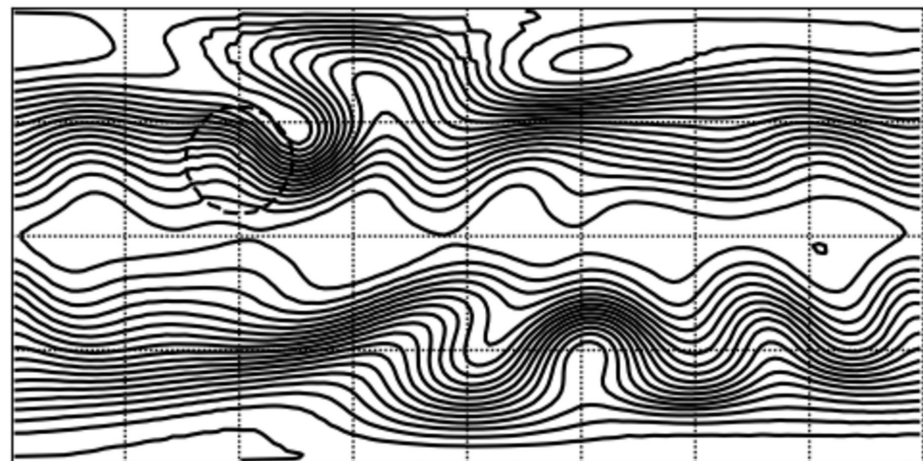
C48.rk3.b0.95



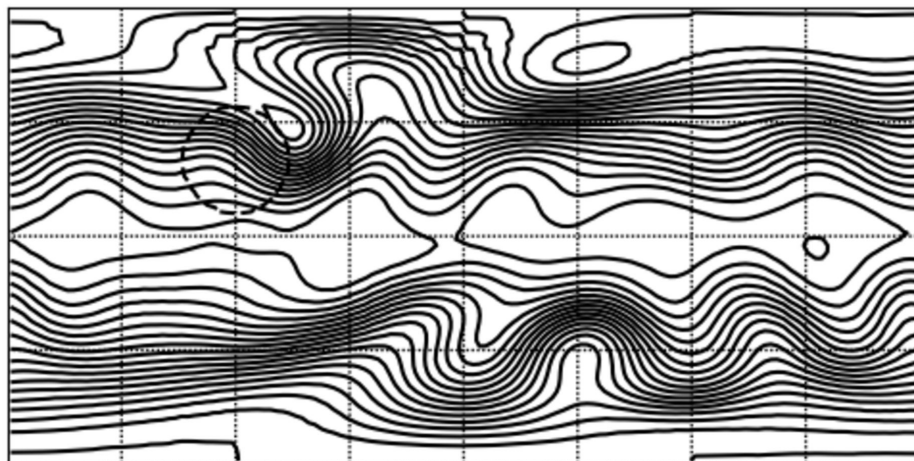
C768.rk3.b0.95



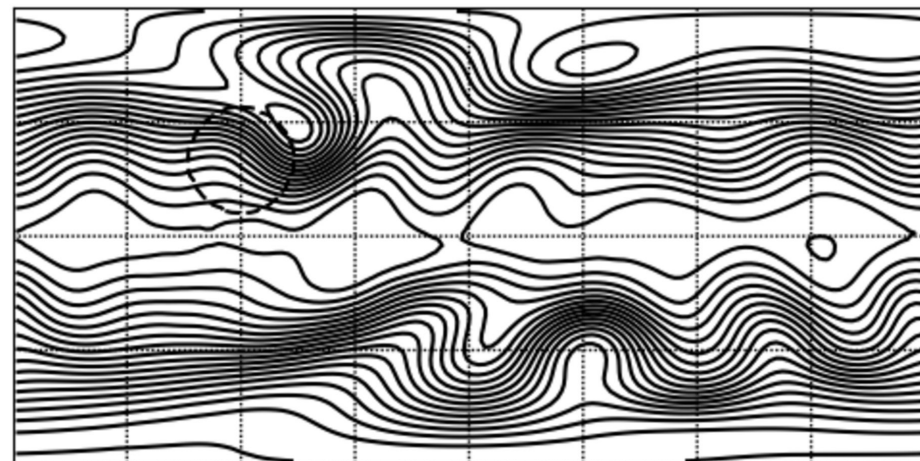
C48.rk2.b1.00



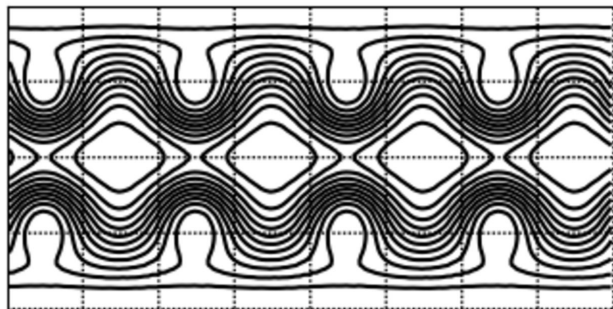
C48.rk3.b1.00



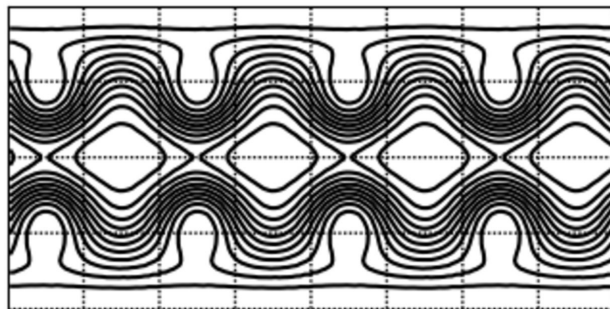
C768.rk3.b1.00



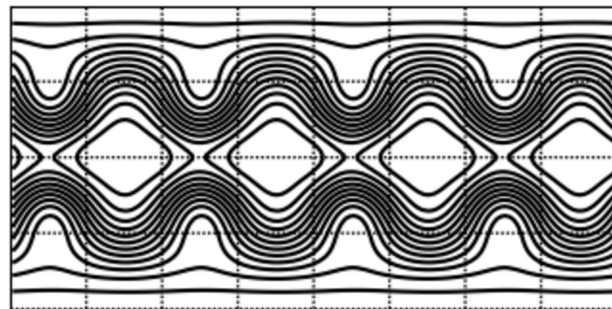
C48.g2.rk2 Height Field - Day 14



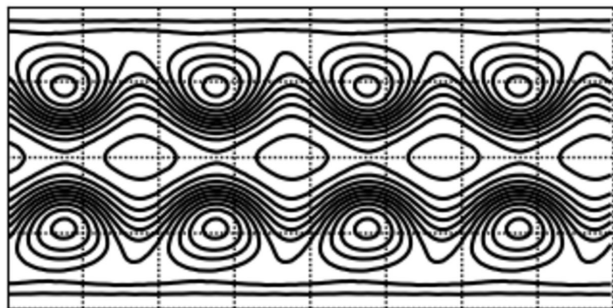
C48.g2.rk3 Height Field - Day 14



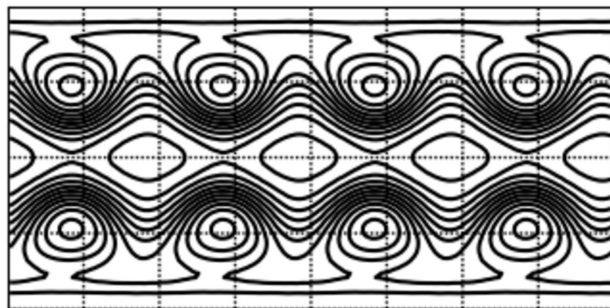
C768.g2.rk3 Height Field - Day 14



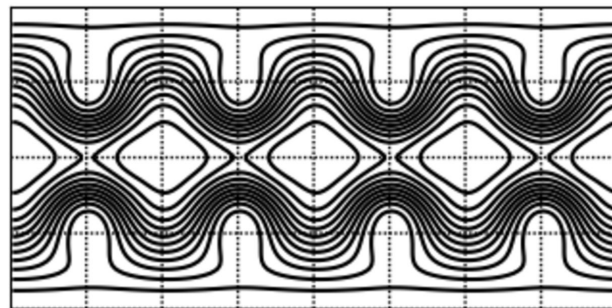
C48.g2.rk2 Height Field - Day 40



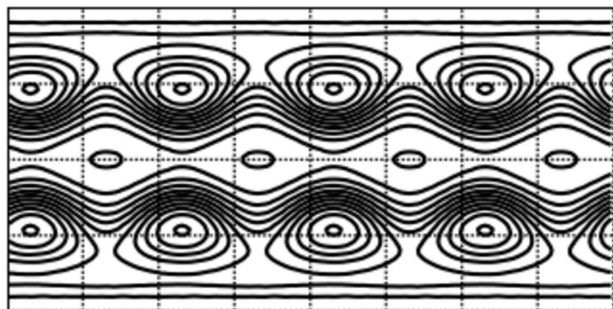
C48.g2.rk3 Height Field - Day 40



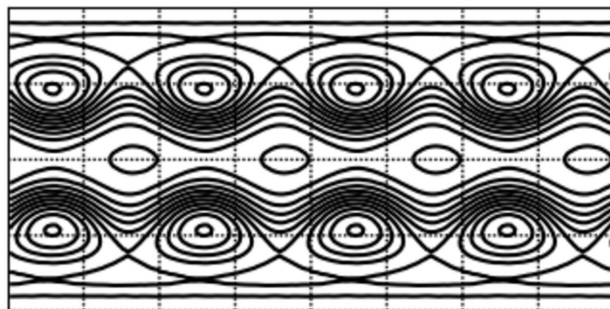
C768.g2.rk3 Height Field - Day 40



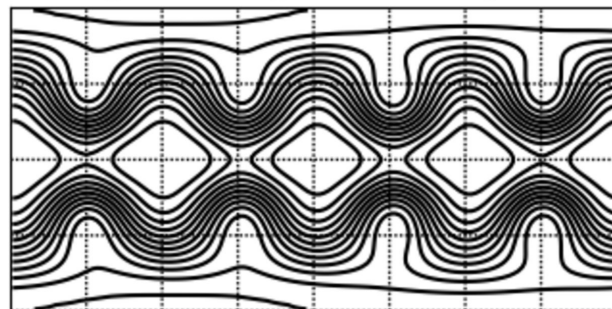
C48.g2.rk2 Height Field - Day 80



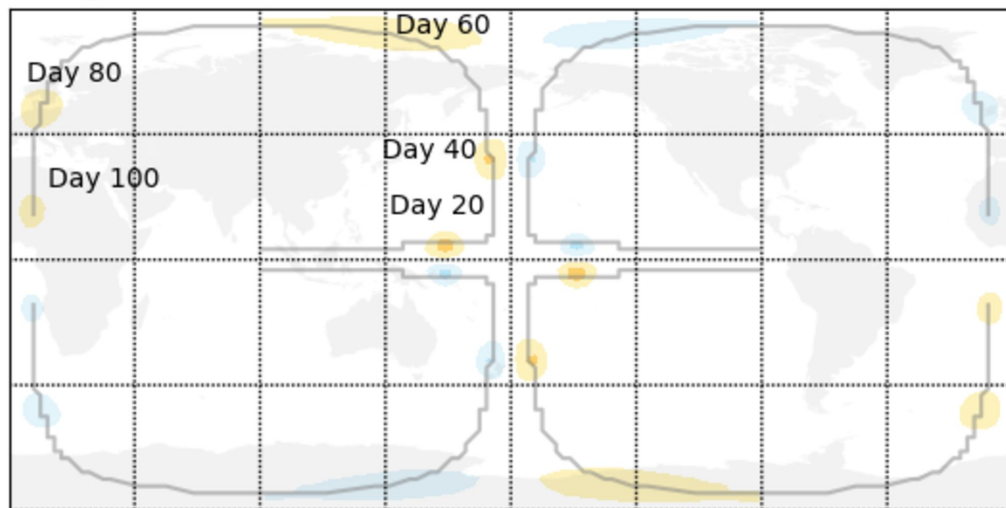
C48.g2.rk3 Height Field - Day 80



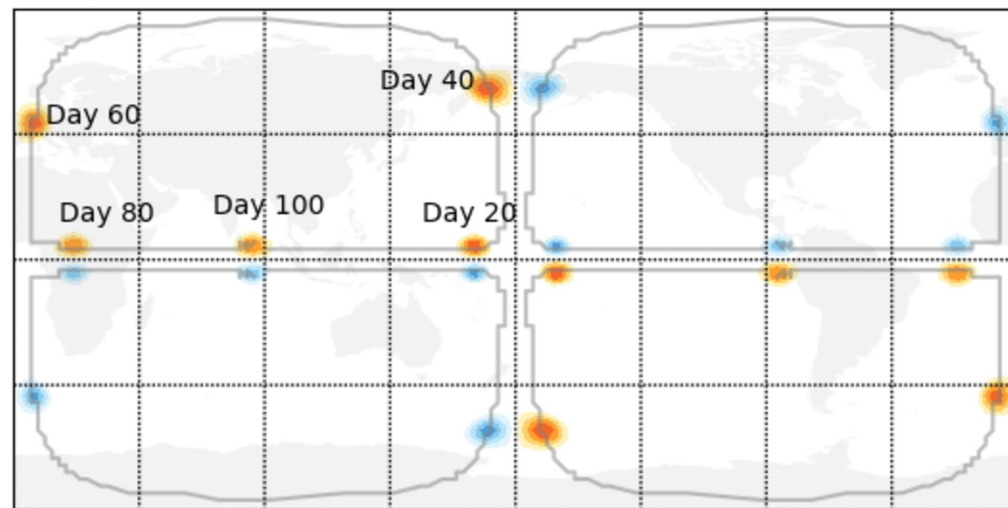
C768.g2.rk3 Height Field - Day 80



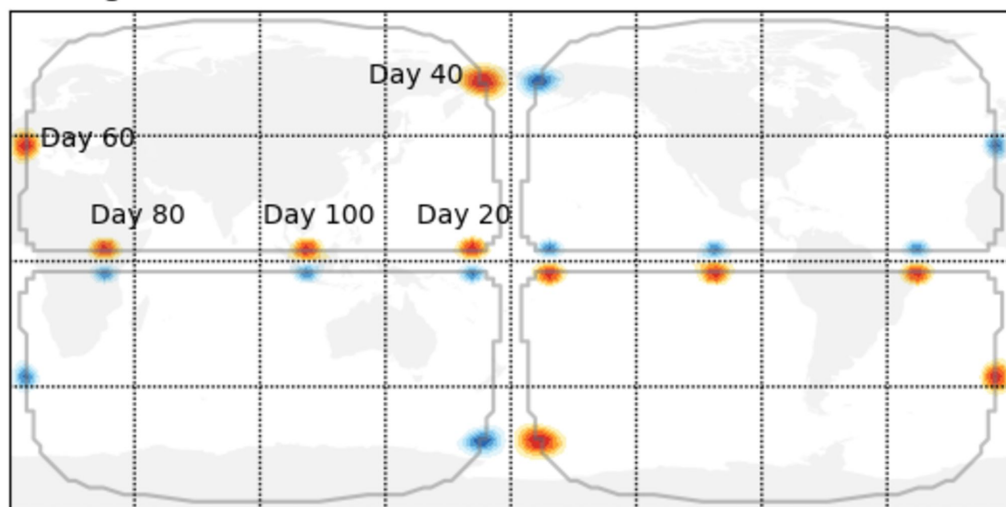
C48.g2.rk3



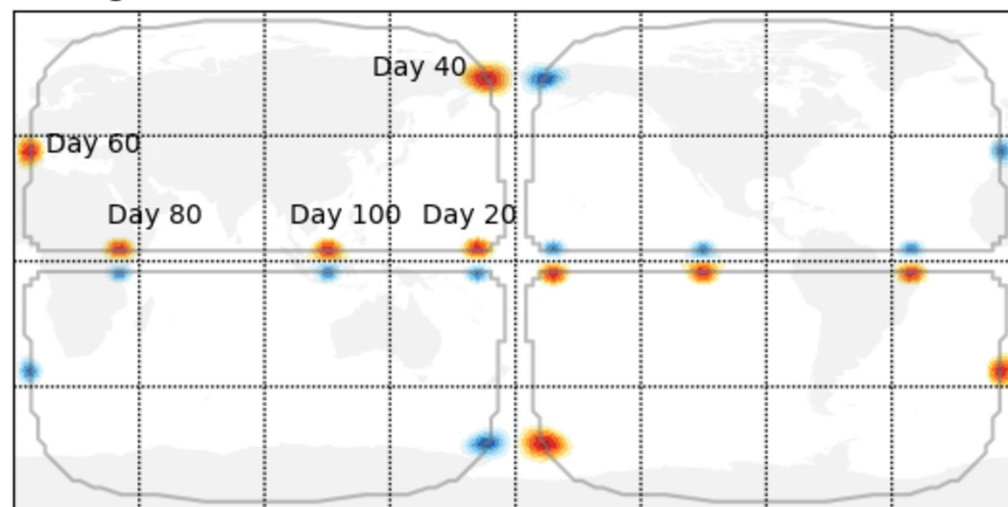
C96.g2.rk3



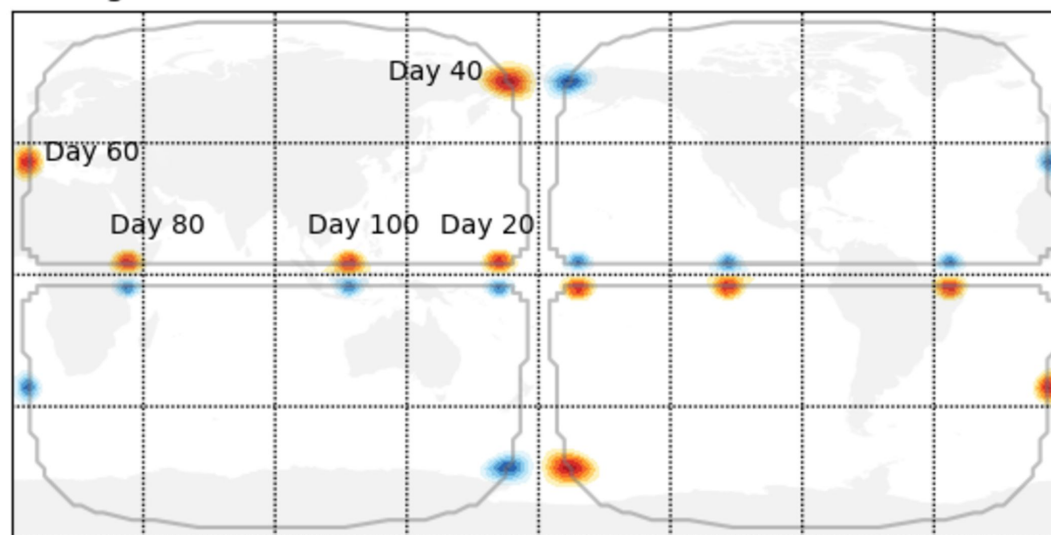
C192.g2.rk3



C384.g2.rk3



C768.g2.rk3



-6.0e-05

-4.0e-05

-2.0e-05

0.0e+00

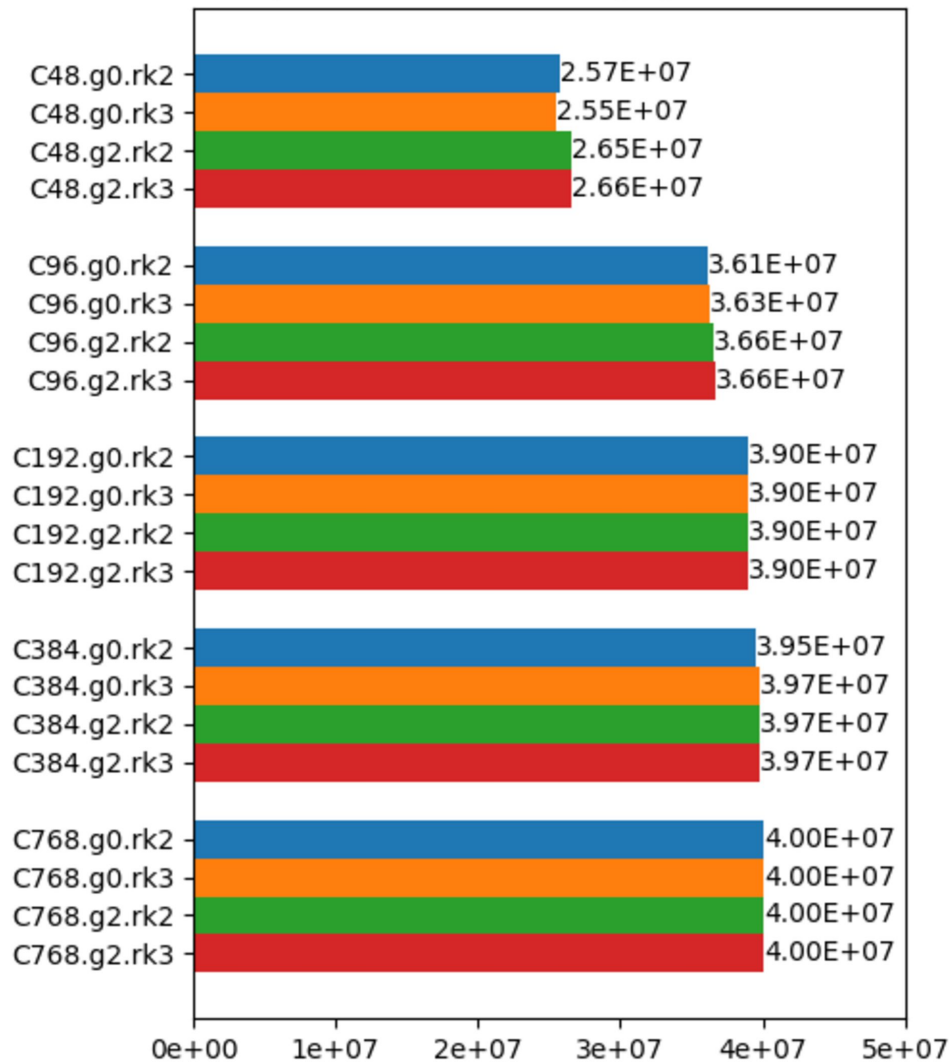
2.0e-05

4.0e-05

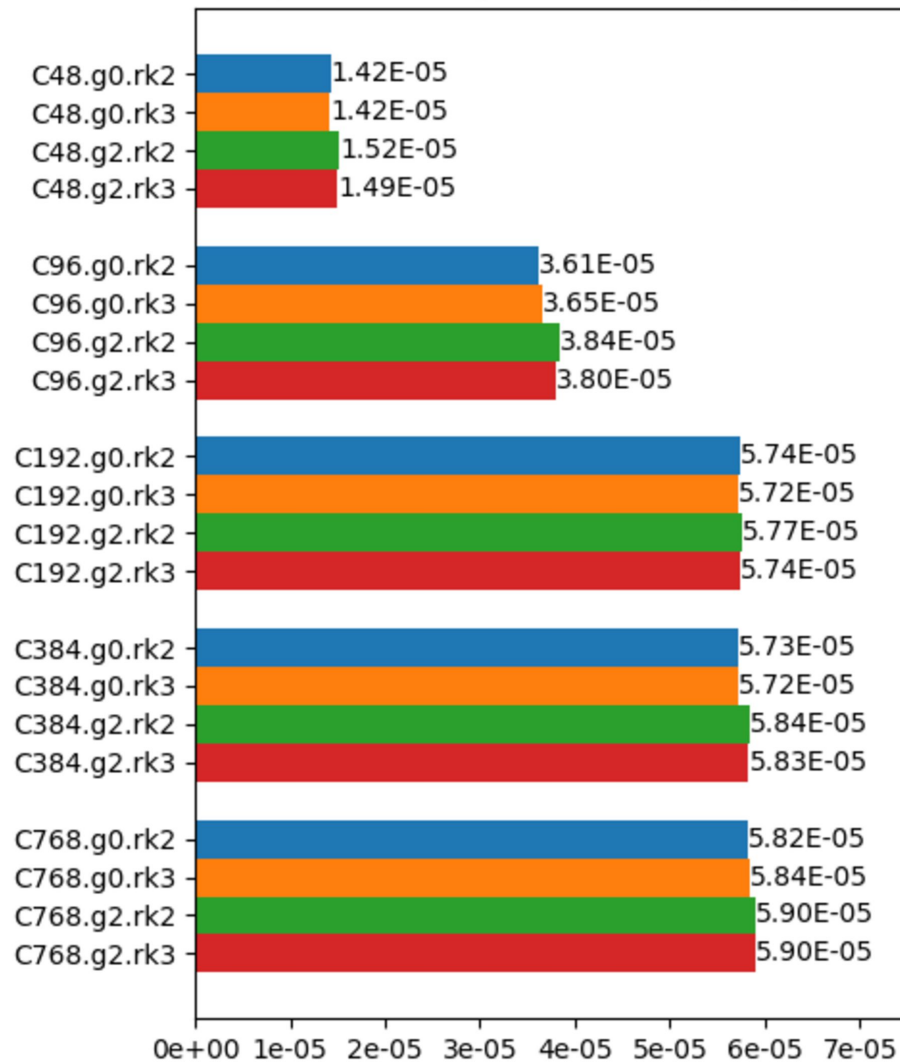
6.0e-05

vort [1/s]

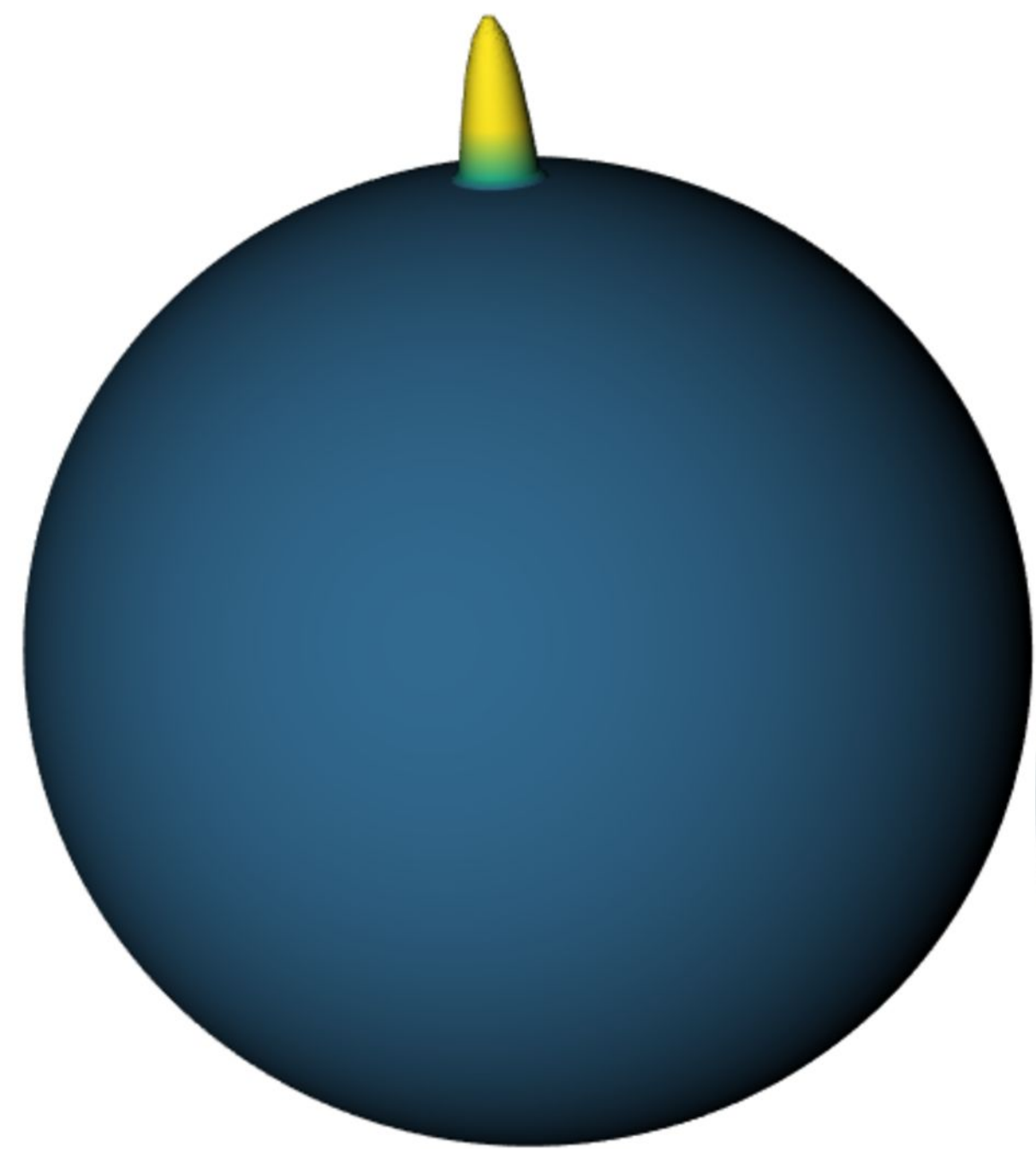
NW Quad Vort Travel Dist [m]



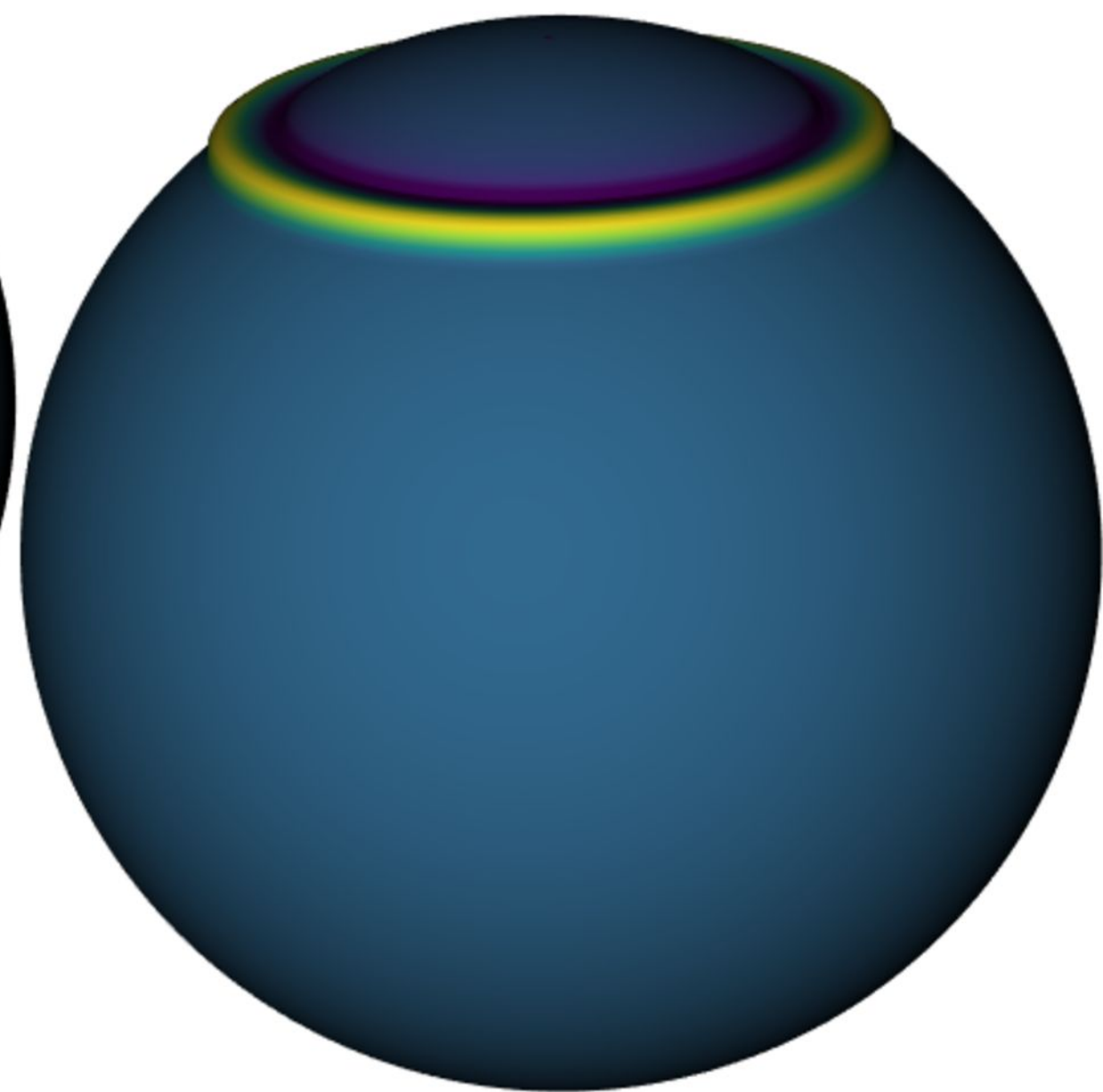
NW Quad Vort Day 100 intensity [1/s]



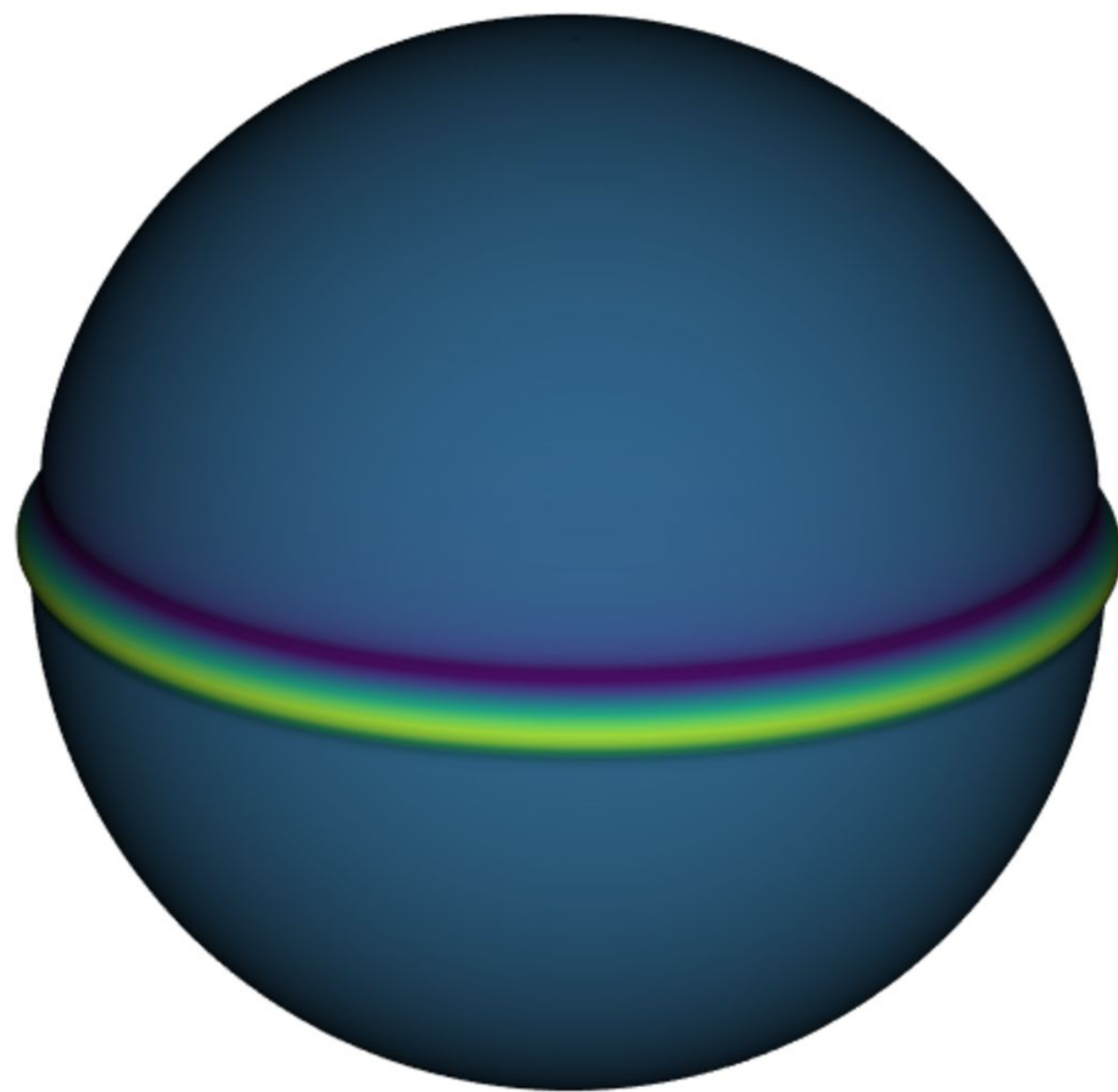
Day 0



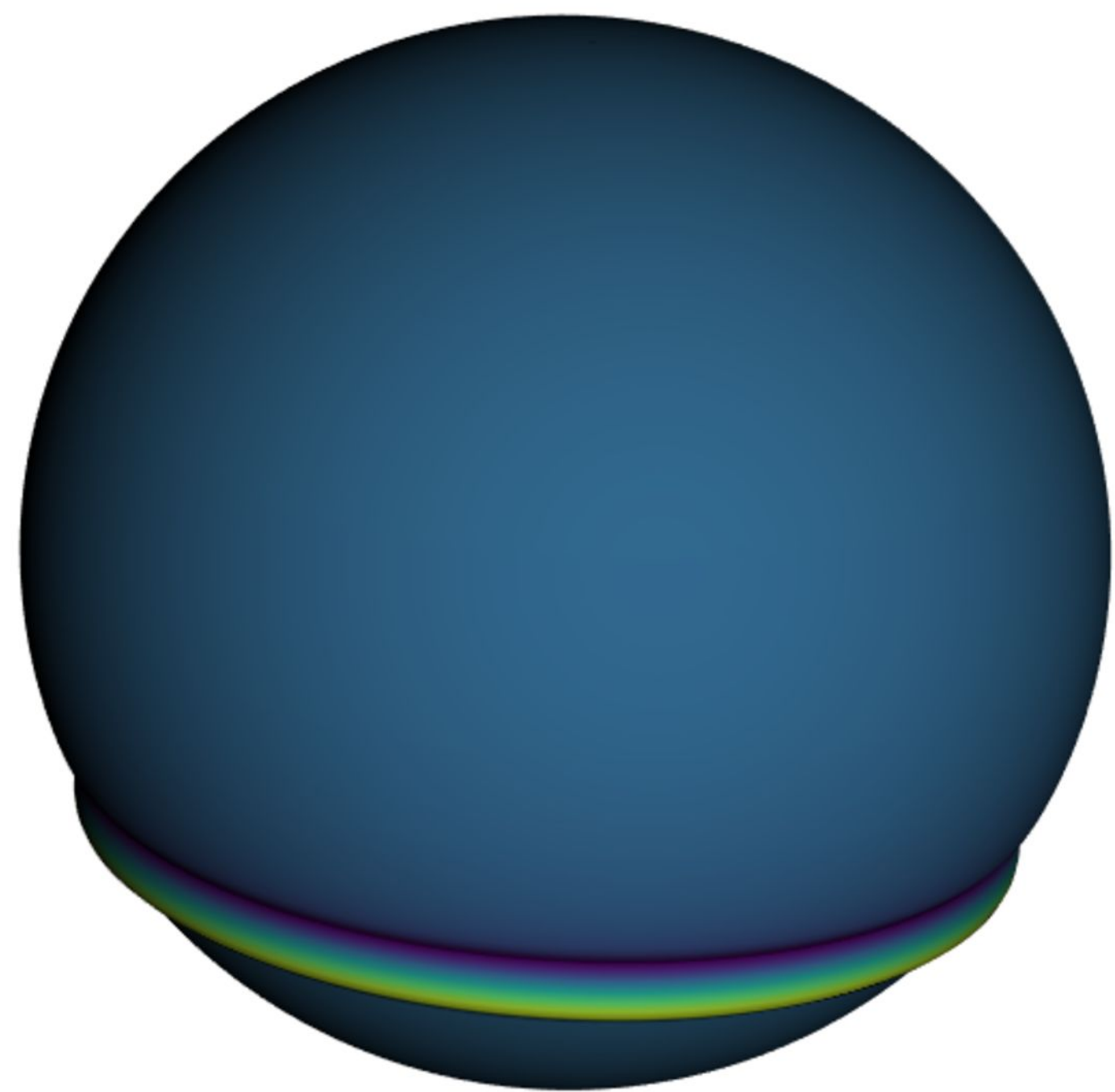
Day 2



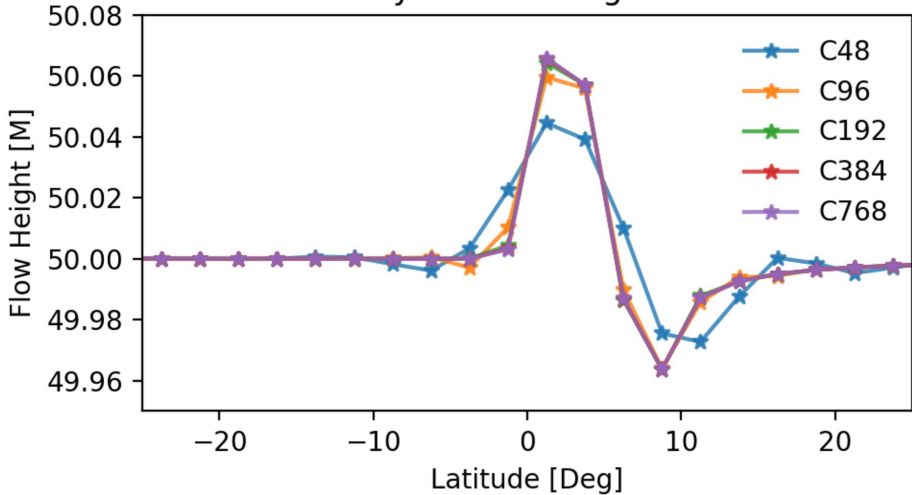
Day 5



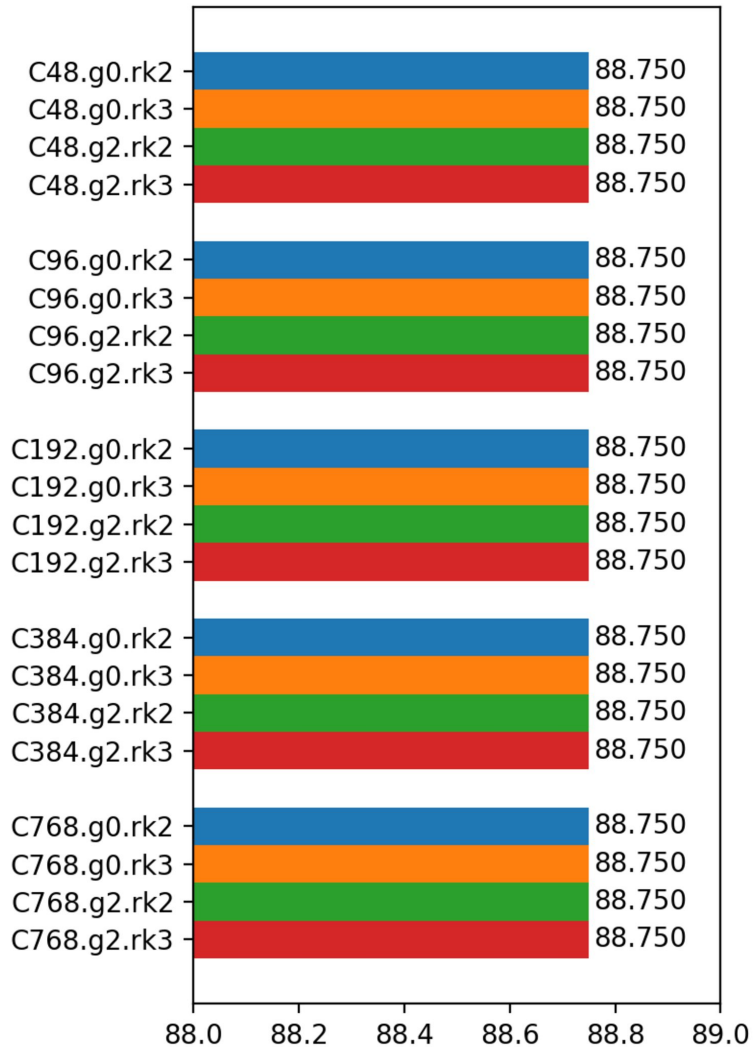
Day 7



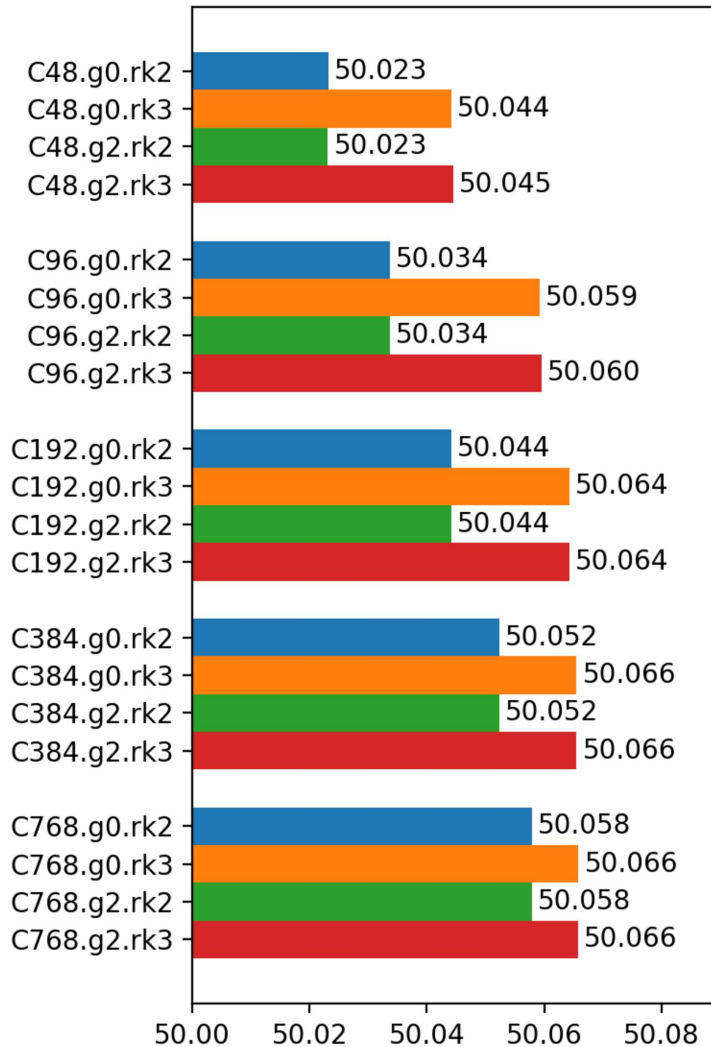
Day 5 of h with g2.rk3



Distance to NP at Day5 [Deg]



Peak flow height at Day 5 [M]

Max value of $|u|$ at Day5 [M/s]